2005

Cementitious Permeable Pavement as a Passive Unit Operation and Process for Stormwater Quality and Quantity Control

Xuheng Kuang
Louisiana State University and Agricultural and Mechanical College, xkuang1@lsu.edu

CEMENTITIOUS PERMEABLE PAVEMENT AS A PASSIVE UNIT OPERATION AND PROCESS FOR STORMWATER QUALITY AND QUANTITIY CONTROL

A Dissertation
Submitted to the Graduate Faculty of the
Louisiana State University and
Agriculture and Mechanical College
in partial fulfillment of the
requirements for the degree of
Doctor of Philosophy

in

The Department of Civil and Environmental Engineering

by
Xuheng Kuang
B.S., Wuhan University of Hydraulic and Electrical Engineering, Wuhan, China, 1994
M.S., Wuhan University of Hydraulic and Electrical Engineering, Wuhan, China, 1997
December 2005

ACKNOWLEDGEMENTS

I would like to extend my sincere appreciation to all those who made this research possible. First and foremost, I would like to thank Dr. John Sansalone who has consistently gone above and beyond the call of duty in helping me attain my goals. He has been both a friend and mentor in this great learning experience.

I appreciate the enthusiastic encouragement, patient guidance and creative advice of my committee members, Dr. Linbing Wang, Dr. Louay Mohammad, Dr. John Metcalf, Dr. Donald Adrian, Dr. Radhey Sharma, and Dr. Walter Keithly, who have taught me what it means to be a distinguished professional.

I would like to thank all my colleagues, Bo Liu, Cristian I Druta, Gaoxiang Ying, Jia Ma, Jong-yep Kim, Matt McGaugh, Natalie Magill, Sreemoyee Ganguly, Srikanth Pathapati, Tianpeng Guo, Vi Ngugen, Will Bartlett, Yongping Wang, Yuhong Sheng and Zheng Teng. Without their help, this work would not be possible.

I would like to express special thanks to all those who work in the Concrete Lab of Louisiana Transportation Research Center, Mr. Randy Young, Mr. Sadi Torres, Mr. Alvin Mix, Mr. John Eggers, Mr. Matt Tircuit, and the student worker, Mr. Christopher Duet and Ryan Estess. Thanks for their help in mix design, specimens fabrication and tests.

I would also like to thank all faculties and staffs in the Department of Civil and Environmental Engineering and the Mechanical Workshop who taught me courses or gave me help in my PhD career. Without their help, this work would not be possible either.

A special thank is due to my wife, Yanrong, my little girl, Vivian, and my family. Their love, support, encouragement and understanding have driven me throughout this long journey and experience. I cherish and enjoy the life with them together.

TABLE OF CONTENTS

LIST OF TABLES

LIST OF FIGURES

ABSTRACT

With respect to the problems caused by impervious pavements, cementitous permeable pavement (CPP) functions as a passive unit operation and process for stormwater quality and quantity control through infiltration, evaporation, filtration, absorption and reaction mechanisms.

CPP pore characteristics were examined through pore connectivity analysis using X-Ray Tomography (XRT). Image resolution influence on image analysis results was evaluated. Relationships between parameters of pore characteristics were evaluated.

Factors that significantly influence fluid flow in CPP media include effective porosity, pore connectivity and pore size distribution. A modified Kozeny-Carman model in which effective porosity ϕ_e, specific surface area based on effective pores $(SSA)_{pe}$, and weighted tortuosity $(L_e/L)_w$ were employed was developed and demonstrated applicable for CPP hydraulic conductivity estimation. Both the k- ϕ_t relationship and k- ϕ_e relationship were developed with a power law model.

Filtration of CPP subject to different particle loadings for a constant particle size gradation was investigated experimentally. Removal efficiencies for both total particles and for each size fraction were examined. A power law model was developed for the relationship between suspended solid concentration (SSC) and turbidity.

CPP clogging potential was evaluated by measuring the temporal hydraulic conductivity, k(t) as well as the particles strained on CPP surface. Two CPP cleaning methods, vacuuming and sonicating followed by backwashing, were evaluated and found capable of recovering k_0 up to 96%. A method for scheduling of CPP maintainance was presented.

3 groups of CPP specimens were sued to evaluate the capability of pH and alkalinity elevation and phosphorus removal functions of CPP. The removal efficiencies of total phosphorus

(TP), total dissolved phosphorus (TDP) and total particulate phosphorus (TPP) were evaluated through experimental measurements.

Factors that influence CPP strength and porosity, including water to cement ratio (w/c), aggregate to cement ratio (a/c), aggregate gradation and the degree of compaction, were evaluated through 6 mix designs with different design parameters. Based on test results, an optimized mix design was recommended, and a CPP structural with $f_c' > 25$ MPa (3500 psi), $f_s > 2.76$ MPa (400 psi), $\phi_t > 20\%$, and permeability $k > 0.3$ cm/s is desirable.

CHAPTER 1 INTRODUCTION

1.1 PROBLEMS AND IMPACTS CAUSED BY IMPERVIOUS PAVEMENTS

With the significant urban growth of the 20th and 21st century combined with the widespread introduction of impervious pavement around 1900, deleterious hydrologic, climate and environmental problems associated with urban land development have grown increasingly serious due to the increased peak flow, volume and lag time of runoff, reduced underground water recharge, and degraded water quality (Bäckström 2000; Field et al. 1982; Jackson et al. 1974; Kuennen 2003; Teng and Sansalone 2004). With urban growth, forests, farms, meadows and pervious soils are being transformed into compacted soils, houses, shopping centers, roadways and parking lots, resulting in a much higher degree of imperviousness. Compared to soils covered by vegetation, the highly impervious nature of disturbed soils and impervious pavement greatly reduces the infiltration capacity and the capability to recharge aquifers and maintain stream base flow and waterway health (Malcom 1989, Field et al. 1982). As a result, this rainfall-runoff is lost as a resource for the long-term health of natural waters (Teng and Sansalone 2004). Control of rainfall-runoff has been increasingly challenging with the growth of urbanization and urban population of the world. Data from 47 small urban watersheds across the USA indicate that an approximately linear relationship exists when the volume-based runoff coefficient ("C") is regressed against watershed imperviousness (Schueler 1987).

Further research has shown that the degree of imperviousness in the built environment is significantly correlated to hydrologic, climate and environmental problems (Bäckström 2000; Balades et al. 1995; Field et al. 1982; Jackson et al. 1974; Kuennen 2003). The most obvious impact of impervious pavement on hydrology is the alteration of the rainfall-runoff relationship. As water is conveyed downstream, along with soil, fertilizer, and other constituents, the runoff

causes flooding and increased transport of particulate and dissolved pollutants and debris. Large quantities of runoff cause significant problems in the environment. In many cities the unintentional combination of storm and sanitary sewers are common, and the combined runoff and sewage have to overflow through bypass due to the limited treatment capacity. This contaminant- and nutrient-loaded water impairs our surface waters and accelerates eutrophication (Miller 1989). Hydrologic impacts also include channel incision, bank erosion, and increased sediment transport (Andersen et al. 1999; Bäckström and Bergström 2000; Brattebo and Booth 2003; Watanabe 1995). Examples of local climate impacts include generation of higher temperature in urban areas as compared to surrounding rural areas resulting in urban heat islands (Kobayashi et al. 2002; Oke 1982). Examples of environmental impacts include significantly increased loading and delivery of anthropogenic constituents such as metal elements, nutrients, organics, and particulate matter discharged to the environment (Bäckström and Bergström 2000; Ghafoori and Dutta 1995; Sansalone 1999; Sansalone and Teng 2004).

Recognizing the effects of urbanization on the hydrological environment, many communities have passed laws encouraging municipalities and developers to practice sound stormwater management on their properties (Field et al. 1982; Diniz 1980). However, traditional stormwater management systems that collect, transport and dispose of stormwater are not able to meet the requirement of the rapid land development and the continuously increasing degree of imperviousness due to the installation of streets, parking lots and rooftops (Andersen et al. 1999; Bäckström and Bergström 2000; Brattebo and Booth 2003; Watanabe 1995; Field et al. 1982). An available and effective approach to mitigate these problems is to reduce the impervious surface in urban areas, which suggests the utilization of permeable pavement.

1.2 PERMEABLE PAVEMENT

Permeable pavement, also called pervious pavement, or porous pavement, is a structural low impact development (LID) material for rainfall-runoff control, in which cemented aggregate can produce hydraulically-conductive pore characteristics throughout the pavement structure (Berengier et al. 1997). Such pore characteristics permit gravitational drainage, capillary movement, evaporation, gaseous transport, precipitation and dissolution reactions, and filtration mechanisms.

Permeable pavement has generated increasing interest of a wide range of stakeholders over the last several decades (HMAT 2003). With respect to the problems caused by impervious pavements, permeable pavement reduces rainfall-runoff peak, volume (Bäckström and Bergström 2000; Ghafoori and Dutta 1995; Legret and Colandini 1999; Pagotto et al. 2000), improves water quality through physical and chemical mechanisms (Legret and Colandini 1999; Pagotto et al. 2000, Sansalone and Teng 2004), facilitates groundwater and interflow recharge (HAMT 2003; Ranieri 2002), and mitigates temperature increases (Kobayashi et al. 2002; Oke 1982; Asaeda and Ca 2000).

Permeable pavements have been more and more widely applied in the USA, Europe, Australia and Japan in the last two decades. In the United States, interest is once again growing in open-graded friction courses (OGFC), and more and more states are taking interest in OGFCs. Georgia, Florida and Alabama require open graded friction courses to be used on all interstate projects (Kuennen, 2003). Georgia, Florida, South Carolina, Texas, Arizona, Colorado, Utah, Michigan, New Jersey, Rhode Island, and Vermont are among those joining lead state Alabama in the study of OGFCs (Kuennen 2003).

Permeable pavements have been widely used in Europe since 1970s for stormwater

management. In Germany, for example, the use of permeable pavements has become widespread for a sustainable urban water management, because it is a highly suitable method to reduce surface runoff, and in some newly developed areas, legal regulations require the infiltration of rainwater into the groundwater or to discharge runoff into a receiving water (Fach et al. 2002). In Spain, experimentation with porous mixes started in 1980 when the Ministry's Road Department built four test sections in Cantabria, and the good behavior of these sections and the advantages offered by these mixes for the safety and comfort of driving has led to wide and frequent application of permeable pavements in Spain (Jiménez and Pérez 1990). In Switzerland, the first permeable pavement was placed on an airport runway in 1972, and permeable pavements have been used since the later 1970s and the early 1980s (Isenring et al. 1990). In the UK, permeable highway pavements were put in place in the middle of 1980s (Pratt et al. 1995). In France, the use of porous pavements as a road surfacing materials has grown considerably since 1985 (Pagotto et al. 2000). Swedish researchers found that porous pavement removed constituents effectively in highway runoff as a type of infiltration BMP. A Swedish porous pavement system, known as the Swedish Unit Superstructure, was developed as both a water quantity and quality control BMP (Niemczynowicz 1989). Most permeable pavements constructed more than 20 years ago in Europe still function well.

In Japan, infiltration facilities including permeable pavements were introduced to Japan in the early 1970s and progressively implemented during the 1980s. When rainfall infiltration was first implemented, its primary objective was to reduce runoff volume. With the enhanced recognition of water quality benefits, as well as the Japanese desire to maintain closeness with nature in an urban setting, however, permeable pavement philosophy has shifted more towards groundwater cultivation than runoff reduction since the 1990s.

1.3 CEMENTITIOUS PERMEABLE PAVEMENT (CPP)

One common form for permeable pavement, cementitious permeable pavement (CPP) consists of Portland cement, open-graded aggregate and water (Li et al. 1999). CPP has generated increasing interest of a wide range of stakeholders over the last several decades (HMAT 2003). Compared to asphalt porous pavement, CPP has its outstanding advantages in both transportation and environment aspects. It provides a relatively rougher surface for traffic, which makes our car-moving safer under inclement weather conditions (Ghafoori and Dutta, 1995 (a), 1995(b)). From an environmental viewpoint, CPP can not only control the quantity of runoff as asphalt porous pavement does by reducing the peak flow rate and volume of runoff, it also has the capability to control the quality of runoff by removing particulate matters, metals, and anthropogenic pollutants from runoff (Teng, 2004; Stotz and Kruth 1994), and elevate alkalinity and pH values in runoff (Li et al. 1999; Park and Tia 2004; Pratt 1999). Combined with engineered adsorptive-filter media, cementitious porous pavement (CPP) functions as a primary unit operation/process and a capable infiltration-exfiltration best management practice (BMP) in removing both soluble and particulate pollutant from stormwater (Fujita 1993; Jahangir-Issa 1998; Legret et al. 1999; Pratt et al. 1989; Sansalone 1999; Teng and Sansalone 2004; Yu 1993). CPP structures are able to significantly reduce the impact of any real or perceived first flush effect commonly associated with urban runoff (Anderson et al. 1999; Aulenbach and Chan 1998; Rajapakse and Ives 1990). For example, the permeable pavement systems promote infiltration using porous pavement and granular subgrades systems for quantity storage, ground water recharge and quality control in all those countries, such as in US (Brattebo and Booth 2003; Field 1982; Jackson and Ragan 1974, Sansalone 1999; Teng and Sansalone 2004), UK (Anderson et al. 1999; Schluter and Jefferies 2002), Switzerland (Isenring et al. 1999;

Xu and Mermoud 2003), Sweden (Backstrom and Bergstrom 2000; Niemczynowicz and Hogland 1987; Teng and Sansalone 2004), German (Fach et al. 2002; Stotz and Krauth 1994), and Spain (Jimenez and perez 1990), Singapore (FWA et al. 1999; Tan et al. 2003) and France (Balades et al. 1995; Legret and Colandini 1999; Pagotto et al. 2000). The infiltration-exfiltration BMPs exhibited a high pollutant removal capability with total solids suspension (TSS) mass removal up to 90%, total phosphorus (TP) removal up to 65% and total nitrogen (TN) up to 80% (Park and Tia 2004; Sansalone 1999; Teng and Sansalone, 2004). In-situ partial exfiltration reactor (PER) has been developed combining the advantage of CPP, infiltration trenches and engineered filtration. In such a combined unit operation and process, CPP functions as initial control preventing solids from entering the PER (Teng and Sansalone, 2004).

1.4 MECHANISTIC EVALUATION OF CPP

Related to the mechanisms of filtration, infiltration, absorption, evaporation and reaction, knowledge of CPP pore characteristics are critical. Pore characteristics determine the physical behavior of porous materials to fluid, solute and particulate loadings. However, using many conventional gravimetric-geometric and destructive techniques it has been difficult to directly measure critical pore characteristics such as effective porosity (ϕ_e), tortuosity, pore size distribution $(PSD)_{pore}$ and (SSA) based on effective pores. Although research has been done on the pore characteristics for conventional pavements and porous materials in many other fields, there has been no methodological investigation of CPP pore structure.

Hydraulic conductivity (k) is one of the most important properties for a permeable pavement. High conductivity is desirable for CPP to let water infiltrate into sub-base layer as soon as possible to reduce or even avoid runoff. Although much research has been carried out for many kinds of porous media, such as soils, rocks, and filters and many empirical models were

developed based on simplified or idealized media particle shape, little research has been carried out on CPP based on CPP's pore structure with high porosity, irregularly shaped pores and wide range of pore size distribution. Compared to other porous media, CPP has the characteristics of high porosity and low hydraulic head under empty bed conditions. It is very important to develop methodology to predict CPP hydraulic conductivity based on these pore characteristics and pore size distribution.

A very important function of CPP is filtration. Studies have demonstrated that particles are the main vector of runoff pollution (Colandini et al. 1995; Teng and Sansalone 2004). Combined with engineered adsorptive-filter media, cementitious porous pavement (CPP) functions as a primary unit operation/process and a capable infiltration-exfiltration BMP in removing both soluble and particulate pollutant from stormwater (Fujita 1993; Jahangir-Issa 1998; Legret et al. 1999; Pratt et al. 1989; Sansalone 1999; Teng and Sansalone 2004; Yu 1993). Due to the formation of schumutzdecke which functions as a filter cake and aids particle removal, and protects deeper specific deposits, CPP can remove finer particles less than 25 μm (Sansalone 1999, Teng and Sansalone 2004).

Clogging potential is one of the most common concerns of permeable pavement, and the useful life of permeable pavement depends on maintaining a high drainage capacity (Fwa, et. al. 1999; Schlüter and Jefferies 2002, Tan et al. 2003). It is critical to correctly predict clogging based on hydraulic loading rate, particulate loading and CPP properties, as well as cleaning the surface with proper methods before the infiltration rate drops to an unacceptable level.

With the urban development, more and more pollutants and acidity from acid rain flow to watersheds and deteriorate our water environment. One of the significant contributions of CPP for water quality control is that CPP is able to elevate the pH and alkalinity after water infiltrates

through it. The elevated alkalinity functions as a buffer, and neutralizes acids. In waters with low alkalinity, pH might fluctuate from 5 or lower to as high as 9 or above; while in high alkalinity waters, pH might fluctuate from about 7.5 to 8.5. Alkalinity levels of 20-200 mg/L are typical of fresh water. A total alkalinity level of 100-200 mg/L will stabilize the pH level in a stream. Levels below 20 mg/L indicate that the system is poorly buffered, and is very susceptible to changes in pH from natural and human-caused sources. Above pH 9.5 (usually well above pH 10), OH^- alkalinity can exist or CO_3^{2-} and OH- alkalinities can coexist together.

The excess release of phosphorus (P) into surface water is of an increasingly environmental concern, because P is a major cause of eutrophication in most ecosystems, subsequently followed by massive algal blooms, fish suffocation and other undesired effects (Spivakov et al. 1999). The critical concentration of P above which the growth of algae and other aqueous plants accelerates is suggested as 0.01 mg/L for dissolved P and 0.02 mg/L for total P (Kim et al. 2003). Phosphorus in the elemental form is particularly toxic and is subject to bioaccumulation in much the same way as mercury (Spivakov et al. 1999). In comparison, dissolved P (as TDP) off I-10 of City Park in Baton Rouge can be as high as 1.0 mg/L and total P can be as high as 3.0 mg/L as an event mean concentration (EMC). Compared to asphalt porous pavement, one of the outstanding advantages of CPP for environmental benefits is the capability to removal phosphorus (Fach et al. 2002; Li et al. 1999; Park and Tia 2004; Pratt 1999).

CPP strength is also a main concern because it not only functions as a device for stormwater management but also provides a strong structure for traffic loading. Optimization of the mix design is critical to achieve a desirable high porosity for stormwater quality and quantity control and a high strength for traffic loading.

1.5 CONTENTS OF THE DISSERTATION

Chapter 2: Pore Characteristics of CPP by X-Ray Tomography Imaging

Pore characteristics, including total porosity ϕ_t, effective porosity ϕ_e, pore size distribution $(PSD)_{pore}$, specific surface area of based on solid volume, $(SSA)_s$, based on total pore volume, $(SSA)_{pt}$ and based on effective pores, $(SSA)_{pe}$, and tortuosity (L_e/L), critical to CPP functioning as an adsorptive, reactive, and filtration infrastructure, are examined by XRT analysis and conventional Geometric-Gravimetric methods. Relationships between pore parameters, such as ϕ_t-ϕ_e, ϕ_t-(L_e/L), and ϕ_t-(SSA) relationships were developed, so that ϕ_e, (L_e/L) and (SSA) which are otherwise very difficult to obtain by conventional measurements could be estimate based on CPP geometric-gravimetric properties.

Chapter 3 Hydraulic Characteristics of CPP

This chapter examined hydraulic conductivity for CPP by constant-head experiments. Empirical models for CPP hydraulic conductivity estimation were evaluated. A modified Kozeny-Carman Model (MKCM) applicable for CPP hydraulic conductivity prediction based on CPP pore characteristics was developed. Pore space factors that influence hydraulic characteristics of CPP were investigated. Based on measurements, k-ϕ_t and k-ϕ_e relationships for predicting hydraulic conductivity *k* with known total porosity ϕ_e or ϕ_t were developed.

Chapter 4 Filtration and Clogging Potential of CPP

Main task of this chapter is to evaluate the infiltration and clogging properties of CPP. Particle removal efficiency of CPP was evaluated experimentally for different particle sizes and under different particle loading concentration. The clogging process of CPP materials was evaluated by measuring the temporal hydraulic conductivity. A methodology to calculate the cumulative strained particles on CPP surface and examine the size distribution of particles

strained on CPP surface was developed. A relationship between turbidity and TSS was developed based on experimental measurements. The methods for infiltration rate recovery and maintenance schedule estimation for CPP surface were presented.

Chapter 5 Chemistry Properties of CPP

This chapter focuses on CPP functions as a reactive and absorptive material for acid neutralization and phosphorus removal from stormwater. pH and alkalinity elevation properties of CPP were investigated. Phosphorus removal properties of CPP, including total phosphorus (TP), total dissolved phosphorus (TDP) and total particulate phosphorus (TPP) removal efficiency after infiltrating through CPP were evaluated. The relationship of removed total solids suspension (TSS) and TPP was also presented based on experimental measurements.

Chapter 6 Optimization Mix Design

The main task of this chapter is to recommend a good mix design by which a CPP material could be achieved with desirable strength ($f_c' > 3000$ psi) for traffic loading and expected porosity ($\phi_t >$ 20%) for rainfall-runoff quality and quantity control. Focusing on this task, a number of objectives related to the mix design of CPP functioning as an infiltration/evaporation interface, a conveyance/storage medium, a filtration material, and a reactive material were achieved. The influence of water to cement ratio (w/c), aggregate gradation and aggregate to cement ratio (a/c) on strength and porosity of CPP was investigated. Relationships of w/c –porosity, w/c –strength, a/c-porosity, a/c-strength were presented. The influence of compaction degree on both porosity and strength was also evaluated for CPP. A relationship between porosity and compressive strength, f_c', was developed for CPP materials. The correlation between compressive (f_c') and splitting tensile strength (f_s) for the designed CPP materials was developed. Hydraulic conductivity (k) of the designed CPP, and the relationship of k-ϕ_t were also presented.

1.6 REFERENCES

Asaeda, T., and Ca, V.T. (2000). "Characteristics of permeable pavement during hot summer weather and impacton the thermal environment." *Can. Build. & Env.,* 35, 363-375.

Andersen, C.T., Foster, I.D.L., and Pratt, C.J. (1999). "The role of surfaces (permeable pavement) in regulating drainage and evaporation: development of a laboratory simulation experiment." *Hydrological Processes*, 13, 597-609.

Aulenbach, D.B. and Y.Y. Chan, 1988, "Heavy meal removal in a rapid infiltration sand column", *Particle. Sci. Tech*. 6, pp 467-481.

Bäckström, M. (2000). "Ground temperature in porous pavement during freezing and thawing." *Journal of Transportation Engineering, ASCE*, 375-381.

Bäckström, M. and Bergström, A. (2000). "Draining function of porous asphalt during snowmelt and temporary freezing." *Can. J. Civil. Eng.*, 27, 594-598.

Balades, J-D. , M. Legret and H. Madiec, 1995, "Permeable pavements: pollution management tools." Wat. Sci. Tech. Vol. 32, No. 1, pp. 49-56.

Bérengier, M.C., Stinson M.R., Daigle, G.A., and Hamet, J.F. (1997). "Porous road pavements: Acoustical characterization and propagation effects." *Journal of Acoustic Society of America*, 101(1), 155-162.

Brattebo, B.O., and Booth, D.B. (2003). "Long-term Stormwater quantity and quality performance of permeable pavement systems." *Water Research*, 37, 4369-4376.

Colandini, V., M. Legret, and J. D. Balades, 1995, "Metallic pollution in clogging materials of urban porous pavements." *Wat. Sci. Tech*., Vol. 32, No. 1, pp. 57-62.

Fach, Dipl.-Ing. S., Prof. Dr.-ing. W.F. Geiger, Dr.-Ing. C. Dierkes, 2002, "Development of an assessment procedure for permeable pavements." University of Essen, Urban Water Management, Universitaesstr. 15, 45141 Essen, Germany, pp. 1-12.

Fach, S., Geiger, W.F. and Dierkes, C. (2002). "Development of an assessment procedure for porous pavements." *9th Conference on Urban Drainage 2002 in Portland.*

Field, R., Masters, H., and Singer, M. (1982). "Porous pavement: research; development; and demonstration." *Journal of Transportation Engineering*, *ASCE*, 108, 244-258

Fujita, S., 1993, "Infiltration in congested urban areas of Tokyo", Proc. 6th Int. Conf. on Urban Storm Drainage, Vol. 1, pp993-998.

Fwa, T. F., Tan S. A., and Y. K. Guwe, 1999, "Laboratory evaluation fo clogging potential of porous asphalt mixtures." *J. Tran. Eng., ASCE*, pp. 43-49.

Ghafoori, N., and Duta, S. (1995). "Laboratory investigation of compacted no-fines concrete for paving materials." *Journal of Materials in Civil Engineering*, *ASCE*, 7(3), 183-191.

Giménez, D., Allmaras, R.R., Huggins, D.R. and Nater, E.A. (1997). "Prediction of the Saturated Hydraulic Conductivity-Porosity Dependence Using Fractals." *Soil Science Society of America*, 5, 1285-1292.

Hot Mix Asphalt Technology-September/October 2003, 26-40

Isenring, T. H. Koster, and I. Scazziga, 1990, "Experience with porous asphalt in Switzerland." *Transportation Research Record 1265*, pp. 41-53.

Jackson, T.J. and Ragan, M. (1974). "Hydrology of porous pavement parking lots." *Journal of the Hydraulics Division*, 1739-1752.

Jahangir, I., 1998, "Rainwater and its infiltration importance in Iran." *Pro., 3rd Int. Conf. on Innovative Technologies in Urban Storm Drainage*, Vol. 2, pp 475-485.

Jimenez, F.E.P. and M.A.C. Perez, 1990, "Analysis and evaluation of the performance of porous asphalt: the Spanish experience." *Surface Characteristics of Roadway: International Research and Technologies*, ASTM STP 1031, W. E. Meyer and J. Reichert, Eds., American Society for Testing and Materials, PA, pp. 512-527.

Kobayashi, T., Kagata, M., Kodama, T., and Ito, M. (2002). "Development of the environment-friendly hybrid permeable concrete." *Transactions of the Japan Concrete Institute*, 23, 65-76.

Kuennen T. (2003). "A new era for permeable pavement." *Road Science-Better Road*, 28-32.

Legret, M. , M. Nicollet, P. Miloda, V. Colandini, and G. Raimbault, 1999, "Simulation of heavy metal pollution from stormwater infiltration through a porous pavement with reservoir structure." *Wat, Sci. Tech*. 39(2), pp. 119-125.

Legret, M. and V. Colandini, 1999, "Effects of a porous pavement with reservoir structure on runoff water: water quality and fate of heavy metals." *Wat. Sci. Tech*. 39(2), pp. 111-117.

Li, Y.B., Buchberger, S.G., and Sansalone, J. (1999). "Variably Saturated Flow in Storm –Water Partial Exfiltration Trench." *Journal of Environmental Engineering*, *ASCE*, 556-565

Miller, A.R., 1989, *Porous pavement: pavement that leaks.*

Niemczynowicz, J. (1989). "Swedish way to storm water enhancement by source control." *Urban Stormwater Enhancement-Source Control, Retrofitting and Combined Sewer Technology*, *Urban Water Resource Research Council*, American Society of Engineers, New York, 156-158.

Oke T. (1982). "The energetic basis of urban heat island." *Quar. J. Roy. Met. Soc*. 108, 1-24

Park, S. B. and M. Tia, 2004, "An experimental study on the water-purification properties of the porous concrete." *Cement and Concrete Research*, Vol. 34, pp. 177-184.

Pratt, C.J., 1999, "Use of permeable, reservoir pavement constructions for stormwater treatment and storage for re-use". Wat. Sic. Tech., 39(5), pp 145-151.

Ranieri V. (2002). "Runoff control in porous pavement." *TRB* 1789, Paper no. 02-3476, 46-55

Sansalone, John J., 1999, "Adsorptive infiltration of metals in urban drainage-media characteristics." The Science of the Total Environment 235 pp. 179-188.

Sansalone, J.J., Koran, J.M., Smithson, J.A., and Buchberger, S.G. (1998). "Physical characteristics of urban roadway solids transported during rain events." *J. Environ. Eng*., 124(5), 427-440.

Sansalone, John J., 1999, "In-sity performance of a passive treatment system for metal source control." Wat. Sci. Tech. Vol, 39, No. 2, pp.193-200.

Schluter, W. C. Jefferies, 2002, "Modelling the outflow from a porous pavement." *Urban Water*, 4, pp. 245-253.

Spivakov, B.Y., T.A. Maryutina and H. Muntau, 1999, "Phosphorus Speciation in water and sediments." *Pure Appl. Chem*., 71(11), pp 2161-2176

Stotz, G. and K. Krauth, 1994, "The pollution of effluents from pervious pavement of an experimental highway section: first results." *The Science of the Total Environment*, 146/147, pp. 465-470.

Teng, Z. and J.J. Sansalons, 2004, "In situ partial exfiltration of rainfall runoff. II: particle separation", *Journal of Environmental Engineering*, *ASCE*, 130(9), pp 1-13.

Wada, Y., H. Miura, R. Tada and Y. Kodaka, 1997, "Evaluation of an improvement in runoff control by means of a construction of an infiltration sewer pipe under a porous asphalt pavement." *Wat. Sci. Tech*, 36(8-9) pp397-402

Watanabe, S. (1995). "Study on storm water control by permeable pavement and infiltration pipes." *Water Science Technology*, 32(1) 25-32.

Xu, D., A. Mermoud, 2003, "Modeling the soil water balance based on time-dependent hydraulic conductivity under different tillage practices." *Agr. Wat. Manag.*, 63, pp. 139-151.

Yu, S. L., 1993, "Stormwater management for transportation facilities." National Cooperative Highway Research Program, Synthesis of Highway Practice, *Transportation Research Board*, Washington, D. C.

CHAPTER 2 X-RAY TOMOGRAPHIC EXAMINATION OF PORE CHARACTERISTICS FOR CPP

2.1 INTRODUCTION

Permeable pavement, also called pervious pavement, is a pavement structure in which cemented aggregate can produce hydraulically-conductive pore characteristics throughout the pavement structure (Berengier et al. 1997). Such pore characteristics permit gravitational drainage, capillary movement, evaporation, gaseous transport, precipitation and dissolution reactions, and filtration mechanisms. One common form, cementitious permeable pavement (CPP) consists of Portland cement, graded granular aggregate and water (Li et al. 1999).

CPP has generated increasing interest of a wide range of stakeholders over the last several decades (HMAT 2003). Research has shown that the degree of imperviousness in the built environment is correlated to deleterious hydrologic, climate and environmental impacts (Bäckström 2000; Field et al. 1982; Jackson et al. 1974; Kuennen 2003). Examples of hydrologic impacts include increased discharges, increased flooding, channel incision, bank erosion, and increased sediment transport (Andersen et al. 1999; Bäckström and Bergström 2000; Brattebo and Booth 2003; Watanabe 1995). Examples of local climate impacts include generation of higher temperature in urban areas as compared to surrounding rural areas resulting in urban heat islands (Kobayashi et al. 2002; Oke 1982). Examples of environmental impacts include significantly increased loading and delivery of anthropogenic constituents such as metal elements, nutrients, organics, and particulate matter discharged to the environment (Bäckström and Bergström 2000; Ghafoori and Dutta 1995; Sansalone and Teng 2004). With respect to these impact categories, CPP reduces rainfall-runoff peak, volume, improves water quality through

physical and chemical mechanisms, facilitates groundwater and interflow recharge (HAMT 2003; Ranieri 2002), and mitigates temperature increases (Asaeda and Ca 2000).

2.1.1 The Role of Pore Characteristic Measurements for Porous Structures

Pore characteristics determine the physical behavior of porous materials to fluid, solute and particulate loadings. Therefore, there has been a wide range of research disciplines interested in the many aspects of pore characteristics. These areas include soil and rock science (Giménez et al. 1997; Meegoda 1989), conventional pavement (Cooley and Brown 2000; Hall et al. 2001; Harvey 1994; Huang et al 1999; Masad et al 1998; Maupin 2000; Mohammad et al. 2003; Wang et al. 2003; Yue et al 1995; Zube 1962), environmental engineering (Li et al. 1999; Sansalone and Teng 2004); fluid mechanics (Dardis and McCloskey 1998; Hilpert et al. 2001; Lebron et al. 1999), and porous media (Choubane et al. 1998; Fach et al. 2002; Flint and Selker 2003; Nakashima and Watanabe 2002).

However, using many conventional gravimetric-geometric and destructive techniques has been difficult to directly measure critical pore characteristics such as effective porosity (ϕ_e), tortuosity, pore size distribution $(PSD)_{pore}$ and (SSA) based on effective pores. For example, ϕ_e rather than total porosity (ϕ_t) has been demonstrated as a critical factor that determines the hydraulic characteristics of porous structures (Al-Omari, et al. 2002; Flint and Selker, 2003). Despite this recognition, many evaluations of porous structures still rely on measurement of ϕ_t due to simplicity and economy of measurement as compared to ϕ_e (Harvey 1994; Kanitpong et al. 2003; Krishnan et al. 2001; Masad et al. 1998; Mohammad et al. 2003; Yue et al. 1995).

The flow path of the liquid through a porous medium is commonly approximated in terms of tortuosity (Al-Omari, et al. 2002; Zhang and Knackstedt 1995). Tortuosity is difficult to measure directly (Al-Omari, et al. 2002; Dullien 1992; Saripalli et al. 2002; Scheidegger 1974).

By assuming that fluid-flow and electrical current follow equivalent flow paths in porous solids, a common approximation estimation of hydraulic tortuosity is to measure electrical conductivity on the same porous media saturated with electrolyte with known conductivity, but some research showed that this assumption was not valid (Zhang and Knackstedt 1995). Because of its difficulty of measurements, tortuosity is usually assumed as 1.414 based on equally-sized spherical granular material in the porous medium and the assumption that the fluid pathway is along the diagonal of a rhombic packing structure of these spheres (Carman 1956). However, some experiments have found values as high as 2.5~7 and dependant on porosity (Saripalli et al. 2002, Zhang and Knackstedt, 1995).

The $(PSD)_{pore}$ influence hydraulic and filtration characteristics of a porous medium (Lebron et al. 1999, Nakashima and Watanabe 2002). For example, to predict filtration or clogging behavior of a porous medium such as CPP, various PSD indices have been examined. Investigations utilize d_{50} indices for the $(PSD)_{pore}$ and the filtrate particle size distribution (PSD) to suggest filtration mechanisms (Li et al. 1999; McDowell et al. 1986, Sansalone and Teng 2004). Other research has shown that ratios for the size indices of the d_{15} of the filter and d_{85} of the filtrate can be used to examine filtration mechanisms (Sherard, et al. 1984, 1989).

SSA influences the hydraulic characteristics of porous media (Al-Omari et al. 2002; Masad et al. 1998; Saripalli et al. 2002). SSA is usually defined as the ratio of the surface area to the volume of the particles when porous medium function as a filter. For spheres, SSA = 6/D, where D is the diameter of the sphere (Metcalf and Eddy 2003). However, in CPP, the pore volume interface to the solid structure surface is irregular. Flow characteristics are controlled by the pore space geometry rather than the solid matrix (Nakashima and Watanabe 2002; Zhang and Knackstedt 1995). SSA based on the ratio of the pore-solid interfaces to the volume of total

pores or effective pores, denoted as $(SSA)_{pt}$ and $(SSA)_{pe}$, respectively, are necessary to predict hydraulic conductivity and other flow characteristics (Nakashima and Watanabe 2002), but little research has been done due to the difficulty of pore connectivity determination.

Although research has been done on the pore characteristics for conventional pavements and porous materials in many other fields, there has been no methodological investigation of CPP pore structure. At the same time, it is necessary to recognize that ϕ_e, $(PSD)_{pore}$, $(SSA)_{pe}$, and (L_e/L) influence the hydraulic characteristics and filtration performance of CPP as a LID material and unit operation for rainfall-runoff management.

2.2 OBJECTIVES

This study had a number of objectives related to the pore characteristics of CPP, as these pore characteristics provide inputs for modeling of CPP material as an infiltration/evaporation interface, a conveyance/storage medium, a filtration material, and a reactive material. The first objective was measurement of CPP pore characteristics, specifically, ϕ_t, ϕ_e, $(PSD)_{pore}$, $(SSA)_{pt}$ and $(SSA)_{pe}$ and (L_e/L) by x-ray tomography, gravimetrics and geometrics. The second objective was examination of the $(\phi_t - \phi_e)$ relationship. The third objective was determination of a correlation between $(PSD)_{pore}$ and SSA. The fourth objective evaluated the tortuosity range and distribution for CPP. The final objective examined how image resolution influenced results when x-ray tomographic imaging was employed.

2.3 BACKGROUND

2.3.1 Conventional Methods of Determination of Pore Characteristics for Pavements

There have been many attempts, theoretical and experimental, to determine relationships between microstructure (pore structure characteristics) and transport properties of single phase or multiphase flows (Lindquist and Lee 1996). ASTM C 457 Standard (1990) introduced two

principal methods for microscopic determination of parameters of pore space in hardened concrete; the linear traverse method and the modified point-count method. These methods can only be applied to sawed and lapped plane sections of a specimen, and can not examine the internal structure in a non-destructive way. Eriksen and Wegan (1993) used microscopy to examine pore space in asphalt concrete. Their efforts focused on the methodology of microscopy more than quantifying the pore space distribution. Roberts et al (1994) analyzed factors such as sample preparation, image processing procedures and the concrete air-void system itself that influence microscopic image analysis of porosity in hardened concrete. Berryman and Blair (1986) estimated fluid permeability utilizing digitalized microscopic images.

As an effective non-destructive technique (NDT), X-ray tomography (XRT) has brought revolutionary changes to medical diagnosis and medical science since 1970s (Wang et al. 2003), and it has been increasingly used to help examine pavement internal microstructure in recent years (Braz et al. 1999; Hall et al. 2000; Landis and Denis 1999; Shashidhar 1999; Wang et al. 2001, 2003). Compared to conventional destructive methods, XRT has the advantage of imaging the internal structure in a non-destructive manner with high accuracy. For example, image analysis can correctly assess pore characteristics as defined in ASTM C 457 (Pleau et al. 2001).

2.3.2 Methods for Image Processing

There are two critical steps in image processing. The first step is to determine the threshold to transfer gray images into binary images thereby separating or segmenting pores from solid structure. Many methods have been presented for image segmentation (Jain and Dubisson 1992; Lindquist et al. 1996; Leu 1992; Roberts et al 1994). Jain and Dubisson (1992) compared 3 widely accepted algorithms to segment X ray images: (i) thresholding based on Bayes decision theory in pattern recognition. A cutoff threshold is between the peaks of the

object (pore) and background (solids), and based on Bayes theory of pattern recognition. Any pixel with an attenuation coefficient greater (less) than the cutoff is identified as grain (void). The aim of the decision is to assign an object to a binary class; (ii) adaptive thresholding is used when there is a large range of variation in array values from one part of the image to the other, a single fixed threshold cannot be used for the entire image. By dividing the image into several sub-images, adaptive thresholding assigns a different threshold value to each pixel, and (iii) iterated conditional modes, which can be used to threshold dirty images with low quality. However, if the grey images are not of high quality, the simplest way of segmentation is by observation and comparison of the original gray image and the transferred binary image, as long as only a small amount of noise (fine pores) is generated, and the area of easily identified coarse pores are unchanged before and after segmentation.

The second step is to reconstruct 3D specimen based on 2D images. Because the spacing between image slices is much larger than the resolution of image plane, interpolation is required to make a smooth boundary of the reconstructed 3D specimen (Raya and Udupa 1990; Wang et al. 2001). For regularly shaped images of similar sizes, however, it is reasonable to simply interpolate the values of the gray level between two slices (Jin et al. 1992). Recognizing that the spacing between two slices is the most important factor, Wang et al (2001) presented a linear proportional erosion method for reconstruction interpolation.

2.4 METHODOLOGY

2.4.1 CPP Specimens

Cored specimens were taken from CPP material constructed as the surface interface of a partial exfiltration reactor (PER). The PER is a linearly-extended in-situ rainfall-runoff unit operation and process whose primary components include (i) a structural CPP surface allowing

urban pavement sheet flow infiltration, particulate straining/filtration, pH/alkalinity modification while acting as a structural surface supporting wheel loads, and (ii) a reactive adsorptive-filtration medium located below the CPP surface. Details of the PER system with a CPP component and PER performance are provided elsewhere (Li et al 1999, Sansalone and Teng 2004, Teng and Sansalone 2004). After 3 years of exposure a total of 21 specimens were cored from CPP material taken from the PER surface (mean pH = 6.8, mean suspended solids ≈ 200 mg/L), from control CPP material at the site exposed to only rain (mean pH = 4, mean suspended solids < 1 mg/L), and from control CPP material not exposed to any rainfall or runoff during this period (Sansalone et al 1998). All but two cores were backwashed with tap water (pH = 7 and alkalinity ≈ 150 mg/L as $CaCO_3$) to remove any runoff particles from field CPP material or abraded particles generated in the coring process. Saturated hydraulic conductivity in the range of 10^{-2} to 10^{-3} cm/second facilitated the backwashing process (Teng and Sansalone 2004). Geometric and gravimetric measurements of each core are shown in Table 2-1.

2.4.2 Pore Characteristics through Gravimetric-Geometric Evaluations

2.4.2.1 Experimental Measurement of Specific Gravity (ρ_s) and $(SSA)_s$

Measurements of ρ_s were made to gravimetrically determine total porosity (ϕ_t).

$$\phi_t = \frac{\text{volume of pores}}{\text{bulk volume of specimen}} = \frac{\text{bulk volume - solid volume}}{\text{bulk volume}} = \frac{V_b - V_s}{V_b} = 1 - \frac{W/\rho_s}{V_b} \qquad (2\text{-}4)$$

In this expression W is the specimen dry weight and V_b the bulk volume of a specimen, and V_s is the solid volume. To determine CPP ρ_s, CPP material was ground into a powder. This material was taken from the proximity of where the CPP specimens were cored. After grinding, the CPP powder was dried in a hot room at 40°C until the weight stabilized. The CPP powder was then cooled and remained dry in a dessicator. This procedure follows

ASTM D- 421 (1999). The measurement of specific gravity followed ASTM D 5550-4 (1994) through inert gas pycnometry. The gas utilized in this procedure was ultra-high pure *He* for inertness and ability to enter pore space approaching 1 angstrom (10^{-10} m) in diameter. Triplicate aliquots were analyzed for each test. Table 2-2 summarizes S_g measurements. Based on S_g, total porosity of CPP cores can be estimated by equation (2-4).

Table 2-1 Geometric and gravimetric indices of CPP specimens

Specimen Code[1]	Dry Weight (g)	Diameter (cm)	Height (cm)	Bulk Volume (cm^3)	Solid Volume (cm^3)	Bulk Density (kg/m^3)
C1-5	857.48	6.89	9.60	376.61	322.36	2194.40
C2-1	785.44	7.03	9.60	357.93	295.28	2147.79
C2-3	800.31	7.00	9.65	372.62	300.87	2148.58
C2-5	797.94	6.90	9.72	371.38	299.98	2215.57
C2-6	804.85	7.01	9.68	363.27	302.58	2103.00
C2-11	785.68	7.01	9.65	373.60	295.37	2002.79
C2-12	745.92	7.01	9.70	372.44	280.42	2324.06
LC2-8	870.06	6.93	9.60	374.37	327.09	2388.54
LC1-4	863.65	6.94	9.60	361.58	324.68	2340.33
LC1-5	848.65	6.92	9.74	362.62	319.04	2367.89
LC1-6	867.83	6.97	9.76	366.50	326.25	2167.78
LC2-2	807.67	6.92	9.60	372.58	303.64	2258.11
LC2-9	815.54	7.00	9.70	361.16	306.59	2095.69
LC2-10	782.32	6.99	9.64	373.30	294.11	2201.75
N1-4	814.56	7.05	9.62	369.96	306.23	2184.50
N2-10	820.74	6.96	9.73	375.71	308.55	1978.14
S1-4	732.05	7.07	9.75	370.07	275.21	1915.61
S1-5	732.05	7.10	9.79	382.15	275.21	1873.53
S1-8	725.00	6.90	9.65	386.97	272.56	2113.49
S2-2	762.95	6.90	9.63	360.99	286.82	2049.00
S2-4	738.48	6.89	9.60	360.41	277.62	2194.40

[1]: Specimen Code:
C: field control, LC: lab control,
N and S: extracted from field site PER;

- PER: partial exfiltration reactor;
- CPP: Cemetitious Permeable Pavement;
- Specimens were taken from CPP surface for PER;
- The D_{50} of the fine aggregate (sand) in the mix design was 2.00 mm;
- The D_{50} of the coarse aggregate (gravel) in the mix design was 6.30 mm;
- The mix design water/cement ratio was 0.3 and the mass ratio of sand to gravel was 1;
- The 28-day f'_c for CPP > 4000 psi (27580 kPa)

Table 2-2 Inert gas pycnometer measurements of specific gravity (ρ_s) for CPP specimens

V_c [1]	V_r [1]	P_1 [2]	P_2 [2]	V_p [3] (cm^3)	Weight W (g)	ρ_s [4]
25.644	13.964	17.645	7.397	6.298	16.769	2.663
		17.454	7.310	6.266	16.769	2.676
		17.502	7.332	6.275	16.769	2.672
25.644	13.964	18.565	7.985	7.142	18.998	2.660
		16.847	7.245	7.137	18.998	2.662
		16.785	7.220	7.145	18.998	2.659
147.499	91.281	17.118	8.494	54.821	145.438	2.653
		17.864	8.865	54.838	145.438	2.652
		17.308	8.592	54.901	145.438	2.649
147.499	91.281	17.203	8.436	52.636	139.829	2.657
		17.196	8.435	52.690	139.829	2.654
		17.184	8.430	52.710	139.829	2.653
Mean (μ)						2.659
Standard Deviation (σ)						0.008

[1]: Coefficients of the inert gas (He) pycnometer, for medium cell, V_c=25.644, V_r=13.964; for the large cell, V_c=147.499, V_r=91.281;

[2]: Pressure of inert gas *He*, read from pycnometer before and after test;

[3]: Solid Volume, $V_p = V_c - V_r(\frac{P_1}{P_2} - 1)$;

[4]: Specific Gravity, $\rho_s = \frac{\text{solid weight W}}{\text{solid volume V}_p} / (1000\ \text{kg/m}^3)$

2.4.2.2 Specific Surface Area $(SSA)_s$ by EGME Measurements

$(SSA)_s$ is denoted as the ratio of area of pore-solid interfaces to solid mass or volume. A modified EGME (ethylene glycol monoethyl ether) method (Sansalone et al. 1998) was utilized for experimental determination of SSA. Granular activated carbon (GAC) with known SSA values of 1000-1100 m^2/g (Calgon 1995) was employed to serve as control for the precision and accuracy of the EGME method. CPP cores with 70 mm diameter were sawed into thin slices of 1-2 mm thickness or utilized as crushed material with diameters from 1 to 10 mm. Each measurement of SSA was carried out using triplicate samples. $(SSA)_s$ results ranged from 0.5 to

2 m^2/g, or 1.33 - 5.32×10^6 m^2/m^3 (based on CPP specific gravity of 2.659), as Table 2-3 illustrated.

Table 2-3 Specific surface area measurements (based on solid mass) for CPP using EGME

Sample[1]	Sample Description	Dry Sample mass M_S (g)	Absorbed EGME M_E (g)	$(SSA)_s$[2] (m^2/g)	Average $(SSA)_s$ (m^2/g)	St. Dev.
D_1	Concrete discs cut from CPP core, h =1 mm, d=70 mm	44.8499	0.0059	0.4600	0.5306	0.080
D_2		42.1898	0.0062	0.5138		
D_3		48.0901	0.0085	0.6180		
S_1	Disc fragments, h=1 mm	4.5588	0.0016	1.2272	1.2020	0.065
S_2		8.0559	0.0026	1.1285		
S_3		12.0237	0.0043	1.2504		
P_1	Crushed CPP particles, d =1 to10 mm	29.1008	0.0137	1.6461	1.7100	0.238
P_2		31.2428	0.0135	1.5108		
P_3		29.7690	0.0168	1.9732		
GAC_1	Granular activated carbon	1.0009	0.3076	1074.686	1061.669	32.510
GAC_2		1.0006	0.3107	1085.652		
GAC_3		1.0005	0.2932	1024.667		

[1]: Sample D, S and P are cut from a CPP core.

[2]: $(SSA)_s$: specific surface area (m^2/g) based on solid mass, $(SSA)_s = M_E/(0.000286\times M_S)$

[3]: GAC: granular activated carbon, with known $(SSA)_s = 1000\sim1100$ m^2/g

2.4.3 X-Ray Tomography Imaging

The XRT system used in this study is the ACTIS system made by BIO-Imaging Research, Inc., consisting of a *250* kV X-ray tube, a part manipulator, and an image intensifier. During operation the X-ray beam penetrates the specimen, and X-ray intensity is attenuated, depending on the density of scanned materials. The image intensifier records all attenuation information and forms gray images in which different material constituents are represented by different brightness levels. The part manipulator holding the specimen rotates automatically during scanning so that the image intensifier can collect all attenuation information from all angles. The maxima scanning range and space between two slices can be controlled by adjusting the position of the manipulator. Before scanning, great care must be taken to calibrate the XRT system. It is

necessary to do vertical, horizontal, central and wedge calibrations, to make certain that the XRT system adjusts suitable X-ray intensity depending on scanned specimens and acquires images with consistent lightness. Figure 2-1 illustrates the XRT system and schematic methodology.

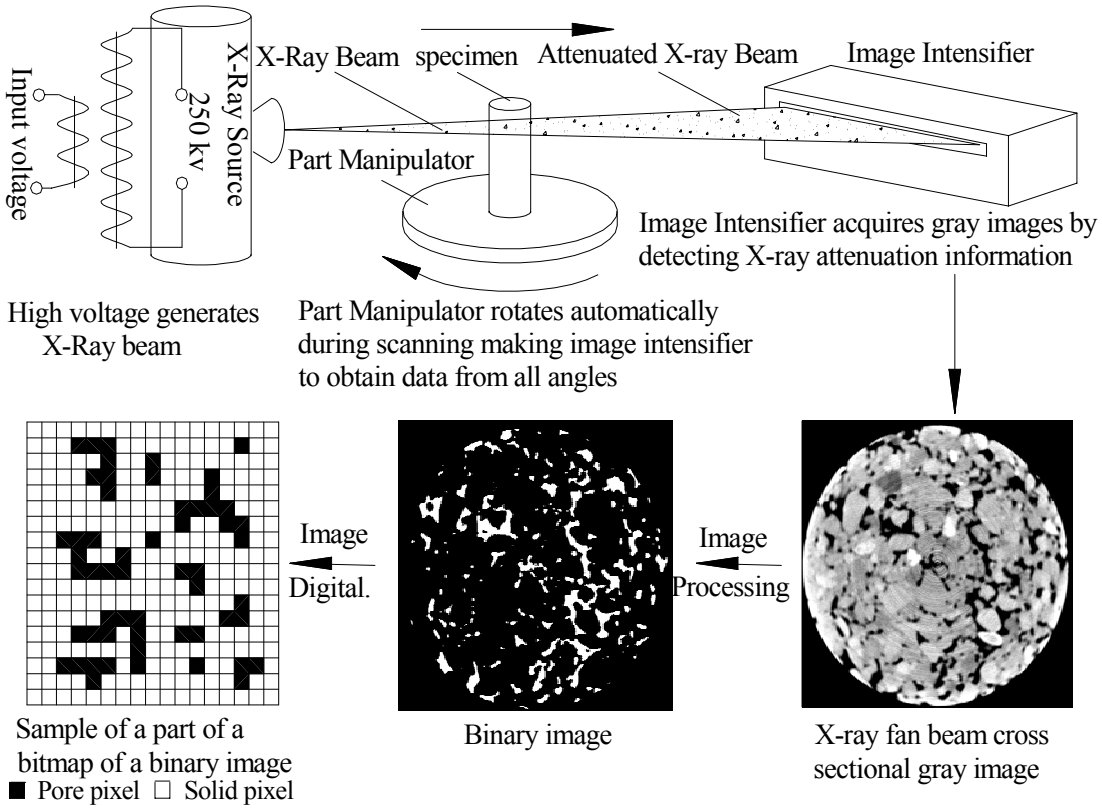

Figure 2-1 This Figure illustrates the methodology by which pore space geometry is determined through X-ray tomography, resulting gray image, image processing, and image digitalization. Each specimen was approximately 97 mm in height, 70 mm in diameter, and an image analysis was obtained at 0.5 (mm) intervals of specimen depth.

Before scanning, each specimen was dried in a hot room at a temperature of 40°C until the weight difference between two weighting less than 0.5 mg, cooled and scanned immediately. In this study, the spacing interval between two slices was 0.5 mm. Each image/slice is divided by 2048*2048, namely, 4194304 pixels, yielding an image resolution of 35 μm (0.0012 mm^2/pixel).

2.4.4 Image Processing

After all images are acquired by XRT, the first step is to transfer these gray images to binary images (black and white images) which include only two constituents: void pixels and solid pixels, then air voids can be easily identified in the binary images. The methodology used for transferring is based on the Bayes Decision Theory of pattern recognition introduced by Jain and Dubuisson (1992). All images acquired were clear so that it was not necessary to divide images into several sub-images when thresholding. In binary images white pixels with value of 255 are considered to be air voids while black pixels with value of 0 represent solids. After determination of the threshold of each image, bitmap of each image can be obtained by image digitalization process. In bitmaps, each pixel is identified by its position as referenced by its row (y coordinate) and column (x coordinate), and its pixel value, 0 or 255. Figure 2-1 conceptually illustrates the procedure of image processing.

Since the spacing between adjacent image sections (0.5 mm) is much larger than the image resolution (35 μm), interpolation is needed during the 3D reconstruction. Both the linear proportional erosion method developed by Wang et al. (2001) and the pixel value interpolation between two slice (Jin et al. 1992) were applied.

2.4.5 Pore Connectivity Determination

Pore connectivity analysis is critical for pore characteristics determination. ϕ_e, $(SSA)_{pe}$, $(SSA)_{pt}$ and tortuosity τ are determined by pore connectivity analysis. There are 3 necessary steps for connectivity analysis.

(i) Pore identification

In each image slice, any connected pixels with values of 255 are a pore. While it is easy to conceptually visualize whether or not any two pixels belong to a phase, the computational

process is more involved in two-phase images. An identification methodology had to be designed to identify each pore automatically from the image analysis. This methodology required coding to locate and identify each pixel. Any two pixels are designated as having the same code if they are connected to each other as a same pore. Then each pore in slice z can be identified as *N(z ,k)*, where *z* is image/slice number, and k=1~n(z), representing the code of each pore, and n(z) represents the number of total pores in slice *z*.

(ii) Boundary determination for each pore

Each pore is defined by: number of rows N_r, the beginning row R_b, and the end row R_e, the beginning column $C_b\ (i)$ and the end column $C_e(i)$ of each row that it occupies, and the slice *z* where the pore exits. Then the boundary configuration of the *k*th pore in slice z can be defined.

$$\Omega(z,k) = f\{N_r, R_b, R_e, C_b(i), C_b(i), z\} \tag{2-1}$$

In this expression $z = 1,2,\ldots M$; $k = 1,2,\ldots n(z)$; $I = R_b \sim R_e$, and *M* is the number of total slices.

(iii) Connectivity analysis

To determine the pore connectivity properties from the first and second slice, if any two pores have any overlap, they are considered as connected with each other, and can be defined.

$$\Omega(1,k_1) \bigcap \Omega(2,k_2) \neq 0 \tag{2-2}$$

In this expression $i = 1,2,\ldots n(1)$; $k = 1,2,\ldots n(2)$. Then pore k_1 in slice 1 is connected with pore k_2 of slice 2. All pores in slice 1 and slice 2 connected with each other were recorded, and other pores in slice 1 and slice 2 are eliminated.

The next step is to use the recorded pores in the upper slice z to determine the connectivity with the next lower slice $z + 1$, and can be defined.

$$\Omega(z,k_1) \bigcap \Omega(z+1,k_2) \neq 0 \tag{2-3}$$

Pore k_1 in slice z and pore k_2 in slice $z+1$ then are recorded. Repeating this procedure, only those pores that have connection with the top slice and the bottom slice, defined as effective pores which form flow pathways are stored in terms of the void code in each slice $N(z, i)$. Since the configurations $\Omega(z, i)$ are known, configurations of all pathways are obtained.

With image processing and pore connectivity analysis, pore characteristics of ϕ_t, ϕ_e, $(PSD)_{pore}$, (SSA) and (L_e/L) were evaluated.

2.4.6 Total Porosity ϕ_t

For an isotropic system, the area fraction of a phase represented in a 2-D image will directly correspond to the volume fraction in 3-D. From image processing results, porosity was obtained as follows. M slices were scanned from a CPP sample, and the number of pixels with value of 255 was determined and designated as A_v, and total pixels occupied by the specimen cross section area of M slices is A, then total porosity can be determined.

$$\phi_t = \frac{A_v / M}{A / M} \times 100\% = \frac{A_v}{A} \times 100\% \tag{2-5}$$

In this expression A_v is the area of pores in all images. It is hypothesized that total porosity obtained by image analysis should agree well with that obtained by geometric-gravimetric measurements.

2.4.7 Effective Porosity ϕ_e

Effective porosity is defined as the ratio of the volume of all effective pores to the total gross volume of a specimen. Effective pores can be obtained by void connectivity analysis.

$$\phi_e = \frac{A_e}{A} \times 100\% \tag{2-6}$$

Total area of effective pores, A_e, was determined as follows.

$$A_e = \sum_{z=1}^{M} A_e(z) \tag{2-7}$$

In this expression $A_e(z)$ represents the area of effective pores in slice z, which can be obtained by void connectivity analysis.

2.4.8 Pore Size Distribution $(PSD)_{pore}$

The purpose of $(PSD)_{pore}$ analysis is to determine the size of pores; which is important for hydraulic and filtration performance prediction. Usually, the median size (d_{50}) is used to represent the PSD characteristics. However, most of the pore shape is irregular. It is much more convenient to use pore area rather than pore diameter to represent the distribution. Based on pore area, an equivalent diameter can be obtained. Pore area can be obtained by image analysis. Two criteria are considered here for pore area distribution: A_{50a}, median pore area based on area distribution, and A_{50n}, median pore area based on number distribution of all pores.

The A_{50n} was obtained by: (i) Sorting the area of all pores in ascending order; (ii) Determining the number of total pores N; and (iii) Determining the A_{50n} is the median area of all pores based on the number distribution. The A_{50a} was obtained by: (i) Sorting ascending pore size based on areas of all pores; (ii) calculating the total pore area in all slices of a specimen; (iii) calculating the ratio of each pore area to total pore area; (iv) summing the percentage greater or equal to each size; and (v) the A_{50a} is the area of the median pore with a cumulative percentage of 50%. Once the A_{50} is determined, the equivalent median diameter can be calculated.

$$d_{50} = \sqrt{4 \times A_{50} / \pi} \tag{2-8}$$

2.4.9 Tortuosity (L_e/L)

Tortuosity is defined as the ratio of the actual pathway length of fluid flow to the shortest distance from the top to the bottom of a specimen or system. Prediction of hydraulic

conductivity, and diffusion coefficients in both saturated and unsaturated zones requires knowledge of tortuosity. The methodology for tortuosity determination by tomography analysis is summarized.

(i) Calculation of the coordinates of the center point of each pore

For each pore, the number of rows N_r, the beginning row R_b and the end row R_e, the beginning column $C_b(i)$ and the end column $C_e(i)$ in each row that it occupies, and the slice z where the pore exits are determined. The center of each row can be determined as $x_i = (C_b(i) + C_e(i))/2$, and $y_i = i$. The area in terms of pixels in row i for that pore can be determined as $A_i = C_e(i) - C_b(i) + 1$ and therefore the centroid of the pore in slice z can be determined:

$$X_c = \frac{\int_A x_i A_i}{A} = \frac{\sum x_i A_i}{\sum A_i} \qquad Y_c = \frac{\int_A y_i A_i}{A} = \frac{\sum i A_i}{\sum A_i} \tag{2-9}$$

(ii) Distance between two centers of two connected pores

Two connected pores $N(z, k_1)$ in slices z and $N(z+1, k_2)$ in slice $z+1$ can be calculated.

$$l_e = \sqrt{[X_c(z,k_1) - X_c(z+1,k_2)]^2 + [Y_c(z,k_1) - Y_c(z+1,k_2)]^2 + l^2} \tag{2-10}$$

In this expression l is spacing between the two adjacent slices.

(iii) Weighting each pathway based on cross-sectional area of all pathways

Different pathways may have different cross-sectional areas which contribute differently to fluid flow. An average tortuosity may not reflect the contribution of different pathways (Al-Omari, et al. 2002; Zhang and Knackstedt 1995). As a result it is necessary to weight each pathway by its cross-sectional area. The weighting methodology employed here is to weight the pathway length between two adjacent slices based on its cross-sectional area. Suppose there are n pores in slice z that connect with slice z + 1, the weighted length of fluid flow between these

two slices can be calculated.

$$l_e(z) = \sum_{i=1}^{n} (l_{ei} A_i) / \sum_{i=1}^{n} A_i \tag{2-11}$$

In this expression A_i is the smaller cross-sectional area of two connected pores between the two adjacent slices.

(iv) Wighted Tortuosity calculation

Weighted tortuosity $(L_e/L)_w$ is calculated based on the following expression.

$$(\frac{L_e}{L})_w = \frac{\sum_{z=1}^{M-1} l_e(z)}{(M-1)l} \tag{2-12}$$

In this expression L_e is the sum of total weighted length between each of the adjacent slices, and L is the length of specimen.

2.4.10 Specific Surface Area (SSA)

As mentioned above, SSA measured using EGME results in the ratio of total area of all solid-pore interfaces to the solid mass. In many cases, for example for hydraulic characteristic prediction, however, rather than solid mass/volume, SSA based on the pore volume or effective pore volume is needed.

$(SSA)_{pt}$, defined as the ratio of surface area of total pores (S_{pt}) to total pore volume (V_{pt}), can be expressed as. In order to estimate SSA from 2-D images, an assumption usually made is that the constituent fraction between two adjacent slices (spacing = 0.5 mm) is the same as that of the two slices, and a void in a 2-D slice is considered as a straight cylinder-shaped 3-D pore. This cylinder-shaped 3-D pore has x-section shape (usually irregular) as it is in the 2-D slice, and height as the spacing between two slices. Based on this assumption, the area fraction (A_v) of a phase present in a 2-D image will directly correspond to its volume fraction (V_{pt}) in 3-D, and in a

similar framework, the fraction of a phase total perimeter (P_t)in 2D will directly correspond to the fraction of the total surface area (S_{pt})in 3-D, namely, $(SSA)_{pt} = S_{pt}/V_{pt} = P_t/A_{v.}$ However, Wang and Frost (2003) found that the straight cylinder assumption was not very reasonable, and always generated smaller SSA. Considering the existing of tortuosity, it's reasonable to involve this factor in SSA calculation through 2-D images. In this case, the un-weighted tortuosity should be employed (Berryman and Blair 1987). $(SSA)_{pt}$ could be expressed as

$$(SSA)_{pt} = \frac{S_{pt}}{V_{pt}} = (L_e / L)_0 . \frac{\text{total perimeter of all pores}}{\text{total x - section area of pores}} = (L_e / L)_0 . \frac{P_t}{A_v} \tag{2-13}$$

In this expression, P_t represents the total perimeter of all pores; A_v is total cross sectional area of all pores obtained by image analysis, and $(L_e/L)_0$ is un-weighted tortuosity.

In hydraulic conductivity and filtration performance prediction, effective porosity rather than total porosity is the critical factor to predict those characteristics. After obtaining all of the effective pores and their boundary by pore connectivity analysis, $(SSA)_{pe}$, defined as the ratio of total surface area of effective pores (S_{pe}) to effective pore volume (V_{pe}), can be calculated.

$$(SSA)_{pe} = \frac{S_{pe}}{V_{pe}} = (L_e / L)_0 . \frac{\text{total perimeter of all effective pores}}{\text{total x - section area of effective pores}} = (L_e / L)_0 . \frac{P_e}{A_e} \tag{2-14}$$

In this expression P_e represents the total perimeter of effective pores. Similarly, $(SSA)_s$, defined as the ratio of total surface area of all pores (S_{pt}) to total solid volume (V_s), can be represented as $(SSA)_s = S_{pt}/V_s$. Since $\phi_t = V_{pt}/(V_{pt} + V_s)$, where V_s is solid volume, $(SSA)_s$ can be represented as the following.

$$(SSA)_s = \frac{S_{pt}}{V_s} = \frac{\phi_t}{1 - \phi_t} (SSA)_{pt} \tag{2-15}$$

In this expression, S_{pt} is the surface area of all pores, and V_s is the total solid volume.

2.5 RESULTS AND ANALYSIS

Based on the methodology developed, pore characteristics of the 21 CPP specimens were analyzed. In order to measure how image resolution influences the image analysis results, nine resolutions, R_r, of 35 (0.0012), 46 (0.0022), 70 (0.0049), 92 (0.0086), 140 (0.0194), 183 (0.0346) 279 (0.0778), 366 (0.1382) and 558 (0.3111) μm (mm^2/pixel) were analyzed for each image. Table 2-4 summarizes pore characteristic results of image analysis based on resolution of 35 μm.

2.5.1 Total Porosity ϕ_t and Effective Porosity ϕ_e

Plot (a) of Figure 2-2 illustrates the total porosity based on image analysis and geometric-gravimetric measurements, respectively.

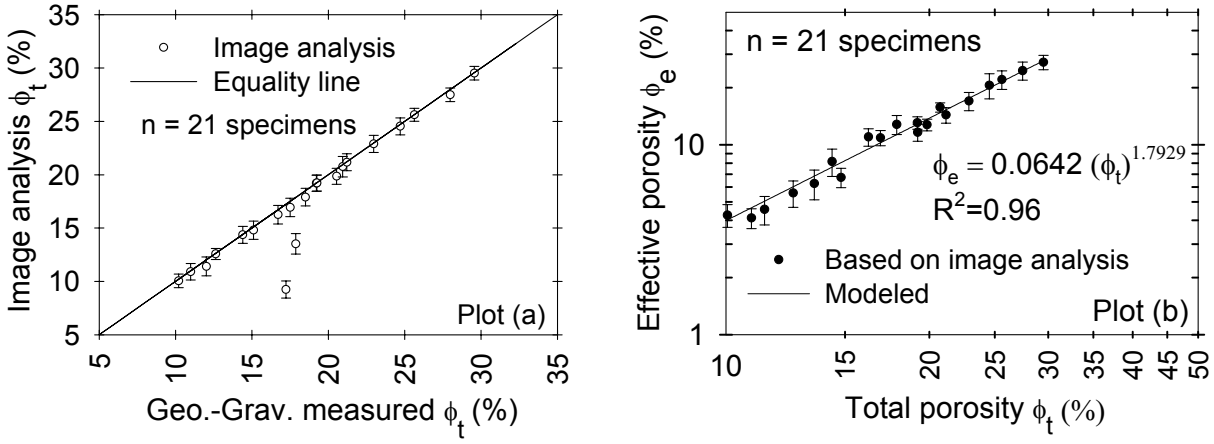

Figure 2-2 Plot (a) illustrates total porosity (ϕ_t) results of CPP specimens as determined by geometric-gravimetric measurements in comparison to image analysis measurements. Plot (b) illustrates a power law model fit of the relationship between total porosity ϕ_t and effective porosity ϕ_e.

Results indicate that for all specimens, image analyses agree well with gravimetric-geometric measurements, and the relative percent difference (RPD) for each specimen is less than 3%. Although the same coarse and fine gradations were used throughout the CPP as was the water/cement ratio, variability in the manufacture of the CPP was one reason that total porosities

ranged from approximately 10 to 30%. A second reason is that the CPP material from which specimens were cored, were exposed to differing leaching conditions had differing porosity. Specimens placed in the laboratory in a dry environment as control and not exposed to leaching from rainfall or runoff had the lowest porosity. Specimens with an intermediate porosity were those specimens cored from CPP of the PER and were exposed to sheet flow runoff with a mean pH of 6.8. Specimens with the highest porosity were those specimens from CPP material exposed only to rainfall (mean pH of 4.0) leaching on site. Two cores were taken from a north section of the PER that was not maintained by design to examine the role of clogging. For these two clogged cores, however, results indicate that the measured total porosity is much higher than that determined from image analysis. The reason is that some particulates clogged in the cores have a smaller specific gravity than that of CPP, and pore space occupied by clogged particulates was underestimated by geometric-gravimetric measurements, but tomographic images can help detect clogged space.

From Table2-4, it is found that the higher the total porosity, the higher the effective porosity. Since determination of pore connectivity and effective pores is a complicated process, it would be preferred to measure total porosity by gravimetric-geometrics and utilize a calibrated correlation between total porosity ϕ_t and effective porosity ϕ_e for a given mix design. The literature has shown that the relationship between total porosity and effective porosity follows a power law model (Al-Omari et al. 2002). Plot (b) of Figure 2-2 illustrates the strong relationship between ϕ_t and ϕ_e based on image analysis summarized in Table 2-4. The relationship for this mix design across a wide range of leaching conditions was determined.

$$\phi_e = 0.0642\phi_t^{1.7929} \tag{2-17}$$

With this model, ϕ_e could be obtained with know ϕ_t.

The coefficient of determination between effective and total porosity was $R^2 = 0.96$. Results suggest that given a calibrated power law model effective porosity can be estimated when total porosity is known. Results indicate that when total porosity is as high as 30%, effective porosity is nearly identical to total porosity since most pores have multiple connections with other pores under conditions of higher porosity. This is similar to the situation of sandy soils, but is not the case for materials such as clay materials with only 5% or less effective porosity despite total porosity that ranges from 30 to 50 % (Mcworter and Sunada 1977).

Error bars in Figure 2-2 represent standard deviation for replicate analyses of porosity. Results indicate that image resolution had little effect on total porosity and effective porosity analyses, because fine pores that may be neglected in low resolution images contribute little to area (volume) fraction. Therefore with respect to porosity, the XRT methodology has advantages with respect to constitutive volume (area) fraction analysis.

2.5.2 $(PSD)_{pore}$ and Influence of Image Resolution R_r

A main rationale for measuring $(PSD)_{pore}$ is to develop the required inputs to predict filtration function of CPP. Figure 2-3 illustrates the probability density function (pdf) of pore distributions from image analysis with resolution of 35 μm, based both on number and on area distribution of all pores in all slices for the 21 CPP cores. Range bars in Figure 2-3 represent the standard deviation of number distribution or area distribution. The pdf of the area distribution fits a Gaussian model, with $R^2 = 0.87$, where A_p is the pore area in mm^2.

$$pdf(a) = 0.3628(e)^{0.5(A_p - 9.21)^2 / 2.0524^2} \tag{2-18}$$

The pdf of the pore number distribution fits an exponential model with an $R^2 = 0.97$.

$$pdf(n) = 0.948(e)^{-2.5987 A_p} \tag{2-19}$$

The mean $A_{50a} = 9.21$ mm^2, and $A_{50n} = 0.0413$ mm^2.

Table 2-4 Micro-structural indices of CPP specimens by tomographic analysis

CPP Core	ϕ_t (%)			ϕ_e (%)	$(PSD)_{pore}$ [2] (μm)		SSA [2] (m^2/m^3)			$(L_e/L)_w$
	Meas	Cal.	RDP[3]		d_{50a}	d_{50n}	$(SSA)_s$	$(SSA)_{pt}$	$(SSA)_{pe}$	
N1-4 [1]	17.23	9.24	46.37	3.85	4012	370	1436	14105	15911	5.12
LC1-4	10.20	10.05	1.51	4.26	2870	364	1537	13529	15261	3.42
LC1-6	10.98	10.91	0.67	4.11	3955	337	1265	10256	11569	3.78
LC1-5	12.02	11.40	2.66	4.56	2943	337	1659	12142	13696	4.12
LC2-8	12.63	12.58	0.42	5.57	2987	370	1979	13689	15442	4.38
N2-10[1]	17.88	13.52	24.4	6.26	3987	364	2134	13650	15397	5.89
LC2-2	14.40	14.36	0.3	8.15	3014	364	1673	9946	11219	4.26
LC2-9	15.11	14.81	2.01	6.73	3048	337	2331	13095	14772	4.83
C2-6	16.71	16.25	2.74	10.99	3069	364	2251	11218	12654	4.73
C2-1	17.50	16.93	3.26	10.88	3311	401	2219	10460	11798	4.62
C1-5	18.51	17.90	3.27	12.80	3391	364	2728	12010	13547	5.45
C2-5	19.23	19.20	0.14	13.07	3150	370	3149	13228	14921	4.88
C2-3	19.26	19.22	0.19	11.64	3429	370	2962	12418	14008	4.41
C2-12	20.55	19.85	3.39	12.75	3477	364	3489	13490	15217	4.27
C2-11	20.94	20.76	0.88	15.75	3300	401	3402	12846	14490	4.38
LC2-10	21.22	21.17	0.22	14.35	3597	364	3398	12615	14230	4.02
S2-4	22.97	22.89	0.36	17.00	3608	364	4035	13531	15263	3.57
S2-2	24.71	24.54	0.67	20.59	3542	370	4946	15069	16998	3.68
S1-4	25.63	25.61	0.09	22.04	3452	401	5326	15455	17433	3.52
S1-5	27.98	27.49	1.77	24.59	3158	401	6221	16011	18061	3.21
S1-8	29.57	29.52	0.16	27.23	3236	401	6982	16629	18758	2.89

[1]: specimens taken from north PER where CPP was allowed to clogged by experiment

[2]: results obtained with image resolution of 35 μm

[3]: relative difference percentage, $RDP = (|measured - calculated| / measured) \times 100\%$

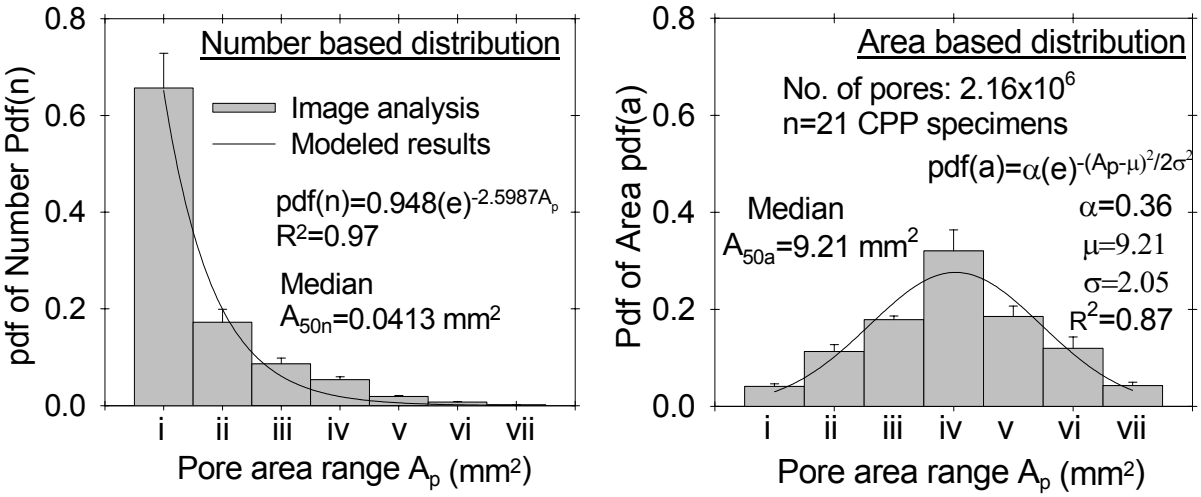

Figure 2-3 Probability density function (pdf) of the pore size area $(PSA)_{pore}$ based on the number and area distribution. Image resolution = 35 μm. The pore number distribution is modeled by an exponential model, $R^2 = 0.97$. In contrast, the pore area distribution is modeled by a gaussian distribution, $R^2 = 0.87$. A_p is the pore area ranges (mm2) as i: < 0.2857; ii: 0.2906~1.2575; iii: 1.2624~3.6035; iv: 3.6084~10.537; v: 10.5419~23.7158; vi: 23.7207~50.2164; vii: >50.2164.

From Figure 2-3, it's found that fine pores less than 286 μm count 66% of total number of pores, while they only contribute 4% to total area of pores. Fine pores' contribution to total area, especially those pores with size less than image resolution (35 μm), can be neglected.

It's also found that image resolution influenced the number analysis results, the higher the resolution, the smaller the d_{50n}, but did not significantly influence the d_{50a} which remained nearly constant as summarized in Table 2-5. The reason is that finer pores which are neglected in lower resolution images contribute significantly to the number of pores but little to the pore area.

Figure 2-4 illustrates the correlation between d_{50} and resolution R_r. The relationship could be modeled by the following expressions.

$$d_{50n} = 5.02(R_r)^{0.945} \tag{2-20}$$

$$d_{50a} = 3341(R_r)^{0.0057} \tag{2-21}$$

Table 2-5 Mean $(PSD)_{pore}$ of 21 CPP specimens under different image resolutions

Resolution mm^2/pixel (μm/pixel)	Number based median size				Area based median size			
	A_{50n} mm^2	σ of A_{50n}	d_{50n} μm	σ of d_{50n}	A_{50a} mm^2	σ of A_{50a}	d_{50a} μm	σ of d_{50a}
0.3111 (558)	3.526	0.65	2119	195	9.4212	0.63	3464	116
0.1383 (372)	2.351	0.50	1730	183	9.4012	0.62	3461	115
0.0778 (279)	0.890	0.16	1065	93	9.3832	0.60	3457	110
0.0346 (186)	0.555	0.20	841	152	9.3209	0.55	3446	102
0.0194 (140)	0.266	0.20	582	215	9.2380	0.55	3430	102
0.0086 (92)	0.111	0.08	376	142	9.2153	0.57	3426	105
0.0049 (69)	0.041	0.02	229	61	9.2050	0.57	3424	107
0.0022 (46)	0.028	0.01	190	36	9.1863	0.57	3421	106
0.0012 (35)	0.014	0.00	134	17	9.1487	0.53	3414	100

A_{50n}, A_{50a}: median pore area based on the number distribution and area distributions of all pores, respectively;

d_{50n}, d_{50a}: equivalent median pore diameter based on the number distribution and area distribution of all pores;

σ: standard deviation, based on image analysis for 21 CPP specimens.

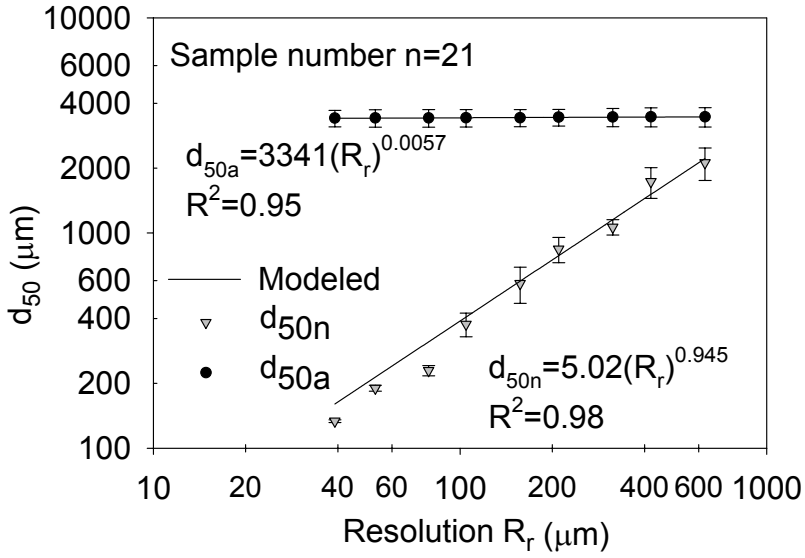

Figure 2-4 Power law model description of the relationship between d_{50} and image resolution (R_r) Range bars represent standard deviation of replicate image analyses for d_{50a} (μm) and d_{50n} (μm) for a given resolution, R_r. The d_{50n} and d_{50a} are the median pore diameter based on number and area distribution of all pores, respectively.

The R^2 = 0.98 and 0.95, respectively. In these equations d_{50} and R_r are in μm. With a very small power of 0.0013 in equation (2-21), it was found that d_{50a} is almost independent on the image resolution, as Figure 2-4 illustrates. The resolution-independent property of $d_{50a,}$ as index for the $(PSD)_{pore}$, makes the XRT analysis an effective tool for pore characteristics analysis for CPP and other similar porous media, and these pore characteristics are very desirable to predict the infiltration, filtration, evaporation and absorption performance of the porous media.

2.5.3 SSA and Correlation with ϕ_t and Image Resolution R_r

SSA results utilizing XRT analysis are shown in Table 2-4 (based on image resolution of 35 μm). Results indicate that depending on the pore size distribution, $(SSA)_s$ fall into the range of 1,00 to 7,000 m^2/m^3; and $(SSA)_{pt}$ are between 10,000 to 17,000 m^2/m^3, with a mean, μ, of 13,000 m^2/m^3 and standard deviation, σ, of 1,800. The $(SSA)_{pe}$ fall into the range of 12,000 to 19,000 m^2/m^3 with μ=15,000 m^2/m^3 and σ = 2,100.

Comparing the results of $(SSA)_{pt}$ to $(SSA)_{pe}$ summarized in Table 2-4, results indicate that $(SSA)_{pe}$ is slightly higher than $(SSA)_{pt.}$ Ratio of $(SSA)_{pe}$ to $(SSA)_{pt}$ falls into a range of 1.02 to 1.37, with a mean of 1.128 and standard deviation of 0.072.

$$(SSA)_{pe} = 1.128(SSA)_{pt} \tag{2-22}$$

This expression can be utilized to estimate $(SSA)_{pe}$ based on $(SSA)_{pt}$.

From Table 2-4, results also indicate that the higher the ϕ_t, the higher the $(SSA)_s$, because the higher porosity results in more pore-solid interface within a CPP core. Another consideration for SSA based on image analysis is the influence of image resolution. As previously indicated image resolution influences the analysis results of pore area distribution and therefore contributes to SSA. It was found that the higher the resolution, the smaller the d_{50n}, and the higher the $(SSA)_s$. These results occur because many fine pores are taken into account in higher resolution images and these fine pores contribute much to both the d_{50n} and SSA. For example, all pores with cross sectional area larger than 0.0012 mm^2 are taken into account when image resolution is 35 μm, while only pores with cross sectional area bigger than 0.0049 mm^2 are taken into account when image resolution is 70 μm.

Since both the total porosity ϕ_t and pore size distribution $(PSD)_{pore}$ influence SSA, it is expected that there should be a correlation between these pore characteristics. Figure 2-5 illustrates the relationship between $(SSA)_s$, total porosity ϕ_t and image resolution R_r, which can be summarized in the following general form.

$$(SSA)_s = f(R_r)(\phi_t)^{1.76} \tag{2-23}$$

In this expression ϕ_t is in percentage, and R_r is image resolution in μm, and relationship between parameter $f(R_r)$ and R_r is summarized in the following expression.

$$f(R_r) = 228.38(R_r)^{-0.716} \tag{2-24}$$

Substituting this equation to equation (2-23), yields the following expression.

$$(SSA)_s = \frac{228.38(\phi_t)^{1.76}}{(R_r)^{0.716}} \tag{2-25}$$

This equation can be used to estimate SSA under different resolution when total porosity is known. Substituting equation (2-20) to (2-25) yields the following expression.

$$(SSA)_s = 775.49(\phi_t)^{1.76}(d_{50n})^{-0.7577} \tag{2-26}$$

In this equation ϕ_t is a percentage, and d_{50n} in μm. This equation indicates how total porosity and pore size distribution influence $(SSA)_s$. As long as $(SSA)_s$ is known using (2-26), $(SSA)_{pt}$ can be calculated by (2-13), while $(SSA)_{pe}$ can be approximately estimated as $1.128(SSA)_{pt}$.

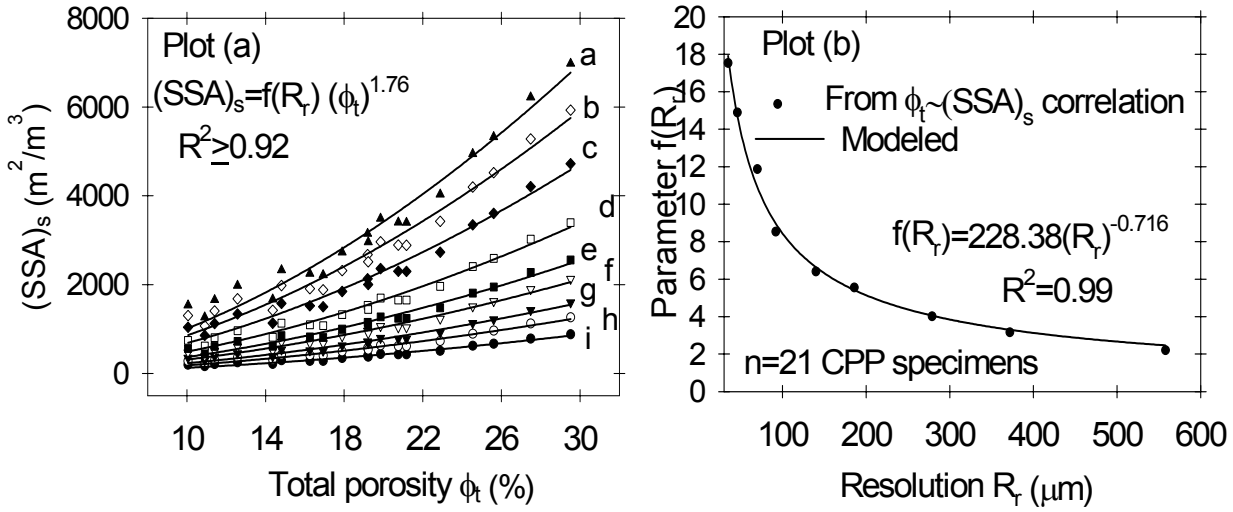

Figure 2-5 Plot (a) illustrates a power law relationship between total ϕ_t (%) and $(SSA)_s$ (m^{-1}). a~i represent the modeled different resolution as table 2-5 shows. f(Rr) and R^2 under different resolution are as follows:
a: R_r=35 μm, $f(R_r)$ = 17.53, R^2 = 0.93; b: R_r = 46 μm, $f(R_r)$ = 14.88, R^2 = 0.94;
c: R_r=70 μm, $f(R_r)$ = 11.86, R^2 = 0.93; d: R_r = 92 μm, $f(R_r)$ = 8.52.77, R^2 = 0.94;
e: R_r=140 μm, $f(R_r)$ = 6.40, R^2 = 0.95; f: R_r = 185 μm, $f(R_r)$ = 5.55, R^2 = 0.96;
g: R_r=279 μm, $f(R_r)$ = 4.00, R^2 = 0.96; h: R_r = 372 μm, $f(R_r)$ = 3.16, R^2 = 0.96;
i: R_r=558 μm, $f(R_r)$ = 2.20, R^2 = 0.97.

Compared to the measured value by EGME, the calculated $(SSA)_s$ are lower. The main reason is that the very fine pores that contribute significantly to the SSA are eliminated in image

analysis because of the limitation of image resolution. The main purpose of measuring SSA in this study, however, was to evaluate hydraulic characteristics of CPP. From this point of view, the very fine pore contribution can be neglected. Pores on the order of 10 μm or less require a pressure head that is not available even under ponded conditions on the CPP surface (the maximum depth of ponding is 6 mm). The nanometer-sized pores are unlikely to influence flow on a macroscopic scale since much larger pores are present. Use of $(SSA)_s$ yield hydraulic conductivity results that underestimate measured values (Schaap and Lebron 2001). According to Berryman and Blair's finding (1987), pores finer than 1/100 of the median size did not significantly influence flow. For CPP, average d_{50a} = 3425 μm as analyzed above, pores with diameter less than 3425/100 = 34.25 μm can be reasonably neglected in terms of hydraulic property estimation. In order to take into account all those pores larger than 34.25 μm, based on the equivalent area, the resolution required during tomography should be calculated as the following.

$$R_r^2 = \frac{\pi[(d_{50a})/100]^2}{4} \tag{2-27}$$

When d_{50a} = 3425 μm, based on the above expression, Rr = 30 μm , however, resolution used in this study is Rr_1= 35 μm, resulting in neglecting all pores with equivalent diameter less than 38.7 μm. For hydraulic conductivity estimation, (SSA) should be analyzed under Rr_2= 30 μm.

When Rr_1 = 35 μm, (SSA) were obtained as Table 2-4 illustrated. Using (2-25), and noticing that ϕ_t is independent on resolution, $(SSA)_s$ under Rr_2 = 30 μm can be estimated as following.

$$(SSA)_{s-30} = (\frac{R_{r1}}{R_{r2}})^{0.7178}.(SSA)_{s-35} \tag{2-28}$$

In this expression, $(SSA)_{s\text{-}35}$ and $(SSA)_{s\text{-}30}$ represent solid based (SSA) under R_r = 35 and 30,

respectively. $(SSA)_{pt\text{-}30}$ and $(SSA)_{pe\text{-}30}$ can be estimated by (2-15) and (2-22), respectively. Table 2-6 illustrates (SSA) under Rr = 35 and 30, respectively. This Table shows that, for the purpose of hydraulic conductivity prediction, the $(SSA)_s$ in the range of 1.4~7.8 $\times 10^3$ m^2/m^3, $(SSA)_{pt}$ of 1.1 ~1.9×10^4 m^2/m^3, and $(SSA)_{pe}$ in the range of 1.3 to 2.1 $\times 10^4$ m^2/m^3 would be utilized for hydraulic prediction. However, it is necessary to note that these conclusions are drawn based on analysis results of the given 21 CPP specimens, and they may not applicable for other porous media with quite different pore size distribution and pore size shape.

2.5.4 Tortuosity (L_e/L)

Based on XRT analysis, CPP tortuosity ranges from 2.89 to 5.89. Compared to the commonly assumed value of 1.414 based on 2-D planes, these values based on 3-D analysis are much higher and much more reasonable agreement with the range for similar porous media (Saripalli et al. 2002; Zhang and Knackstedt 1995). Pdf of tortuosity follows a Gaussian distribution as shown in plot (a) of Figure 2-6, with R^2=0.93.

$$pdf(L_e/L) = 0.2955(e)^{-0.5\left\{\frac{(L_e/L)-4.26}{0.6515}\right\}^2} \tag{2-29}$$

Results also showed that tortuosity increases with the increase of total porosity (ϕ_t) when ϕ_t is less than 17.36%, while decreases when ϕ_t is higher than 17.36%, as plot (b) of Figure 2-6 shows. The relationship can be presented as a Gaussian model

$$(L_e/L) = 4.65(e)^{-0.5\left\{\frac{\phi_t-17.36}{11.09}\right\}^2} \tag{2-30}$$

with R^2=0.77, where ϕ_t is in percentage. Error ranges in plot (b) represent the standard deviation of (L_e/L) for a given (ϕ_t). The reason of a Gaussian relationship between L_e/L and ϕ_t is due to the fact that higher total porosity usually generate more and longer flow pathways which result in the increase of tortuosity, however, when ϕ_t is very high (higher than 17.36% here), most pathways

connect with each other, and pathway cross-section area becomes larger, which reduces tortuosity. These results agree well with those presented by Zhang and Knackstedt (1995).

Resolution has little influence on the measurements of tortuosity. The main reason is that the lengths of flow pathways are weighted by their cross-sectional area, so that pathways formed by coarse pores contribute most while pathways formed by fine pores contribute little to tortuosity. Similar to ϕ_t, ϕ_e and d_{50a}, the resolution-independence property of tortuosity make XRT a very reliable tool for pore characteristics determination.

Table 2-6 (SSA) (m^2/m^3) results under different image resolutions in tomography analysis

CPP Core	ϕ_t	(SSA) with R_{r1} = 35 μm [1]			(SSA) with R_{r2} = 30 μm [2]		
		$(SSA)_s$	$(SSA)_{pt}$	$(SSA)_{pe}$	$(SSA)_s$	$(SSA)_{pt}$	$(SSA)_{pe}$
LC1-4	10.2	1537	13529	15261	1716	15112	17046
LC1-6	10.98	1265	10256	11569	1413	11456	12922
LC1-5	12.02	1659	12142	13696	1853	13562	15298
LC2-8	12.63	1979	13689	15442	2210	15291	17248
LC2-2	14.4	1673	9946	11219	1869	11109	12531
LC2-9	15.11	2331	13095	14772	2604	14628	16500
C2-6	16.71	2251	11218	12654	2514	12531	14134
C2-1	17.5	2219	10460	11798	2478	11683	13179
C1-5	18.51	2728	12010	13547	3047	13415	15132
C2-5	19.23	3149	13228	14921	3518	14775	16667
C2-3	19.26	2962	12418	14008	3309	13871	15647
C2-12	20.55	3489	13490	15217	3897	15068	16997
C2-11	20.94	3402	12846	14490	3800	14349	16185
LC2-10	21.22	3398	12615	14230	3795	14091	15894
S2-4	22.97	4035	13531	15263	4507	15114	17048
S2-2	24.71	4946	15069	16998	5524	16832	18987
S1-4	25.63	5326	15455	17433	5949	17263	19473
S1-5	27.98	6221	16011	18061	6948	17885	20174
S1-8	29.57	6982	16629	18758	7799	18575	20952

[1]: obtained by tomography analysis;

[2]: $(SSA)_s$ estimated by equation (2-28):

$$(SSA)_{s-30} = (\frac{R_{r1}}{R_{r2}})^{0.7178}.(SSA)_{s-35} \quad (2\text{-}28)$$

$(SSA)_{pt\text{-}30}$ and $(SSA)_{pe\text{-}30}$ were calculated using (2-15):

$$(SSA)_s = \frac{S_{pt}}{V_s} = \frac{\phi_t}{1-\phi_t}(SSA)_{pt} \quad (2\text{-}15)$$

and (2-22):

$$(SSA)_{pe} = 1.128(SSA)_{pt} \quad (2\text{-}22)$$

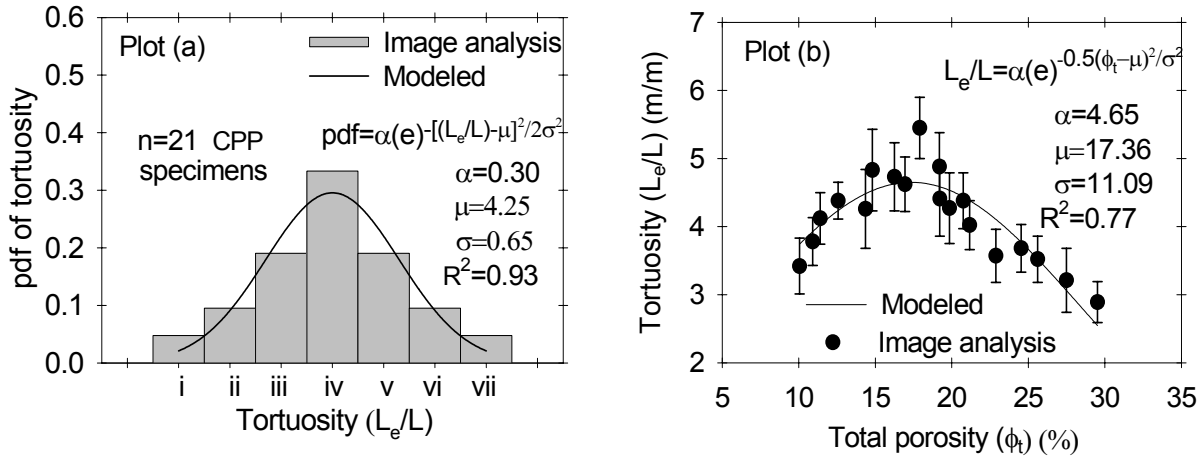

Figure 2-6 Plot (a) illustrates the probability density function of CPP specimen tortuosity (Le/L). Plot (b) illustrates the relationship between Le/L and ϕ_t with a Gaussian model. Tortuosity ranges, i: 2.5~3.0; ii: 3.0~3.5; iii: 3.5~4.0; iv: 4.0~4.5; v: 4.5~5.0; vi: 5.0~5.5; vii: 5.5~6.0.

2.6 CONCLUSIONS

21 cementitious permeable pavement (CPP) specimens taken from a prototype partial exfiltration reactor loaded by rainfall or rainfall-runoff were utilized to present a methodology and pore characteristics results for this low impact development (LID) material that functions to provide passive quantity and quality control of urban runoff. Based on the methodology developed in this study to determine pore characteristics using XRT, total porosity ϕ_t, effective porosity ϕ_e, pore size distribution $(PSD)_{pore}$, specific surface area of $(SSA)_s$, $(SSA)_{pt}$, and$(SSA)_{pe}$, and tortuosity (L_e/L) of CPP specimens were evaluated. Conventional gravimetrics-geometrics were also utilized to determine ϕ_t, specific gravity S_g and $(SSA)_s$.

Results indicate that XRT analysis of ϕ_t, ϕ_e, d_{50a} (or A_{50a}), and (L_e/L) were nearly independent on the image resolution R_r, making XRT a useful tool to predict hydraulic and filtration constitutive properties of CPP. In the presence of coarse pores, fine pores do not significantly contribute to these hydraulic and filtration behavior of CPP. In contrast, (SSA), d_{50n} (or A_{50n}) were dependent on R_r, because fine pores significantly contribute to these results.

Relationships between (SSA), ϕ_t, d_{50n} and R_r were established.

ϕ_t results obtained by XRT analysis agree well with those of gravimetric analyses. Results indicated that across a range of total porosity from 10% to 30% the corresponding effective porosity ranged from 4% to 27%. A power law of ϕ_t–ϕ_e relationship was utilized to establish a calibration between the effective and total porosity, allowing effective porosity to be determined from simpler and more economical measurements from geometrics and gravimetrics. Pore area distributions followed a Gaussian model while pore number distributions followed an exponential decay model. The mean number-based d_{50n} was 229 μm based on image resolution of 35 μm, and the area-based d_{50a} was 3425 μm which is independent on image resolution. According to XRT analysis with a image resolution of 35 μm, $(SSA)_{pt}$ ranged from 10,000 to 17,000 m^2/m^3, and $(SSA)_{pe}$ ranged from 12,000 to 19,000, while 1/100 of the median pore size (d_{50a}) requires a resolution of 30 μm by which most of pores that contribute to fluid flow could be taken into account, and $(SSA)_{pe}$ ranged from 13,000 to 21,000 m^2/m^3. These (SSA) results are applicable for hydraulic properties and filtration performance prediction. Correlation between $(SSA)_s$-d_{50n}-ϕ_t was modeled with a power law model illustrating that (SSA) is determined by $(PSD)_{pore}$ and total porosity. Correlations between $(SSA)_s$, $(SSA)_{pe}$ and $(SSA)_{pt}$ were presented, making it possible to estimate $(SSA)_{pe}$ from $(SSA)_s$ or $(SSA)_{pt}$. Weighted tortuosity (L_e/L) ranged from 2.89 to 5.91, depending on ϕ_t. Both the pdf of (L_e/L) and the (L_e/L)-ϕ_t relationship followed a Gaussian distribution.

These results and relationships provide an essential foundation to predict CPP's hydraulic, hydrologic, filtration, reactive and load-deformation characteristics as a LID material. The XRT methodology also allows pore characteristics of ϕ_e, d_{50}, $(SSA)_{pe}$, and (L_e/L) to be

obtained or calculated from a calibrated relationship, that would otherwise be very difficult to determine from conventional methods.

2.7 NOTATION

A = total cross section area in all images of a specimen (L^2);

A_{50a} = area of the median pore based on area distribution (L^2);

A_{50n} = area of the median pore based on number distribution (L^2);

A_e = area of effective pores (L^2);

A_s = area of solids (L^2);

A_v = area of total pores (L^2);

$C_b(j)$, $C_e(j)$ = beginning and end column of a pore in the *j*th row in image bitmap;

L = length of a specimen in z direction (L);

L_e = weighted length of all fluid pathways formed by effective pores (L);

M = the number of total slices of a specimen;

M_e = EGME mass absorbed by sample (M);

M_s = mass of sample (M);

N_r = the number of total rows occupied by a pore in a image;

P_1, P_2 = recorded pressure of the inert gas during test (P);

P_e, P_t = perimeter of effective pores and total pores of a specimen (L);

R_r = resolution (L);

S_g = specific gravity

SSA = specific surface area (L^2/L^3);

V_c, V_r = coefficient of the Multi-Pycnometer (L^3);

V_b =bulk volume of specimen (L^3);

V_s =solid volume (L^3);

V_p = sample volume (L^3);

W = weight of sample in specific gravity test (M);

X_c, Y_c = central coordinator

d_{50a}, d_{50n} = median pore diameter based on area and number distribution , respectively (L);

l = spacing between two image slices (L);

l_e = length of two connected pores between two adjacent slices (L);

$\Omega(z,k)$ = boundary configuration of the *k*th pore in slice z

ϕ_e, ϕ_t = effective porosity and total porosity (L^3/L^3)

μ = mean

σ = standard deviation

2.8 REFERENCES

Asaeda, T., and Ca, V.T. (2000). "Characteristics of permeable pavement during hot summer weather and impacton the thermal environment." *Can. Build. & Env.,* 35, 363-375.

Al-Omari, L.T., Masad, E., Cooley, A. and Harman, T. (2002). "Proposed methodology for predicting HMA Permeability." *Journal of the Association of the Asphalt Paving Technologists*, 71, 30-58.

Andersen, C.T., Foster, I.D.L., and Pratt, C.J. (1999). "The role of surfaces (permeable pavement) in regulating drainage and evaporation: development of a laboratory simulation experiment." *Hydrological Processes*, 13, 597-609.

ASTM C 457-90 (1990). "Standard test method for microscopic determination of parameters of the air-void system in hardened concrete." *Annual Book of Standard*, 1990.

ASTM D 421-85 (1999). "Standard practice for dry preparation of soil samples for particle-size analysis and determination of soil constants." *Annual Book of Standard*, 4(8), 8-9.

Bäckström, M. (2000). "Ground temperature in porous pavement during freezing and thawing." *Journal of Transportation Engineering, ASCE*, 375-381.

Bäckström, M. and Bergström, A. (2000). "Draining function of porous asphalt during snowmelt and temporary freezing." *Can. J. Civil. Eng.*, 27, 594-598.

Berryman, J.G., and Blair, S.C. (1986). "Use of digital image analysis to estimate fluid permeability of porous materials: application of two-point correlation function." *J. Appl. Phys*., 60(6), 1930-1938.

Berryman, J.G., and Blair, S.C. (1987). "Kozeny-Carman relations and image processing methods for estimating Darcy's constant." *J. Appl. Phys*., 62 (6), 2221-2228.

Bérengier, M.C., Stinson M.R., Daigle, G.A., and Hamet, J.F. (1997). "Porous road pavements: Acoustical characterization and propagation effects." *Journal of Acoustic Society of America*, 101(1), 155-162.

Brattebo, B.O., and Booth, D.B. (2003). "Long-term Stormwater quantity and quality performance of permeable pavement systems." *Water Research*, 37, 4369-4376.

Braz, D., Damotta, L.G. and Lopes, R.T. (1999). "Computed tomography in the fatigue test analysis of an asphalt mixture." *Applied Radiation and Isotopes*, 50, 661-671.

Calgon Carbon Corporation, (1995). *F400 Specification Sheet*, Pittsburgh.

Carman, P.C. (1956). *Flow of Gases Through Porous Media*, New York, Academic Press Inc.

Cooley, L.A. and Brown, E.R. (2000). "Selection and evaluation of a field permeability device for asphalt pavements." *TRB, National Research Council*, no.1723, Washington, D.C.

Dardis O. and McCloskey, J. (1998). "Permeability porosity relationships from numerical simulations of fluid flow." *Geophysical research letters*, 25 (9), 1471-1474.

Dullien, F. (1992). *Porous Media: Fluid Transport and Pore Structure*, Academic, NY, 1992.

Eriksen and Wegan (1993). "Optical Methods for the Evaluation of Asphalt Concrete and Polymer Modified Binders." *Danish Road Institute*.

Fach, S., Geiger, W.F. and Dierkes, C. (2002). "Development of an assessment procedure for porous pavements." *9th Conference on Urban Drainage 2002 in Portland.*

Field, R., Masters, H., and Singer, M. (1982). "Porous pavement: research; development; and demonstration." *Journal of Transportation Engineering*, *ASCE*, 108, 244-258

Flind L.E., and Selker, J.S. (2003). "Use of porosity to estimate hydraulic properties of volcanic tuffs." *Advances in Water Resources*, 26, 561-571.

Ghafoori, N., and Duta, S. (1995). "Laboratory investigation of compacted no-fines concrete for paving materials." *Journal of Materials in Civil Engineering*, *ASCE*, 7(3), 183-191.

Giménez, D., Allmaras, R.R., Huggins, D.R. and Nater, E.A. (1997). "Prediction of the Saturated Hydraulic Conductivity-Porosity Dependence Using Fractals." *So. Sc. Soc. Am.*, 5, 1285-1292.

Guo, J.F., Cai, Y.L., and Wang, Y.P. (1995). "Morphology-based interpolation for 3D medical image reconstruction." *Comput. Med. Image. Grap*. 19(3), 267-279.

Hall, K.D., and NgHooi, G. (2001). "Development of void pathway test for investigating void interconnectivity in compacted hot-mix asphalt concrete." *TRR*, no.1767, 40-47.

Hall,C.C. (2000). "Non-destructive tomographic energy-dispersive diffraction imaging of the interior of bulk concrete." *Cement Concrete Res*. 30(3), 491-495.

Harvey, J., Mills, T., Scheffy, C., Sousa, J., and Monismish, C.L. (1994). "An evaluation of several techniques for measuring air-void content in asphalt concrete specimens." *Journal of testing and Evaluation*, ASTM, 430.

Hilpert, M., and Miller, C.T. (2001). "Pore-morphology-based simulation of drainage in totally wetting porous media." *Advanced in Water Resources,* 24, 243-255.

Hot Mix Asphalt Technology-September/October 2003, 26-40

Huang, B., Mohammad, L., Raghavendra, A., and Abadie, C. (1999). "Fundamentals of permeability in Asphalt Mixtures." *Journal of the Association of Asphalt Paving Technologists*.

Jackson, T.J. and Ragan, M. (1974). "Hydrology of porous pavement parking lots." *Journal of the Hydraulics Division*, 1739-1752.

Jain, A.K., and Dubuisson, M.P. (1992). "Segmentation of X-ray c-scan images of fiber reinforced composite materials." *Pattern Recognition*, 25, 257-270.

Jin, X., Yokoi, S. and Toriwaki, T. (1992). "A shape interpolation method for three-dimensional digital images." *Systems and Computers in Japan*, 23 (2), 51-63.

Kanitpong, K., Benson, C.H., and Bahia, H.U. (2001). "Hydraulic conductivity (Permeability) of laboratory compacted asphalt mixtures." *2001 annual meeting of the TRB*. 2001

Kanitpong, K., Bahia,H.U., Benson, C.H., and Wang, X. (2003). "Measuring and predicting hydraulic conductivity (permeability) of compacted asphalt mixtures in the laboratory." *82nd Annual Meeting of TRB CD-ROM*.

Kobayashi, T., Kagata, M., Kodama, T., and Ito, M. (2002). "Development of the environment-friendly hybrid permeable concrete." *Transactions of the Japan Concrete Institute*, 23, 65-76.

Krishnan, J.M., and Rao, C.L. (2001). "Permeability and bleeding of asphalt concrete using mixture theory." *International Journal of Engineering Science*, 39, 611-627

Kuennen T. (2003). "A new era for permeable pavement." *Road Science-Better Road*, 28-32.

Landis, E.N (1999). "X-ray microtomography for fracture studies in cement-base materials, in proceedings of SPIE." *The International Society for Optical Engineering*, 3772, 105-133.

Lebron, I., Schaap, M.G., and Suarez, D.L. (1999). "Saturated hydraulic conductivity prediction from microscopic pre geometry measurements and neural network analysis." *Water Resources Research*, 35(10), 3149-3158.

Leu J.G. (1992). "Image contrast enhancement based on the intensities of edge pixels." *Graphical Models And Image Processing*, 54(6), 497-506.

Lin, W.C., Liang, C.C., and Chen, C.T. (1988). "Dynamic Elastic Interpolation for 3D medical image reconstruction from serial cross section." *IEEE Tran. on Med. Imag.*, 7(3), 225-232.

Lindquist W.B., Lee, S.M., Coker, D., Jones, K.W., and Spanne, P. (1996). "Medial axis analysis of void structure in three-dimensional tomographic images of porous media." *Journal of Geophysical Research*, 101 (B4), 8297-8310

Li, Y.B., Buchberger, S.G., and Sansalone, J. (1999). "Variably Saturated Flow in Storm –Water Partial Exfiltration Trench." *Journal of Environmental Engineering*, *ASCE*, 556-565

Masad, E., Muhunthan, N., Shashidhar, N., and Harman, T. (1998). "Internal structure characterization of asphalt concrete using image analysis." *Journal of Computation in Civil Engineering*, 13, 88-95

Masad, E., Birgisson, B., Al-Omari, A., and Cooley, A. (2002). "Analysis of Permeability and Fluid Flow in Asphalt Mixes." *The 82th Annual TRB Meeting CD-ROM*.

Maupin, G.W. Jr. (2000). "Asphalt permeability testing in Virginia." *Journal of the TRB*, 1723.

McDowell-Boyer, L.M., Hunt, J.R., and Sitar, N. (1986). "Particle transport through porous media." *Water Resources. Res*., 22(13), 1901-1921.

Mcworter, D.B., and Sunada, D.K. (1977). *Groundwater Hydrology and Hydraulics*, Water Resources Publications, Ft. Collins, CO.

Meegoda N.J., King, I.P. and Arulanandan, K. (1989). "An expression for the permeability of an isotropic granular media." *International Journal for Numerical and Analytical Methods in Geomechanics*, 13, 579-598.

Metcalf & Eddy (2003). *Wasterwater Engineering Treatment and Reuse*, 4th Edition, McGraw-Hill pulishing Ltd.

Mohammad L.N., Herath, A. and Huang, B. (2003). "Evaluation of permeability of superpave asphalt mixtures." *TRB 2003 Annual Meeting CD-ROM*.

Nakashima, Y. and Watanabe, Y. (2002). "Estimate of transport properties of porous media by microfocus x-ray computed tomography and random walk simulation." *Water Resources Research*, 38 (12), 8-1-8-12.

Niemczynowicz, J. (1989). "Swedish way to storm water enhancement by source control." *Urban Stormwater Enhancement-Source Control, Retrofitting and Combined Sewer Technology*, *Urban Water Resource Research Council*, American Society of Engineers, New York, 156-158.

Oke T. (1982). "The energetic basis of urban heat island." *Quar. J. Roy. Met. Soc*. 108, 1-24

Pleau, R., Pigeon, M., and Laurencot, J.L. (2001). "Some findings on the usefulness of image analysis for determining the characteristics of the air-void system on hardened concrete." *Cement and Concrete Composites*, 23, 237-246.

Pollefeys, M., Koch, R., Vergauwen, M., and Gool, L.V. (2000). "Automated reconstruction of 3D scenes from sequences of images." *ISRPS J. of Photo-Gra. Rem. Sen.,* 251-267.

Ranieri V. (2002). "Runoff control in porous pavement." *TRB* 1789, Paper no. 02-3476, 46-55

Raya, S.P., and Udupa, J.K. (1990). "Shape-based interpolation of multi-dimensional objectives." *IEEE Transactions on Medical Iimaging*, 9 (1) , 32-42.

Robertes, L. R., Scali, M. J., Grace, W. R. (1984). "Factors affecting image analysis for measurement of air content in harden concrete." *International Conference on Cement Microscopy*, 402-419.

Sansalone, J.J., Koran, J.M., Smithson, J.A., and Buchberger, S.G. (1998). "Physical characteristics of urban roadway solids transported during rain events." *J. Environ. Eng*., 124(5), 427-440.

Saripalli, K.P., Serne, R.J., Meyer, P.D., and Mcgrail, B.P. (2002). "Prediction of diffusion coefficients in porous media using tortuosity factors based on interfacial areas." *Ground Water*, 40, 346-352.

Scheidegger, A. (1974). *The Physics of Flow Through Porous Media*, University of Toronto Press, Toronto.

Schaap, M.G., and Lebron, I. (2001). "Using microscope observations of thin sections to estimate soil permeability with the Kozeny-Carman equation." *J. of Hydro.*, 251, 186-201.

Shashidhar, N. (1999). "X-ray tomography of asphalt concrete." *Journal of TRB, no. 1681, TRB*, National Research Council, Washington, D.C., 186-192.

Sherard ,J.L. and Dunnigan, L.P. (1989). "Critical filters for impervious soils." *Journal of Geotechnical Engineering*, ASCE, 115(7), 927-947

Teng, Z. and Sansalone, J. (2004). "In-Situ Partial Exfiltration of Rainfall-Runoff-II: Particle Separation." *Journal of Environmental Engineering*, *ASCE*.

United States EPA (1999). "Storm water technology fact sheet porous pavement." *EPA 832-F-99-023*.

Watanabe, S. (1995). "Study on storm water control by permeable pavement and infiltration pipes." *Water Science Technology*, 32(1) 25-32.

Wang, L.B., Frost, J.D., and Shashidhar, N. (2001). "Microstructure Study of Westrack Mixes from X- Ray Tomography Images." *TRR, no. 1767*, 85-94

Wang L.B. and Frost J.D.(2003). "Quantification of Aggregate Specific Surface Area Using X-ray Tomography Imaging." ASCE Geotechnical Special Publication, Editor, Erol Tutumluer, Yacoub Najjar, and Eyad Masad, GSP No.123.

Wang, L.B. Frost, J.D., Voyiadjis, G.Z., Harman, T.P.(2003). "Quantification of damage parameters using X-ray tomography images." *Mechanics of Materials*, 35, 777-790.

Yue,Z.Q., bekking, W., and Morin, I. (1995). "Application of digital image processing to quantitative study of asphalt concrete microstructure." *Transportation Research Record* no.1492, TRB, Nation Research Council, Washington, D.C., 53-60.

Zube, E. (1962). "Compaction wtudy of asphalt concrete pavements as related to the water permeability test." *Highway Research Board*, Bulletin 358.

CHAPTER 3 HYDRAULIC CHARACTERISTICS OF CPP USING XRT ANALYSIS

3.1 INTRODUCTION

With subjective urban growth, deleterious hydrologic, climate and environmental problems associated with urban land development have grown resulting in reduced underground water recharge and degraded water quality (Bäckström 2000; Field et al. 1982; Jackson et al. 1974; Kuennen 2003; Teng and Sansalone 2004). Research has shown that the degree of imperviousness in the built environment is significantly correlated to those impacts and problems due to the increased peak flow, volume and lag time of runoff (Bäckström 2000; Field et al. 1982; Jackson et al. 1974; Kuennen 2003). Permeable pavement is an available and effective approach to mitigate these problems through gravitational drainage, capillary movement, infiltration and filtration mechanisms (Isenring et al. 1995; Imenez and Peren 1990; Fach 2002; Jackson and Ragan 1974; Teng and Sasalone 2004).

Hydraulic Conductivity is one of the most important indexes for porous media. There has been considerable research on hydraulic conductivity in porous media, such as soil and rock science (Carmen 1937; Ahuja et al. 1989; Paydar and Ringrose-Voase 2003; Rawls et al. 1993; Minasny and Mcbratney 2000; Regalado and Muňoz-Carpena 2004; Dixon et al. 1999; Meegoda et al. 1989; Giménez 1997; Flind and Selker 2003; Timlin, 1999), and in regular asphalt pavements (impermeable) (Al-Omari et al. 2002; Choubane et al. 1989; Cooley and Brown 2000; Hainin et al. 2003; Krishnan and Rao 2001; Mallick 2001; Masad et al. 2002; Maupin 2000; Mohammad et al. 2003; Xi and Bažant 1999; Zube 1962). Based on lab and field test, a simple relationship for predicting saturated hydraulic conductivity k_{sat} based on the Kozen-Carman

model was used widely in soil science (Ahuja et al. 1984) and pavement (Krishnan, 2000, Kanitpong et al.2001; Masad et al. 2003) expressed as the following form.

$$k_{sat} = B(\phi_t)^n \tag{3-1}$$

In this expression k_{sat} is saturated hydraulic conductivity in cm/s, B and n are constants obtained by experimental measurements, and ϕ_t is porosity. It is found that hydraulic conductivity is the only engineering property that can vary by more than ten orders of magnitude (Meegoda et al. 1989). For example, hydraulic conductivity for clay is in the range of 10^{-13} to 10^{-8} cm/s (Dixon et al. 1999), for conventional asphalt pavement, it is in the range of 8.5×10^{-7} to 10^{-4} cm/s depending on porosity from 4%-8%. (Kanitpong et al. 2003). According to laboratory and field tests, the typical value of hydraulic conductivity of regular hot mixture asphalt (HMA) pavements is in the magnitude of 10^{-5} cm/s (Huang et al. 1999; Masad et al. 2002; Mohammad et al. 2003). In regular pavements, it demands permeability as small as possible to prevent water from entering pavement systems, because infiltration of water into the pavement can affect the durability of pavements. However, very higher hydraulic conductivity is desirable for porous pavement since one of the main purposes of porous pavement is to control runoff and reduce perk flow during rainfall.

Some research on hydraulic conductivity also has been done for HMA porous pavements (Wada et al 1997, Isenring and Scazziga 1990, Pratt et al. 1995, Backsrom and Bergstrom 2000, Fwa et al. 1999). Most of their work was based on laboratory or field tests. Some assessment procedures for permeable pavement including hydraulic conductivity were also developed by field test (Fach et al. 2002; Jackson and Ragan 1974).

Although much research has been carried out for many kinds of porous media and many empirical models were developed based on simplified or idealized media particle shape, little

was done on CPP based on its special pore structure with high porosity, irregularly shaped pores and wide range of pore size distribution. Compared to other porous media, CPP has the special characteristics of high porosity and low hydraulic head loaded. It is very important to develop methodology to predict CPP hydraulic conductivity based on its specially pore characteristics and pore size distribution.

3.2 OBJECTIVES

This study has four main objectives related to the hydraulic characteristics of CPP. The first objective is to evaluate saturated hydraulic conductivity for CPP by constant-head experiments. The second objective is to compare some empirical models for hydraulic conductivity estimation and, based on these empirical models, to establish a modified model for CPP hydraulic conductivity prediction. The third objective is to evaluate pore space factors that influence hydraulic characteristics of CPP. The last objective is to develop k-ϕ_t and k-ϕ_e relationships for predicting hydraulic conductivity k when total porosity ϕ_e or ϕ_t is known.

3.3 BACKGROUND

Relationships between porosity and hydraulic properties have been identified by previous authors, and many empirical models were developed for hydraulic conductivity estimation for porous media (Flint and Selker 2003; Vuković et al. 1992). These relationships with hydraulic properties include dependence on particle or pore sizes for both mean values and the entire distribution of values. Those based on particle size are typically empirical or phenomenological, while the models based on pore sizes more often include assumptions regarding pore structure, shape, connectivity or tortuosity (Flint and Selker 2003). The real pore size distribution with irregular and non-uniform shape pores was seldom evaluated for hydraulic conductivity estimation. In most of these models, however, only total porosity and an “effective aggregate

diameter", usually d_{10}, were utilized to estimate hydraulic conductivity due to the difficulty and complexity of microstructure and pore characteristics examination. The widely used models are introduced below.

Beyer's model only consider the effective aggregate diameter d_e

$$k = C \cdot d_e^2 \tag{3-2a}$$

The empirical coefficient *C* depends on the coefficient of uniformity of aggregates.

A group of US authors recommended a so called USBR model for materials comprising medium-aggregate sands with the coefficient of uniformity <5,

$$k = 0.36 \cdot d_{20}^{0.3} \tag{3-2b}$$

In this expression d_{20} was used to represent d_e.

The typical form of Hazen model is as the following.

$$k = A \cdot C \cdot \tau \cdot d_e^2 \tag{3-3a}$$

In this expression A is constant and equals to 0.00116 if k in cm/s; $\tau = 0.7 + 0.03t$, and t is the water temperature in °C; d_e is the effective aggregate diameter, and is usually taken as d_{10}, and the empirical coefficient *C* was presented as a function of porosity.

$$C = 400 + 40 \times (\phi - 26)$$

So (3a) can be presented as

$$k = 0.0016 \cdot [400 + 40(\phi_t - 26)] \cdot (0.7 + 0.03t) \cdot d_{10}^2 \tag{3-3b}$$

In this expression, ϕ_t represents total porosity. This model was recommended for conditions under effective aggregate diameter d_e = 0.1~3 mm (Vuković et al. 1992).

Krüger model is recommended to apply at water temperature t = 0°C:

$$k = 240 \cdot \frac{\phi}{(1-\phi)^2} \cdot d_e^2 \tag{3-4}$$

The Krüger model empirical formula yields best results in the case of medium aggregate-size sands with the coefficient of uniformity >5 (Vuković et al. 1992).

Fair-Hatch (1933) presented a model for *k* estimation.

$$k = \frac{\phi^3}{\kappa_0^2 C_0 (1-\phi)^2} \cdot d_e^2 \cdot \frac{\gamma}{\mu} \tag{3-5}$$

In this expression C_0 is a filtration constant, 5 based on sieve opening and 6 based on size of separation, and κ_0 is a shape factor, for spherical particles, $\kappa_0 = 6.0$, and for crushed materials, $\kappa_0 = 8.5$ (Vuković et al. 1992); λ is the unit weight of water. $\lambda = 9790$ N/m^3 and μ is the dynamic viscosity (10^{-3} N.s/m^2) at 20 °C.

In Slichter formula (1898), d_e is required to fall into the range of 0.01~5 mm.

$$k = 10.0219 \cdot \phi^{3.287} \cdot d_e^2 \cdot \frac{\gamma}{\mu} \tag{3-6}$$

Terzaghi (1925) developed a formula to estimate *k* for coarse sand.

$$k = C \frac{\mu_{10}}{\mu_t} \left(\frac{\phi - 0.13}{\sqrt[3]{1-\phi}} \right)^2 \cdot d_{10}^2 \tag{3-7}$$

In this expression μ_t and μ_{10} are coefficient of absolute liquid viscosity at temperature t°C and 10°C, respectively, and *C* is the empirical coefficient depending on the nature of the aggregate surface.

Kozeny-Carman model (KCM) is one of the most accepted for *k* estimation based on filter pore characteristics.

$$k = \frac{\phi_t^{\,3}}{C_0 T^2 (1-\phi_t)^2 (SSA)_s^{\,2}} \cdot \frac{\gamma}{\mu} \tag{3-8}$$

In this expression *T* is tortuosity, (*SSA*)s is specific surface area based on solid volume (m^2/m^3). KCM is widely used to estimate hydraulic conductivity for soil, rocks, filters,

pavements and other porous media (Ahuja et al. 1997; Flint and selker 2003, Giménez et al. 1997; Zhuang et al. 2000; Seki and Miyazaki 2001; Berryman and Blair 1987; Nakashima and Yamaguchi 2004; Schaap and Lebron 2001; Paydar and Ringrose-Voase 2003; Regalado and Munoz-Carpena 2004; Dixon et al. 1999; Davies and Dollimore 1980; Al-Omari, 2002; Nakashima and Watanabe), but how to determine the parameters in this model is still a problem by conventional methods. The empirical coefficients predicted based on uniformly regular shaped particles (usually sphere) lead to unreasonable results of hydraulic conductivity (Flint and selker 2003). For example, effective porosity ϕ_e rather than total porosity (ϕ_t) has been demonstrated as a critical factor that determines the hydraulic characteristics of porous structures (Ahuja et al 1984; Regimand 1998; Huang and Mohammad 1999; Cooley et al. 2002; Al-Omari, et al. 2002; Flint and Selker 2003; Kostek et al. 1992). The second parameter, tortuosity (L_e/L), is difficult to measure directly, and usually assumed 1.414 based on equally-sized spherical granular material in the porous medium (Carman 1956), but some research showed that it was too lower (Flint and selker 2003). Another important parameter, specific surface area (SSA), is defined as SSA = 6/D for filters formed by uniformly spherical particles (Metcalf and Eddy 2003). However, in CPP, the pore volume interface to the solid structure surface is irregular. Flow characteristics are controlled by the pore space geometry rather than the solid matrix (Nakashima and Watanabe 2002; Zhang and Knackstedt 1995). Little research has been done due to the difficulty of pore connectivity determination. Another problem for SSA used in Kozeny-Carman model is that the (SSA) by EGME measurements are obviously too high and may yield hydraulic radii and permeability far too small (Schaap and Lebron 2001; Schlueter 1995) because fine pores contributing little to flow are significant for SSA. Dullien (1992) stated that

the KCM was more valid for porous media with broad particle size distribution than those with narrow gradation.

3.4 EXPERIMENT AND MATERIALS

Cored specimens were taken from CPP material constructed as the surface interface of a partial exfiltration reactor (PER). The PER is a linearly-extended in-situ rainfall-runoff unit operation and process. The primary components of the PER were introduced in Chapter 2. Totally 19 CPP specimens were utilized to measure hydraulic conductivity. Each core is about 96 mm in height and 70 mm in diameter. All cores were backwashed with tap water (pH = 7 and alkalinity ≈ 150 mg/L as $CaCO_3$) to remove any runoff particles from field CPP material or abraded particles generated in the coring process. The pore characteristics, including total porosity ϕ_t, effective porosity ϕ_e, pore size distribution $(PSD)_{pore}$, specific surface area of $(SSA)_s$, $(SSA)_{pt}$, and$(SSA)_{pe}$, and tortuosity (L_e/L) were evaluated using X-ray tomography. Details of the examination and results of pore characteristics are provided in Chapter 2.

An experimental setup was designed to measure the saturated hydraulic conductivity in constant head, as Figure 3-1 illustrated. CPP specimens were dip into DI water for 48 hours before test to make sure a saturated condition. Specimen's sidewall was packed by water-proof gray tape to avoid boundary effects. During test, DI water was pumped from the tank to specimen column by a peristaltic pump (Masterflux 7520-40). A series of constant head (5, 10, 20, 30, 40, 50, 60 mm over the surface of CPP specimen) were achieved by adjust the outlet level of overflow. Influent flow rates were controlled by regulating the speed of the peristaltic pump to make it keep overflowing during all test time, so that a certain constant head is maintained. After the system was steady, effluent volume was collected for 30 minutes, and then measured. At

least 5 samples were measured for each hydraulic head. Based on effluent volume, vol (mL), collected in 30 mins, flow rate, Q (mL/s), can be calculated as

$$Q = vol / t$$

In this expression t is the elapsed time in second.

Seepage velocity V = Q/(A). V is in cm/s and A is the cross section area of the CPP specimen. According to Darcy's Law,

$$V = k_{sat} \times \frac{\Delta h}{L} = k_{sat} \times i$$

From this expression, k_{sat} could be presented as

$$k_{sat} = V / i \tag{3-9}$$

In this expression Δh is head loss (cm), L is the length of specimen (cm), $i = \Delta h/L$ representing hydraulic gradient, and k_{sat} is saturated hydraulic conductivity in cm/s. Experimental measurements of hydraulic conductivity for the 19 specimens are listed in Table 3-1.

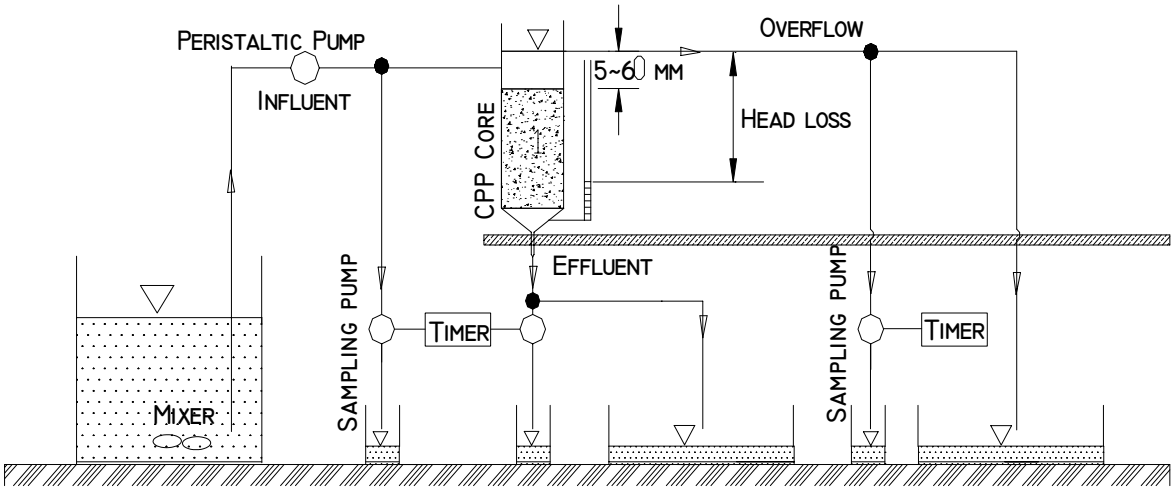

Figure 3-1 Experimental setup of constant head saturated hydraulic conductivity measurements for CPP. Different hydraulic head over the CPP surface could be achieved by adjusting the overflow outlet.

Table 3-1 Experimental results of hydraulic conductivity for 19 CPP specimens

CPP Specimen	ϕ_t (%)	ϕ_e (%)	k (10^{-3} cm/s)	σ (10^{-3})
LC1-4	10.05	4.26	5.68	2.05
LC1-6	10.91	4.11	7.82	1.86
LC1-5	11.40	4.56	5.04	2.03
LC2-8	12.58	5.57	4.45	1.77
LC2-2	14.36	8.15	11.95	1.91
LC2-9	14.81	6.73	5.02	2.21
C2-6	16.25	10.99	10.96	2.42
C2-1	16.93	10.88	12.85	2.56
C1-5	17.90	12.80	7.88	2.87
C2-5	19.20	13.07	9.02	2.48
C2-3	19.22	11.64	10.84	2.25
C2-12	19.85	12.75	11.96	2.65
C2-11	20.76	15.75	14.54	2.02
LC2-10	21.17	14.35	16.87	1.85
S2-4	22.89	17.00	21.77	2.41
S2-2	24.54	20.59	20.66	2.23
S1-4	25.61	22.04	22.41	1.88
S1-5	27.49	24.59	28.76	3.51
S1-8	29.52	27.23	32.86	3.41

ϕ_t: total porosity;
ϕ_e: effective porosity;
k: hydraulic conductivity (10^{-3} cm/s);
s: standard deviation

3.5 METHODOLOGY

On a microscopic scale the steady-state flow of incompressible fluids in an incompressible porous medium is governed by the equation of continuity and the steady-state Navier-Stokes equation (Meegoda et al. 1989; Flint and Selker 2003; reference from a book). The steady-state Navier-Stokes equation can be expressed as follows.

$$\rho \mathbf{V} \cdot \nabla \mathbf{V} = -\nabla p + \mu \nabla^2 \mathbf{V} \tag{3-10}$$

Equation of continuity for fluid motion of an incompressible fluid can be presented as

$$\nabla \cdot V = 0 \tag{3-11}$$

In these expressions, p is the pressure; ρ and μ represent the mass density and dynamic Viscosity, and **V** is velocity vector. Owing to the mathematical difficulties in solving the above equations, the Darcy's Law for macroscopic flow is being widely used as (3-9) shows.

$$k = V / i$$

Hydraulic conductivity, k, can be derived based on Darcy-Weissbach equation (Vuković 1992). For the flow in tubes, the head loss is expressed as

$$\Delta h = \lambda \frac{l}{d} \frac{V_0^2}{2g} \tag{3-12}$$

In this expression λ is the friction coefficient (dimensionless quantity); d is the diameter of tube, Δh is head loss (m); l is the length of the porous media along the flow direction, and V_0 is the fluid velocity in the tube.

Under the condition of laminar flow, the friction coefficient λ is a function of the Reynolds number

$$\lambda = 64 / R_e \tag{3-13}$$

and Reynolds number, R_e, can be presented as

$$R_e = (V_0 d) / \nu \tag{3-14}$$

In this expression ν is the Kinematic coefficient of viscosity (m^2/s).

Substituting (3-13) and (3-14) to (3-12), yields

$$\Delta h = \frac{32 \nu l V_0}{g d^2} \tag{3-15}$$

For porous media,

$$V_0 = V / \phi \tag{3-16}$$

In this expression V is seepage (Darcy) velocity. d is determined by both the porosity and pore size distribution of porous medium, which can be represented by "effective aggregate size" d_e.

letting $i = \Delta h / l$, and substituting (3-16) and (3-14) to (3-15), seepage velocity can be expressed as

$$V = C \cdot \varphi(\phi) \cdot d_e^2 \cdot \frac{g}{\nu} \cdot i = C \cdot \varphi(\phi) \cdot d_e^2 \cdot \frac{\gamma}{\mu} \cdot i \tag{3-17}$$

In this expression ϕ is porosity of porous medium; $\varphi(\phi)$ is the function determined by porosity in porous media; γ is unit weight of fluid; μ is the dynamic viscosity of fluid.

By comparing (3-17) to (3-9), it is easy to find that hydraulic conductivity

$$k = C \cdot \varphi(\phi) \cdot d_e^2 \cdot \frac{\gamma}{\mu} \tag{3-18}$$

From this expression, it is easy to see that hydraulic conductivity is determined by both the pore characteristics of porous medium and the properties of fluid. Most of empirical models mentioned above were derived from (3-18) by assuming a simple function of $\varphi(\phi)$ and an effective aggregate size d_e.

From Hagen-Poiseuille law for viscous flow in uniform circular capillary, Kozeny-Carman model (KCM) could be derived.

$$V_0 = \frac{\gamma \cdot \Delta h}{2\mu \cdot l} R_w^2 \tag{3-19}$$

In this expression R_w is the hydraulic radius (m^{-1}), by definition,

$$R_w = \frac{V_p}{A_g} = \frac{\text{pore volume}}{\text{grain surface area}} \tag{3-20}$$

In this expression

$$V_p = \phi \cdot V_t \tag{3-21}$$

and

$$V_g = (1-\phi)\cdot V_t \tag{3-22}$$

In this expression, V_t is the bulk volume.

$(SSA)_s$, the ratio of pore-solid interface area to aggregate volume, defined as

$$(SSA)_s = \frac{A_g}{V_g} \tag{3-23}$$

Substituting (3-20) ~ (3-22) to (3-23), yields

$$(SSA)_s = \frac{A_g}{V_g} = \frac{A_g}{(1-\phi)\cdot V_t} = \frac{\phi\cdot A_g}{(1-\phi)\cdot V_p} = \frac{\phi}{1-\phi}\cdot\frac{1}{R_w}$$

From this expression, R_w could be expressed as

$$R_w = \frac{\phi}{1-\phi}\cdot\frac{1}{(SSA)_s} \tag{3-24}$$

Substituting (3-16), (3-24) into (3-19), yields

$$V = C\frac{\phi^3}{(1-\phi)^2(SSA)_s^2}\cdot\frac{\gamma}{\mu}\cdot i \tag{3-25}$$

This expression leads to the Carmen (1934) equation of hydraulic conductivity

$$k = \frac{\phi_t^{\,3}}{C_0(1-\phi_t)^2(SSA)_s^{\,2}}\cdot\frac{\gamma}{\mu} \tag{3-26}$$

In this expression ϕ_t is total porosity; C_0 is shape constant, C_0=2.0 ~ 3.0, dependent on particle shape, and $(SSA)_s$ is specific surface area (m^{-1}) based on solid volume.

Since equation (3-25) and (3-26) were derived by uniform circular capillary based on Hagen-Poiseuille law, recognizing the effect of irregular shape of pores and flow pathways, Kozeny (1927) added a tortuosity factor (L_e/L) to Carman's shape factor which resulted in the Kozeny-Carman model as

$$k = \frac{\phi_t^{\,3}}{C_0 (L_e / L)^2 (1-\phi_t)^2 (SSA)_s^{\,2}} \frac{\gamma}{\mu} \tag{3-27}$$

Here (L_e/L) represent the ratio of real length of flow pathway to the shortest length of a medium.

This model have been widely used for filters with uniformly-shaped particles, for porous media with irregularly-shaped solid-pore interfaces and wide range of pore size or particle size distribution, however, it is not applicable for CPP the following reasons.

(a) Effective porosity rather than total porosity determines the hydraulic characteristics;

(b) $(SSA)_s$, specific surface area based on solid volume, can not represent the pore space geometry effectively (Nakashima and Watanabe 2002), however, flow characteristics are controlled by the pore space geometry rather than the solid matrix (Nakashima and Watanabe 2002; Zhang and Knackstedt 1995).

(c) Tortuosity (L_e/L) in (27) only considered the flow length, but actually, it is the throats that limit the flow transport in each pathway (Kostek et al. 1992, Al-Omari, et al. 2002; Zhang and Knackstedt 1995). Not only the length, but also the cross-section area of each pathway needs to take into account (Al-Omari et al. 2002; Flint and selker 2003).

(d) Nanometer-sized pores are unlikely to affect flow on a microscopic scale as long as continuous micron-sized or larger pores are present (Schaap and Lebron 2001), but these nanometer-sized pores contribute a lot to (SSA). It is necessary to determine what scale of pores need to be neglected in (SSA) measurements.

Based on the above recognitions, $(SSA)_{pt}$ and $(SSA)_{pe}$, as defined in Chapter 2, were employed. Based on (2-15)

$$(SSA)_s = \frac{\phi_t}{1-\phi_t} (SSA)_{pt}$$

Equation (3-27) could be written as

$$k = \frac{\phi_t}{C_0 (L_e / L)^2 (SSA)_{pt}^{\ 2}} \frac{\gamma}{\mu} \tag{3-28}$$

Since effective porosity rather than total porosity determines the hydraulic characteristics, it is desirable to use effective porosity ϕ_e and $(SSA)_{pe}$ replace total porosity ϕ_t and $(SSA)_{pt}$ in (3-28),

$$k = \frac{\phi_e}{C_0 (L_e / L)^2 (SSA)_{pe}^{\ 2}} \frac{\gamma}{\mu} \tag{3-29}$$

In order to take into account the effect of cross-section area of each pathway on flow, a weighted tortuosity $(L_e/L)_w$ is used. The weighting methodology can be found elseIn this expression (kuang and Sansalone 2005). The modified Kozeny-Carman model can be presented as the following form.

$$k = \frac{\phi_e}{C_0 (L_e / L)_w^2 (SSA)_{pe}^{\ 2}} \frac{\gamma}{\mu} \tag{3-30}$$

This modified model takes into account the following factors that were rarely considered previously: effective porosity, pore connectivity and pore size distribution. All these factors affect flow characteristics significantly in porous media.

After ϕ_e and $(L_e/L)_w$ are employed, another problem as mentioned above is to determine the scale of $(SSA)_{pe}$. Specific surface area measured by experiments, such as EGME (ethylene glycol monoethyl ether) or nitrogen adsorption, almost always overestimates the relevant length scale for fluid flow (Garboczi 1990). This is because cementitious materials usually have an extremely high surface area, due to the complicated structure of C-S-H gel on a very fine scale, but pore sizes, relevant to fluid flow, are not significantly affected by such fine scale pores (Xi and Bažant, 1999). Pores on the order of 10 μm or less require a pressure head that is not available even under ponded conditions on the CPP surface (the maximum depth of ponding is 6

mm). According to Berryman and Blair's finding (1987), pores finer than 1/100 of the median size did not significantly influence flow. Using (SSA) measured by EGME method, yields too much underestimation of hydraulic conductivity results (Schaap and Lebron 2001). So it is very important to determine what scale of pores should take into account for (SSA) calculation and to obtain the pore size distribution $(PSD)_{pore}$ of CPP. CPP pore size distribution was examined using XRT as illustrated in Chapter 2. The area based median pore size d_{50a} of CPP is around 3425 μm which is independent on image resolution R_r. pores with diameter less than 34.25 μm may be reasonably neglected in terms of hydraulic property estimation.

The relationship between (SSA) and resolution R_r (μm) was developed in Chapter 2 as (2-25) shows.

$$(SSA)_s = \frac{228.38(\phi_t)^{1.76}}{(R_r)^{0.716}}$$

From this equation, (SSA) under a certain resolution could be derived by the (SSA) under 35 μm, as illustrated in (2-28)

$$(SSA)_{s-0} = (\frac{R_{r0}}{R_{r1}})^{0.716} \cdot (SSA)_{s-35}$$

In this expression, R_{r1}=35 μm. (SSA) based on resolution of R_r = 35 μm are shown in Table 2-4. When pores finer than d_0 (μm) can be eliminated, R_{r0} in the above equation can be obtained based on the equivalent area between a circle with diameter of 34.25 μm and a square with side length of R_{r0}.

$$R_{r0}^2 = \pi \cdot d_0^{\,2} / 4 \qquad (3\text{-}31)$$

When d_0 = 34.25 μm, R_{r0} = 30 μm. Substituting R_{r0} = 30 μm to (2-28), (SSA) based on resolution of 30 μm could be obtained, in which pores finer than 34.25 μm are neglected.

According to Berryman and Blair's finding (1987), although the measured image specific surface was considerably smaller in magnitude than the true specific surface area of the material due to resolution constraints, these smaller values were nevertheless the required input to the Kozeny-Carman relation.

3.6 RESULT ANALYSIS

3.6.1 Empirical Models

Based on aggregate and pore characteristics of the 19 CPP specimens, using the above empirical models, hydraulic conductivity for each specimen could be estimated as Table 3-2 shows. Figure 3-2 shows the comparison of hydraulic conductivity results by experimental measurements and empirical model calculations in which total porosity ϕ_t were used.

From Figure 3-2, it is found that Krüger model agreed with experimental measurements best, and the relative different percentages (RDP) were less than 50%. Fair-Hatch and Terzaghi model agree with experimental measurements in some degree (RDP<80%) when total porosity is less than 15%. Bayer and Slichter model agree with experimental measurements in some degree (RDP<50%) when total porosity is less than 14%. Hazan model generated unreasonably negative values when total porosity ϕ_t is less than 15% and generates higher RDP with the increase of ϕ_t, so it is not applicable for CPP hydraulic conductivity analysis. USBR model is also not applicable for CPP hydraulic conductivity analysis since it does not take into account the porosity. The reason of the invalidity of those empirical models for CPP hydraulic conductivity analysis is that most of these empirical methods were developed for soil and sand materials which have quite different aggregate and pore properties from that of CPP. None of these empirical models consider the pore size distribution which, however, is one of the most important factors determining hydraulic properties of CPP materials.

Table 3-2 Comparison of hydraulic conductivity, k (10^{-3} cm/s), by experimental measurements and empirical equations

CPP Core	Measured k	Calculated k (10^{-3} cm/s) based on empirical equations											
		Krüger		Hazen		Slichter		Terzaghi		Beyer		Fair-Hatch	
		k	(RDP) (%)	K	(RDP) (%)	k	(RDP) (%)	k	(RDP) (%)	k	(RDP) (%)	k	(RDP) (%)
LC1-4	5.68	3.9	31.27	-257.93	4641	3.79	33.23	4.12	27.53	3.58	37.04	2.09	63.19
LC1-6	7.82	4.32	44.76	-220.69	2922	4.97	36.49	2.08	73.39	4.66	40.38	2.73	65.14
LC1-5	5.04	4.57	9.41	-199.28	4054	5.74	13.98	1.22	75.82	5.38	6.83	3.15	37.53
LC2-8	4.45	5.17	16.20	-148.47	3436	7.92	78.06	0.09	98.04	7.42	66.64	4.34	2.56
LC2-2	11.95	6.15	48.50	-71.05	695	12.26	2.60	0.91	92.42	11.51	3.68	6.73	43.68
LC2-9	5.02	6.41	27.72	-51.76	1131	13.55	170.00	1.60	68.14	12.75	153.91	7.45	48.47
C2-6	10.96	7.28	33.56	10.88	1	18.41	67.95	5.24	52.17	17.44	59.13	10.20	6.95
C2-1	12.85	7.71	39.97	40.49	215	21.08	64.01	7.72	39.93	20.06	56.10	11.73	8.72
C1-5	7.88	8.35	5.92	82.36	945	25.29	220.95	12.07	53.16	24.25	207.77	14.18	79.97
C2-5	9.02	9.24	2.45	138.63	1437	31.83	252.93	19.52	116.36	30.89	242.45	18.06	100.25
C2-3	10.84	9.26	14.60	139.63	1188	31.96	194.84	19.66	81.41	31.02	186.15	18.14	67.32
C2-12	11.96	9.71	18.80	166.90	1295	35.53	197.06	23.97	100.39	34.70	190.15	20.29	69.66
C2-11	14.54	10.39	28.56	206.13	1318	41.14	182.91	30.95	112.87	40.58	179.09	23.73	63.20
LC2-1	16.87	10.71	36.54	224.08	1228	43.89	160.20	34.46	104.30	43.51	157.92	25.44	50.81
S2-4	21.77	12.10	44.43	298.55	1271	56.73	160.58	51.23	135.34	57.46	163.96	33.60	54.35
S2-2	20.66	13.54	34.44	370.21	1692	71.34	245.32	70.81	242.74	73.97	258.05	43.26	109.37
S1-4	22.41	14.55	35.09	416.64	1759	82.10	266.35	85.37	280.97	86.53	286.10	50.60	125.77
S1-5	28.76	16.43	42.87	498.05	1632	103.60	260.22	114.63	298.58	112.60	291.53	65.84	128.94
S1-8	32.86	18.68	43.16	586.05	1683	130.94	298.47	151.85	362.12	147.59	349.14	86.30	162.63

k: hydraulic conductivity (10^{-3} cm/s);

(RDP): relative different percentage;

$$(RDP) = \frac{|\text{measured k - calculated k}|}{\text{measured k}} \times 100\%$$

USBR equation: since it is only the function of d_{20}, the calculated k for all the specimens are the same as 457.16×10^{-3} cm/s;

Hazan equation: it generates unreasonably negative values, obviously not be applicable for CPP hydraulic conductivity analysis.

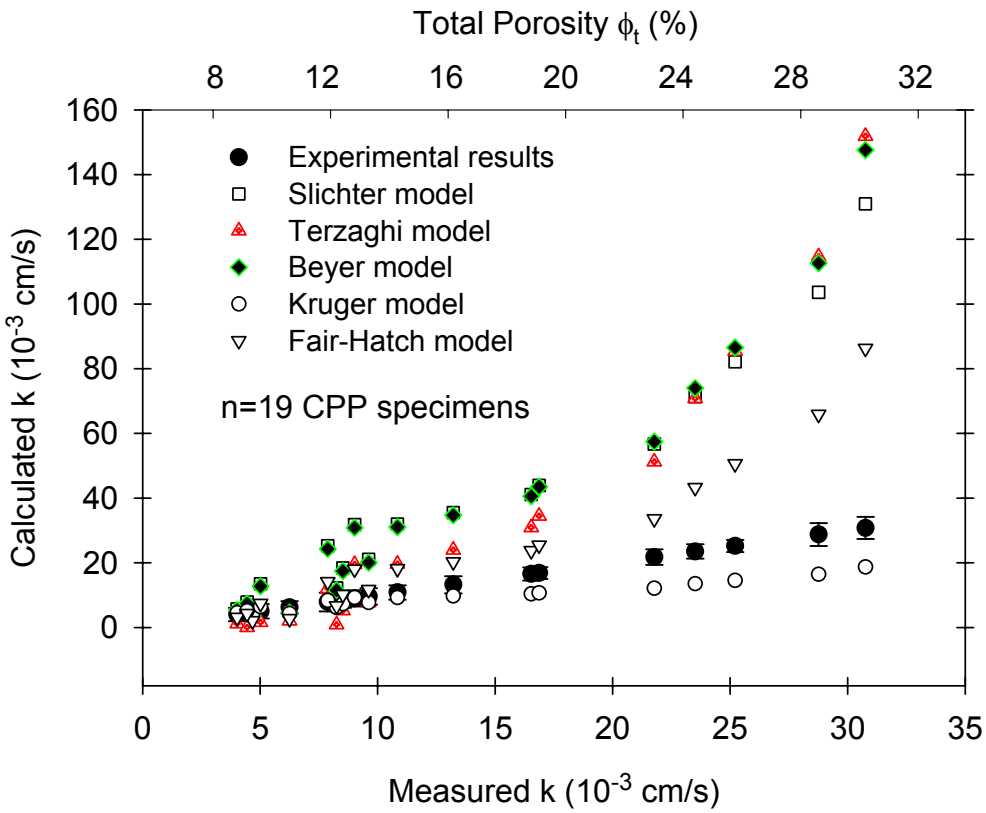

Figure 3-2 Comparison of hydraulic conductivity obtained by empirical equation and experimental measurements. This plot shows that the calculated results by Slichter, Terzaghi, Beyer, Kruger and Fair-Hatch model agree with measured results when total porosity ϕ_t is less than 15%. For the case ϕ_t greater than 15%, none of these models is applicable for CPP hydraulic conductivity prediction. Kruger model is the best fit with but lower than experimental measurements.

Conventional Kozeny-Carman model is the most successful method for permeability analyzing (Berryman and Blair 1987), but it was found that the original form, as equation (3-26) shows, was not applicable for CPP hydraulic conductivity estimation. EGME measurement results showed that $(SSA)_s$ of CPP is in the range of $1.3\sim4.5\times10^6$ m^{-1}. $(SSA)_{pt}$ and $(SSA)_{pe}$ could be estimated using (2-15) and (2-22). Using (SSA) measured by EGME method yields unreasonably smaller hydraulic conductivity results. Table 3-3 shows the hydraulic conductivity results based on (3-28) and (3-30) for the 19 specimens when EGME measured (SSA) were used.

Table 3-3 Comparison of hydraulic conductivity results using Kozeny –Carman equation based on EGME measured (SSA)

CPP Specimens	Measured k (10^{-3} cm/s)	Calculated k (10^{-3} cm/s)	
		Using equation (28)	k by equation (30)
LC1-4	5.68	5.94E-06	1.98E-06
LC1-6	7.82	6.34E-06	1.88E-06
LC1-5	5.04	6.16E-06	1.94E-06
LC2-8	4.45	7.51E-06	2.61E-06
LC2-2	11.95	1.23E-05	5.49E-06
LC2-9	5.02	1.06E-05	3.79E-06
C2-6	10.96	1.51E-05	8.05E-06
C2-1	12.85	1.82E-05	9.22E-06
C1-5	7.88	1.59E-05	8.91E-06
C2-5	9.02	2.52E-05	1.35E-05
C2-3	10.84	3.10E-05	1.47E-05
C2-12	11.96	3.70E-05	1.87E-05
C2-11	14.54	4.11E-05	2.45E-05
LC2-10	16.87	5.23E-05	2.79E-05
S2-4	21.77	8.75E-05	5.11E-05
S2-2	20.66	1.06E-04	7.00E-05
S1-4	22.41	1.36E-04	9.17E-05
S1-5	28.76	2.12E-04	1.49E-04
S1-8	32.86	3.43E-04	2.49E-04

$(SSA)_s$ were measured by EGME directly.
(RDP): relative different percentage.

In equation (3-28), total porosity and $(SSA)_{pt}$ were employed, while in (3-30), effective porosity, $(SSA)_{pe}$ based on effective pore volume, and weighted tortuosity (L_e/L) were used. Figure 3-3 shows the comparison of measured k_{sat} with calculated k_{sat} by conventional KCM. Compared to experimental measurements, it is found that hydraulic conductivity was underestimated by magnitude of 4-5 orders. The main reason is that fine pores contribute significantly to the value of (SSA), but little to hydraulic conductivity (Flint and Selker 2003). When applying (SSA) from EGME measurements to Kozeny-Carman model, fine pores' contribution to flow was significantly overestimated.

3.6.2 Modified KCM Using (SSA) based on Image Analysis

Based on X-ray tomographic analysis results, the area based median size of pores, d_{50a}, in CPP is 3425 μm. (SSA) based on resolution of 35 μm was shown in Table 2-4. Using equation (2-28), (SSA) based on image resolution of 30 μm was shown in Table 3-4. Based on (3-30), hydraulic conductivity of each specimen was calculated as Table 3-4 illustrates also.

Weighted tortuosity $(L_e/L)_w$ were also used in this procedure. It is found that the (SSA) from image analysis were much smaller in magnitude than the true specific surface area of the material, but these smaller values are reasonable for hydraulic conductivity calculation, which agree well with Berryman and Blair's finding (1987). Figure 3-4 shows that calculated results of hydraulic conductivity using (SSA) based on image resolution of 30 μm agree better with experimental results than that using (SSA) based on image resolution of 35 μm. It demonstrates that pore size distribution is a key factor for fluid flow in porous media, and pores with size smaller than 1/100 of d_{50a} could be reasonably neglected.

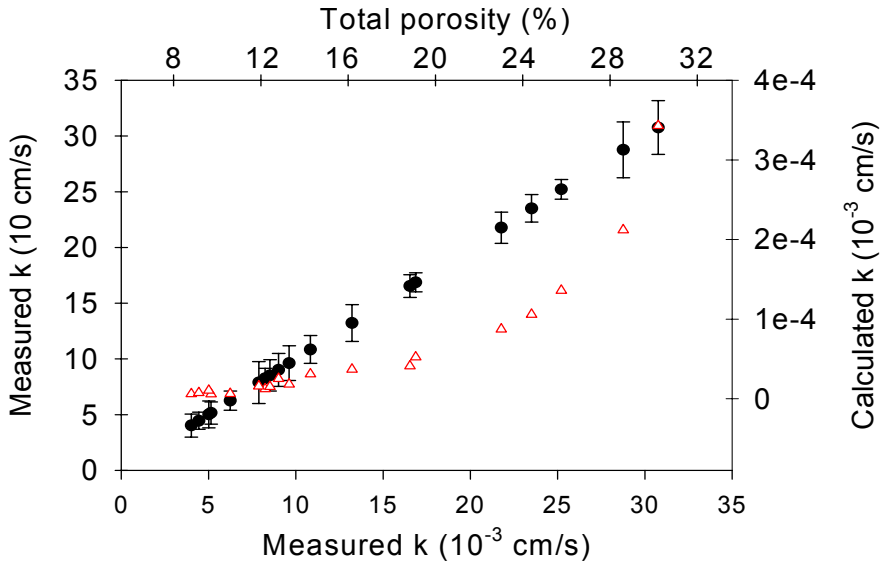

Figure 3-3 Comparison of hydraulic conductivity obtained by conventional Kozeny-Carman model to that by experimental measurements.

Table 3-4 Comparison of hydraulic conductivity (10^{-3} m/s) results using Kozeny –Carman equation based on (SSA) obtained by tomography analysis

CPP Spec.	Measured k (10^{-3} m/s)	$(SSA)_{pe}$ by tomography Analysis (m^2/m^3)		Calculated k(10^{-3} cm/s)			
				Using $(SSA)_{pe}$ with resolution of 35 μm		Using $(SSA)_{pe}$ with resolution of 30 μm	
		R_r=35 μm	R_r=30 μm	k	RDP (%)	k	RDP (%)
LC1-4	5.68	15261	17046	6.96	22.52	5.58	1.80
LC1-6	7.82	11569	12922	9.56	22.30	7.67	1.97
LC1-5	5.04	13696	15298	6.37	26.45	5.11	1.35
LC2-8	4.45	15442	17248	5.42	21.76	4.34	2.40
LC2-2	11.95	11219	12531	15.88	32.87	12.73	6.50
LC2-9	5.02	14772	16500	5.88	17.19	4.72	6.07
C2-6	10.96	12654	14134	13.65	24.56	10.94	0.16
C2-1	12.85	11798	13179	16.30	26.82	13.06	1.63
C1-5	7.88	13547	15132	10.45	32.61	8.37	6.28
C2-5	9.02	14921	16667	10.97	21.62	8.79	2.53
C2-3	10.84	14008	15647	13.57	25.21	10.88	0.36
C2-12	11.96	15217	16997	13.44	12.36	10.77	9.94
C2-11	14.54	14490	16185	17.40	19.67	13.95	4.08
LC2-10	16.87	14230	15894	19.51	15.67	15.64	7.28
S2-4	21.77	15263	17048	25.48	17.04	20.42	6.19
S2-2	20.66	16998	18987	23.42	13.34	18.77	9.16
S1-4	22.41	17433	19473	26.05	16.23	20.87	6.85
S1-5	28.76	18061	20174	32.56	13.20	26.09	9.27
S1-8	32.86	18758	20952	41.23	25.48	33.05	0.58

Calculated k based on Kozeny-Carman Equation (3-30);
$(SSA)_{pe}$ under image resolution, R_r, of 30 μm were calculated by the Equation (2-28);
$(SSA)_{pe}$ of 35 μm were known by tomography analysis;
(RDP): relative different percentage
R_r: image resolution

Weighted tortuosity $(L_e/L)_w$ were also used in this procedure. It is found that the (SSA) from image analysis were much smaller in magnitude than the true specific surface area of the material, but these smaller values are reasonable for hydraulic conductivity calculation, which agree well with Berryman and Blair's finding (1987). Using the tomographically analyzed (SSA) yields small relative different percentage (<10%). Figure 3-4 shows that calculated results of hydraulic conductivity using (SSA) based on image resolution of 30 μm agree better with experimental results than that using (SSA) based on image resolution of 35 μm. It shows clearly

that pore size distribution is a key factor for fluid flow, and pores with size smaller than 1/100 of d_{50a} is reasonably to be neglected, while pores larger than 1/100 of d_{50a} should take into account.

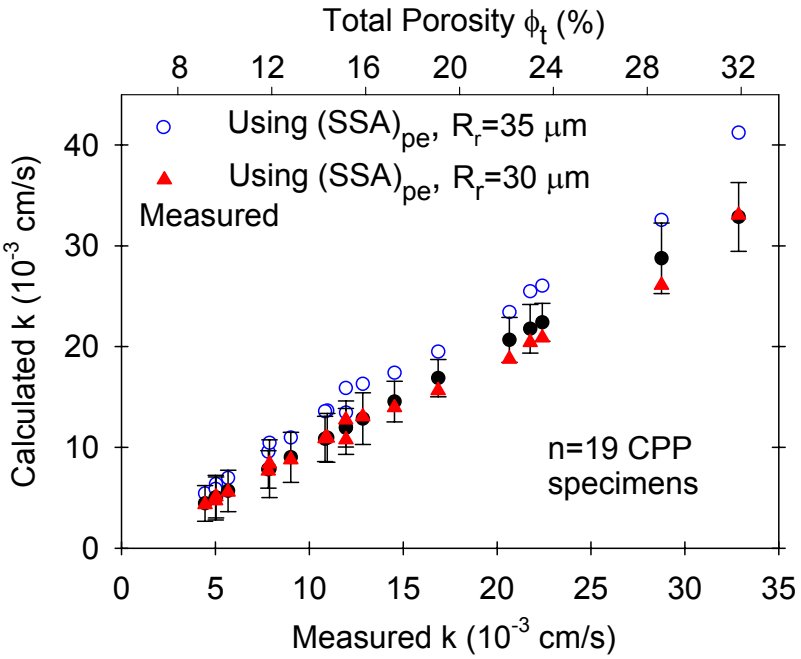

Figure 3-4 Comparison of hydraulic conductivity obtained by Kozeny-Carman equation and experimental measurements. According to tomography analysis, median pore size of CPP is about 3000 μm. Using $(SSA)_{pe}$ based on tomographic analysis in resolution of 30 μm generates results agreeable with measured results well. $(SSA)_{pe}$ represents specific surface area based on effective pores, and R_r is the image resolution in tomography analysis

3.6.3 Modified KCM Using Un-Weighted and Weighted Tortuosity

Another task of this study is to measure the effect of flow pathway characteristics on flow transport. According to the findings of Flint and Selker (2003), if pores of different sizes are operating serially, the sequential variation in the effective cross section of flow channels tends to result in a *k* associated with the smaller cross section. Calculation k based on un-weighted tortuosity (L_e/L) and weighted tortuosity $(L_e/L)_w$ was compared in Table 3-5 using (3-29) and (3-30), respectively. Figure 3-5 shows that weighted tortuosity $(L_e/L)_w$ were more reasonable and generated the results agreeable with experimental measurements results. Un-weighted tortuosity generates unreasonable results when porosity is more than 18%.

Table 3-5 Calculated results using un-weighted and weighted tortuosity in modified KCM

CPP Spec.	Measured k (10^{-3} m/s)	Un-weighted $(L_e/L)_0$	Weighted tortuosity $(L_e/L)_w$	Calculated k (10^{-3} cm/s) [1]			
				Based on $(L_e/L)_0$	RDP (%)	Based on $(L_e/L)_w$	RDP (%)
LC1-4	5.68	4.57	3.42	2.75	51.60	5.58	1.80
LC1-6	7.82	4.23	3.78	5.39	31.11	7.67	1.97
LC1-5	5.04	5.18	4.12	2.84	43.58	5.11	1.35
LC2-8	4.45	5.91	4.38	2.10	52.83	4.34	2.40
LC2-2	11.95	3.87	4.26	13.57	13.56	12.73	6.50
LC2-9	5.02	3.97	4.83	6.14	22.35	4.72	6.07
C2-6	10.96	4.12	4.73	12.69	15.80	10.94	0.16
C2-1	12.85	4.26	4.62	13.52	5.19	13.06	1.63
C1-5	7.88	4.87	5.45	9.23	17.13	8.37	6.28
C2-5	9.02	3.68	4.88	13.61	50.83	8.79	2.53
C2-3	10.84	3.59	4.41	14.45	33.26	10.88	0.36
C2-12	11.96	4.25	4.27	9.57	20.00	10.77	9.94
C2-11	14.54	5.46	4.38	7.90	45.68	13.95	4.08
LC2-10	16.87	3.36	4.02	19.70	16.80	15.64	7.28
S2-4	21.77	4.52	3.57	11.21	48.50	20.42	6.19
S2-2	20.66	4.19	3.68	12.74	38.34	18.77	9.16
S1-4	22.41	4.29	3.52	12.37	44.81	20.87	6.85
S1-5	28.76	4.36	3.21	12.45	56.72	26.09	9.27
S1-8	32.86	4.67	2.89	11.14	66.10	33.05	0.58

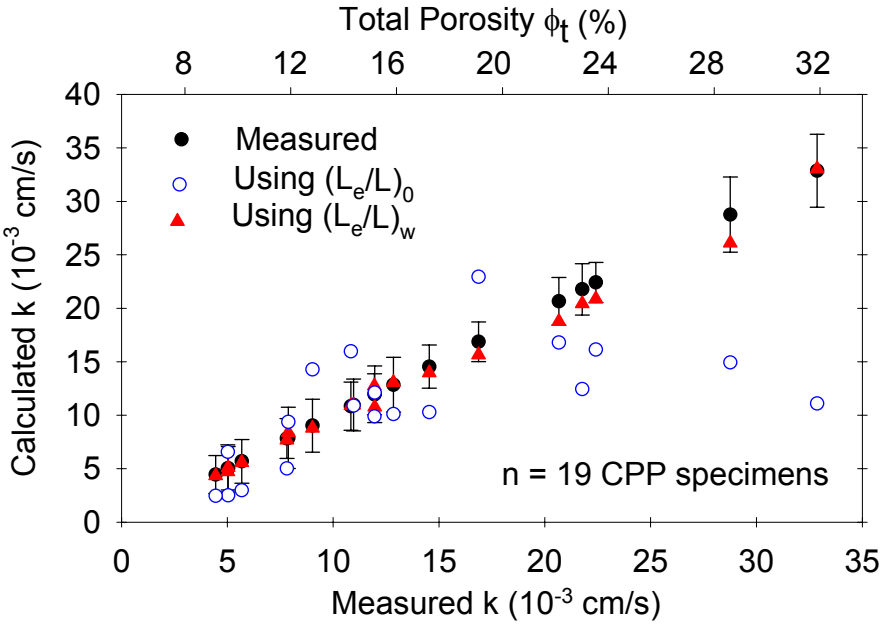

Figure 3-5 This plot shows the influence of tortuosity on calculated hydraulic conductivity by Kozeny-Carman equation.

3.6.4 k-ϕ_t and k-ϕ_e Relationship

Based on experimental measurements of hydraulic conductivity k and specimen effective porosity ϕ_e, as illustrated in Table 2-4, k_{sat}-ϕ_e relationship was presented in Figure 3-6. It can be modeled by the following expression.

$$k_{sat} = 0.7024(\phi_e)^{1.1452} \tag{3-32}$$

Figure 3-7 illustrated the relationship between k_{sat} and ϕ_t, which could be modeled by the following expression.

$$k_{sat} = 0.0286(\phi_t)^{2.0721} \tag{3-33}$$

These models make it possible to estimate CPP hydraulic conductivity based on its total porosity which can be obtained by geometric and gravimetric properties. It has to point out, however, that this model may not be applicable for porous media with similar pore size distribution as CPP.

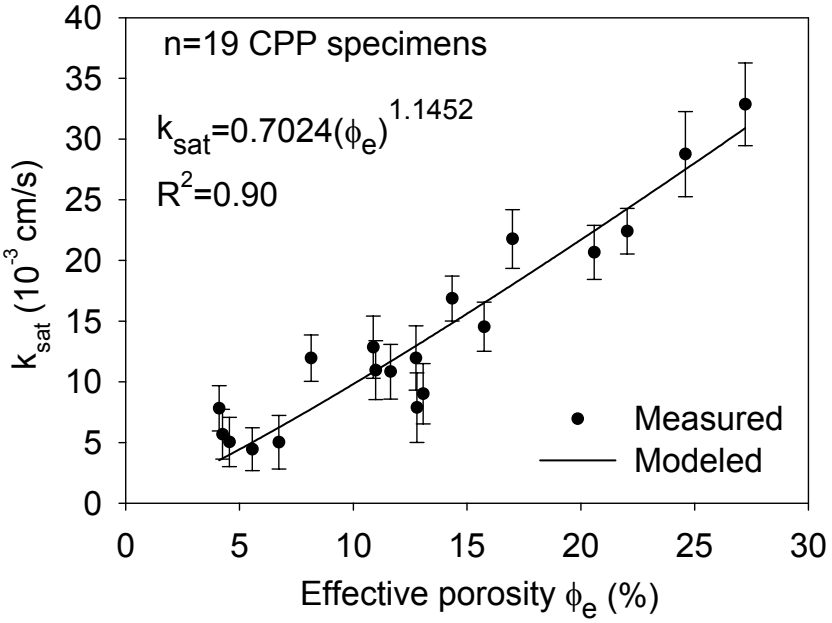

Figure 3-6 Relationship between hydraulic conductivity k and effective porosity ϕ_e. Range bars represent standard deviation of measured hydraulic conductivity in a given ϕ_e.

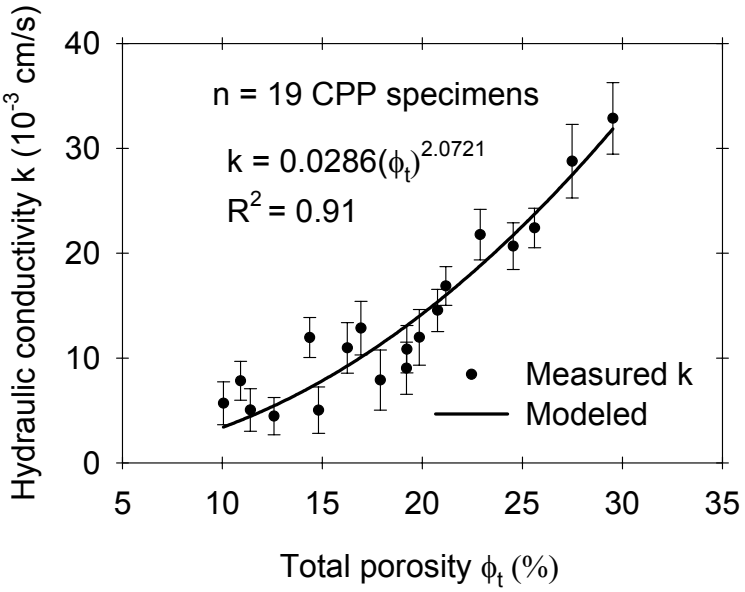

Figure 3-7 Relationship between hydraulic conductivity k and total porosity ϕ_t. The relationship was modeled by a power law model as $k = 0.0286 \times (\phi_t)^{2.0271}$ with $R^2 = 0.91$. In this expression, k is in 10^{-3} cm/s and ϕ_t in %. Range bars represent standard deviation of measured hydraulic conductivity for a given ϕ_t.

3.7 SUMMARY AND CONCLUSIONS

Hydraulic characteristics are one of the most important concerns for permeable pavement. In this study, 19 cementitious permeable pavement (CPP) specimens taken from a prototype partial exfiltration reactor loaded by rainfall or rainfall-runoff were utilized to present hydraulic characteristics results. An experiment was designed to measure saturated hydraulic conductivity with constant head. Calculation results based on some empirical models, such as Kozeny-Carman model (KCM), Krüger model, Fair-Hatch model, Hagan model, USBR model, Beyer model and Terzaghi model, were compared to the experimental measurements. It was found that Hazen and USBR model were not applicable for CPP hydraulic conductivity analysis at all. Compared to these models, Krüger model agreed with experimental measurements best, but it generates underestimated results with relative different percentage about 50%, and with the increase of total porosity, it generates increased errors. Fair-Hatch, Terzaghi, Bayer and Slichter

model agree with experimental measurements with RDP<80% when total porosity is less than 15%. Since the typical porosity in CPP is more than 20%, all of these empirical models are not desirable for CPP hydraulic conductivity analysis.

Kozeny-Carman model is the most successful method for permeability analysis, but the conventional form of KCM is found not applicable for CPP hydraulic conductivity estimation. Recognizing the significant contribution of pore size distribution, a modified Kozeny-Carman model was presented, in which effective porosity ϕ_e, specific surface area based on effective pores $(SSA)_{pe}$, and weighted tortuosity $(L_e/L)_w$ were employed, generating results agree with measured ones well. This model can be used to accurately analyze hydraulic conductivity for CPP with known pore characteristics.

Factors that significantly influence fluid flow in porous media include porosity, pore connectivity and pore size distribution. These pore characteristics were represented by effective porosity, area based median pore size d_{50a}, weighted tortuosity $(L_e/L)_w$, and specific surface area based on effective pores with size larger than 1/100 of d_{50a}. It is found necessary to weight flow pathways based on their cross-section areas formed by different size of pores. Weighted tortuosity generates much more reasonable and accurate results of hydraulic conductivity for CPP using the KCM. Un-weighted tortuosity generates unreasonable result trends when porosity is more than 10%.

How to determine the pore scale for (SSA) is very important in KCM. (SSA) obtained by EGME method generates underestimated hydraulic conductivity in 3-5 order of magnitude. It is found necessary to neglect the pores that have little contribution to fluid flow but significant contribution to (SSA). For CPP, pores with size smaller than 1/100 of d_{50a} may be neglected,

which generate much smaller (SSA) than EGME test, but this (SSA) generates hydraulic conductivity results agree well with measured results by using KCM.

Both the K_{sat}- ϕ_t relationship and k_{sat}- ϕ_e relationship were modeled by a power law model. These relationships make it possible to predict CPP hydraulic conductivity knowing total porosity which can be obtained conventionally by CPP's geometrics and gravimetrics.

As a whole, this study discussed important factors that influence fluid flow in CPP, and provided methods to predict hydraulic conductivity for porous media with similar pore size distribution to CPP.

3.8 NOTATION

d_{50a} = area based median pore size (L);

d_e = effective aggregate size (L);

i = hydraulic gradient (L/L);

k = hydraulic conductivity (L/T);

K = Permeability (L^2);

L = length of a specimen in z direction (L);

L_e = weighted length of all fluid pathways formed by effective pores (L);

$(Le/L)_0$, $(Le/L)_w$ = un-weighted and weighted tortuosity (L/L);

Re = Reynolds number;

R_r = resolution (L);

R_w: = hydraulic radii (L);

SSA = specific surface area (L^2L^{-3});

V = seepage velocity (L/T);

d_{50a}, = median pore diameter based on area distribution (L);

ϕ_e, ϕ_t = effective porosity and total porosity (L^3L^{-2});

Δh = head loss (L)

η = coefficient of uniformity of aggregate

μ = dynamic viscosity (MTL^{-2});

ν = kinematic viscosity (L^2T^{-1})

3.9 REFERENCES

Ahuja, LR., Cassel, D.K. Bruce, R.R. and Barnes, B.B., 1989. "Evaluation of spatial distribution of hydraulic conductivity using effective porosity data." *Soil Science*, 148, 401-411

Al-Omari, L.T., Masad, E., Cooley, A. and Harman, T. (2002). "Proposed methodology for predicting HMA Permeability." *Journal of the Association of the Asphalt PavingTechnologists*, 71, 30-58.

Asaeda, T., and Ca, V.T. (2000). "Characteristics of permeable pavement during hot summer weather and impacton the thermal environment." *Can. Build. & Env.,* 35, 363-375.

Andersen, C.T., Foster, I.D.L., and Pratt, C.J. (1999). "The role of surfaces (permeable pavement) in regulating drainage and evaporation: development of a laboratory simulation experiment." *Hydrological Processes*, 13, 597-609.

Bäckström, M. (2000). "Ground temperature in porous pavement during freezing and thawing." *Journal of Transportation Engineering, ASCE*, 375-381.

Bäckström, M. and Bergström, A. (2000). "Draining function of porous asphalt during snowmelt and temporary freezing." *Can. J. Civil. Eng.*, 27, 594-598.

Berryman, J.G., and Blair, S.C. (1986). "Use of digital image analysis to estimate fluid permeability of porous materials: application of two-point correlation function." *J. Appl. Phys*., 60(6), 1930-1938.

Berryman, J.G., and Blair, S.C. (1987). "Kozeny-Carman relations and image processing methods for estimating Darcy's constant." *J. Appl. Phys*., 62 (6), 2221-2228.

Bérengier, M.C., Stinson M.R., Daigle, G.A., and Hamet, J.F. (1997). "Porous road pavements: Acoustical characterization and propagation effects." *Journal of Acoustic Society of America*, 101(1), 155-162.

Brattebo, B.O., and Booth, D.B. (2003). "Long-term Stormwater quantity and quality performance of permeable pavement systems." *Water Research*, 37, 4369-4376.

Carman, P.C. (1956). *Flow of Gases Through Porous Media*, New York, Academic Press Inc.

Choubane, Page, B., G. and Musselman, J., 1998. "Investigation of water permeability of coarse graded superpave pavements." *Journal of Association of Asphalt Paving Technologists*, vol. 67,

Cooley, L.A. and Brown, E.R. (2000). "Selection and evaluation of a field permeability device for asphalt pavements." *TRB, National Research Council*, no.1723, Washington, D.C.

Davies, L., and Dollimore, D., 1980. "Theoretical and experimental values for the parameter k of the kozeny-Carman model, as applied to sedimenting suspensions." *J. Phys. D: Appl. Phys*., 13, 20130-2020

Diniz, E.V., 1980. "*Porous Pavement Phase I design and operation*." EPA, Municipal Environment Research Lab, OH.

Dixon, D.A., J. Graham, and M.N. Gray, 1999. "Hydraulic conductivity of clays in confined tests under low hydraulic gradient." *Canadian Geotechnical Journal*, 36, 815-825

Dullien, F. (1992). *Porous Media: Fluid Transport and Pore Structure*, Academic, NY, 1992.

Fach, S., Geiger, W.F. and Dierkes, C. (2002). "Development of an assessment procedure for porous pavements." *9th Conference on Urban Drainage 2002 in Portland.*

Fwa, T.F., Tan, S.A., and Guwe, Y.K., 1999. "Laboratory Evaluation of Clogging Potential of Porous Asphalt Mixtures." *Transportation Research Record* 1681, 43-49.

Giménez, D., Allmaras, R.R., Huggins, D.R. and Nater, E.A. (1997). "Prediction of the Saturated Hydraulic Conductivity-Porosity Dependence Using Fractals." *Soil Science Society of America*, 5, 1285-1292.

Field, R., Masters, H., and Singer, M., 1982. "Status of porous pavement research." *Water Research*, 16, 849-858.

Field, R., Masters, H., and Singer, M. (1982). "Porous pavement: research; development; and demonstration." *Journal of Transportation Engineering*, *ASCE*, 108, 244-258

Flind L.E., and Selker, J.S. (2003). "Use of porosity to estimate hydraulic properties of volcanic tuffs." *Advances in Water Resources*, 26, 561-571.

Garboczi, E.J., Permeability, diffusivity, and microstructural parameters: a critical review, *Cement and Concrete Research*, vol. 20, pp 591-601, 1990

Ghafoori, N., and Dutta, S. (1995). "Laboratory investigation of compacted no-fines concrete for paving materials." *Journal of Materials in Civil Engineering*, *ASCE*, 7(3), 183-191.

Ghafoori, N., and Dutta, S. (1995). "Pavement thickness design for no-fine concrete parking lots." *Journal of Transportation Engineering*, *ASCE*, 121(6), 476-484

Gimenez, D., Allmaras, R.R., Huggins, D.R., and Nater, E.A., 1997. "Prediction of the saturated hydraulic conductivity-porosity dependence using fractals." *Soil Science Society of America Journal*, 61(5), 1285-1292.

Hainin, M.R., Cooley, L.A., and Prowell, B.D., 2003, "An inverstigation of factors influencing permeability of superpave mixes." *Publication of 82th Annual Meeting of TRB*.

Harvey, J., Mills, T., Scheffy, C., Sousa, J., and Monismish, C.L. (1994). "An evaluation of several techniques for measuring air-void content in asphalt concrete specimens." *Journal of testing and Evaluation*, ASTM, 430.

Hilpert, M., and Miller, C.T. (2001). "Pore-morphology-based simulation of drainage in totally wetting porous media." *Advanced in Water Resources,* 24, 243-255.

Hot Mix Asphalt Technology-September/October 2003, 26-40

Huang, B., Mohammad, L., Raghavendra, A., and Abadie, C. (1999). "Fundamentals of permeability in Asphalt Mixtures." *Journal of the Association of Asphalt Paving Technologists*. Volume 68, pp. 479-500

Isenring, T., Koster, H., and Scazziga, I., 1990. "Experiences with Porous Asphalt in Switzerland." *Transportation Research Record* 1265, pp. 41-53

Jackson, T.J. and Ragan, M. (1974). "Hydrology of porous pavement parking lots." *Journal of the Hydraulics Division*, 1739-1752.

Kanitpong, K., Benson, C.H., and Bahia, H.U. (2001). "Hydraulic conductivity (Permeability) of laboratory compacted asphalt mixtures." *2001 annual meeting of the TRB*. 2001

Kanitpong, K., Bahia,H.U., Benson, C.H., and Wang, X. (2003). "Measuring and predicting hydraulic conductivity (permeability) of compacted asphalt mixtures in the laboratory." *82nd Annual Meeting of TRB*.

Kobayashi, T., Kagata, M., Kodama, T., and Ito, M. (2002). "Development of the environment-friendly hybrid permeable concrete." *Transactions of the Japan Concrete Institute*, 23, pp 65-76.

Kostek, S., Schwartz, L.M., and Johnson, D.L., 1992, "Fluid permeability in porous media: comparison of electrical estimates with hydrodynamical calculations." *Physical Review* B 45(1), 186-195).

Krishnan, J.M., and Rao, C.L. (2001). "Permeability and bleeding of asphalt concrete using mixture theory." *International Journal of Engineering Science*, 39, 611-627

Kuang, X.H., and Sansalone, J., 2005. "X-Ray Tomographic Examination of Permeable Pavement Pore Characteristics: Implications for In-situ Rainfall-Runoff Infiltration, Evaporation and Filtration."

Kuennen T. (2003). "A new era for permeable pavement." *Road Science-Better Road*, 28-32.

Lebron, I., Schaap, M.G., and Suarez, D.L. (1999). "Saturated hydraulic conductivity prediction from microscopic pre geometry measurements and neural network analysis." *Water Resources Research*, 35(10), 3149-3158.

Legret, M., and Colandini, V., 1999. "Effects of a porous pavement with reservoir structure on runoff water: water quality and fate of heavy metals." *Wat. Sci. Tech*., 39(2), 111-117

Li, Y.B., Buchberger, S.G., and Sansalone, J. (1999). "Variably Saturated Flow in Storm –Water Partial Exfiltration Trench." *Journal of Environmental Engineering*, *ASCE*, 556-565

Masad, E., Muhunthan, N., Shashidhar, N., and Harman, T. (1998). "Internal structure characterization of asphalt concrete using image analysis." *Journal of Computation in Civil Engineering*, 13, 88-95

Masad, E., Birgisson, B., Al-Omari, A., and Cooley, A. (2002). "Analysis of Permeability and Fluid Flow in Asphalt Mixes." *The 82th Annual TRB Meeting CD-ROM*.

Maupin, G.W. Jr. (2000). "Asphalt permeability testing in Virginia." *Journal of the TRB*, 1723.

Meegoda N.J., King, I.P. and Arulanandan, K. (1989). "An expression for the permeability of an isotropic granular media." *International Journal for Numerical and Analytical Methods in Geomechanics*, 13, 579-598.

Metcalf & Eddy (2003). *Wasterwater Engineering Treatment and Reuse*, 4th Edition, McGraw-Hill pulishing Ltd.

Minasny B., and McBratney, A.B., 2000. "Evaluation of hydraulic conductivity pedotransfer functions for Austrlian soil." *Australian Journal of Soil Research*, 38, 905-926.

Mohammad L.N., Herath, A. and Huang, B. (2003). "Evaluation of permeability of superpave asphalt mixtures." *TRB 2003 Annual Meeting CD-ROM*.

Nakashima, Y. and Watanabe, Y. (2002). "Estimate of transport properties of porous media by microfocus x-ray computed tomography and random walk simulation." *Water Resources Research*, 38 (12), 8-1-8-12.

Nakashima, Y., and Yamaguchi, T. 2004, "DMAP.m: a mathematical probram for three-dimensional mapping of tortuosity and porosity of porous media, Bulletim of Geological Survey of Japan 55, 93-103.

Oke T. (1982). "The energetic basis of urban heat island." *Quar. J. Roy. Met. Soc*. 108, 1-24

Pagotto, C., Legret, M., and Cloirec, P.LE, 2000. "Comparison of the hydraulic behaviour and the quality of highway runoff water according to the type of pavement." *Water Research*, 34(18), 4446-44554.

Park, S.B., and Tia, M., 2004. "An experimental study on the water-purification properties of porous concrete." *Cement and Concrete Research*, 34 177-184

Paydar, Z and A.J. Ringrose-Voase, Prediction of hydraulic conductivity for some Australian soils, *Australian Journal of Soil Research*, vol. 41, pp 1077-1088, 2003.

Pratt, C.J., Mantle, J.D., and Schofield, P.A., 1995. "UK research into the performance of permeable pavement, reservoir structures in controlling stromwater discharge quantity and quality." *Water Science Tech.*, 32, 63-69.

Rawls W.J., D.L. Brakensiek, and K.E. Saxton, 1993. "Predicting saturated hydraulic conductivity utilizing fractal principles." *Soil Science Society of America Journal* vol. 57, 1193-1197.

Regalado, C.M., Muňoz-Carpena R., 2004. "Estimating the saturated hydraulic conductivity in a spatially variable soil with different permeameters: a stochastic Kozeny-Carman relation." *Soil & Tillage Research*, 77, 189-202.

Sansalone, J.J., Koran, J.M., Smithson, J.A., and Buchberger, S.G. (1998). "Physical characteristics of urban roadway solids transported during rain events." *J. Environ. Eng*., 124(5), 427-440.

Saripalli, K.P., Serne, R.J., Meyer, P.D., and Mcgrail, B.P. (2002). "Prediction of diffusion coefficients in porous media using tortuosity factors based on interfacial areas." *Ground Water*, 40, 346-352.

Schaap, M.G., and Lebron, I. (2001). "Using microscope observations of thin sections to estimate soil permeability with the Kozeny-Carman equation." *Journal of Hydrology*, 251, 186-201.

Schluter, W., and Jefferies, C., 2002. "Modeling the outflow from a porous pavement." *Urban Water*, 4, 245-253

Seki, K., and Miyazaki, T., 2001, "A mathematical model for biological clogging of uniform porous media." *Water Resources Research,* 37, 2995-2999.

Stotz, G., and Krauth, K, 1994. "The pollution of effluents from pervious pavements of an experimental highway section: first results." *The Science of the Total Environment* 146/147 465-470.

Tan, S.A., T. Fwa and C. Han, 2003. "Clogging Evaluation of permeable bases." *Journal of Transportation Engineering, ASCE*, 309-315.

Teng, Z. and Sansalone, J. (2004). "In-Situ Partial Exfiltration of Rainfall-Runoff-II: Particle Separation." *Journal of Environmental Engineering*, *ASCE*.

Timlin, D.L., L.R. Ahuja, Y. Pachepsky, R.D. Williams, D. Gimenez, and W. Rawls, 1999, "Use of Brooks-Corey Parameters to improve estimates of saturated conductivity from effective porosity." *Soil Science Society of America Journal*, 63, 1086-1092

United States EPA (1999). "Storm water technology fact sheet porous pavement." *EPA 832-F-99-023*.

Wada, Y., H. Miura, R. Tada, and Y. Kodaka, 1997, "Evaluation of An Improvement in Runoff Control By Means of A Construction of an infiltration Sewer Pipe Under a Porous Asphalt Pavement." *Water Sience Tech.*, vol. 36, pp. 397-402

Vukovic, M., Soro, A., and Miladinov, D., 1992. "Determination of Hydraulic Conductivity of Porous Media From Aggregate-Size Composition." *Water Resources Publications*, Colorado.

Watanabe, S. (1995). "Study on storm water control by permeable pavement and infiltration pipes." *Water Science Technology*, 32(1) 25-32.

Xi, Y., and Bažant, Z.P., 1999. "Modeling chloride penetration in saturated concrete." *Journal of Materials in Civil Engineering, ASCE*, Feb., 58-65

Yue,Z.Q., bekking, W., and Morin, I. (1995). "Application of digital image processing to quantitative study of asphalt concrete microstructure." *Transportation Research Record* no.1492, TRB, Nation Research Council, Washington, D.C., 53-60.

Zhang, D., and Knachstedt, M.A., 1995. "Direct simulation of electrical and hydraulic tortuosity in porous solids." *Geophysical Research Letters*, 22(17), 2333-2336

Zhuang, J., Nakayama, K., Yu, G.R., and Miyazaki, T., 2000. "Scaling of saturated hydraulic conductivity: a xomparison of models." *Soil Science*, 165 (9), 718-727

Zube, E. (1962). "Compaction wtudy of asphalt concrete pavements as related to the water permeability test." *Highway Research Board*, Bulletin 358.

CHAPTER 4 FILTRATION AND CLOGGING OF CPP BY PARTICLES IN RUNOFF

4.1 INTRODUCITON

A variety of in situ structural best management practices (BMPs) or unit operations and processes (UOPs) have been developed for stormwater quality and quantity control through infiltration/filtration and some degree of exfiltration (Colandini et al. 1995; Hogland et al. 1987; Teng and Sansalone 2004). Combined with engineered cementitious permeable pavement (CPP) functions as a combined unit operation and process capable of infiltration-exfiltration and treatment of soluble and particulate constituents from stormwater (Fujita 1993; Jahangir-Issa 1998; Legret et al. 1999; Pratt et al. 1989; Sansalone 1999; Teng and Sansalone 2004; Yu 1993). Permeable pavements and engineered permeable subgrades have been able to significantly reduce the impact of a concentration-based first flush effect from mass-limited runoff events (Anderson et al. 1999; Aulenbach and Chan 1998; Rajapakse and Ives 1990). For example, such systems promote infiltration using permeable pavement and granular subgrades for quantity storage, ground water recharge and quality control in many countries; for example, the USA (Brattebo and Booth 2003; Field 1982; Jackson and Ragan 1974, Sansalone 1999; Teng and Sansalone 2004, Sansalone and Teng 2004, Sansalone and Teng 2005), the UK (Anderson et al. 1999; Schluter and Jefferies 2002), Switzerland (Isenring et al. 1990; Xu and Mermoud 2003), Sweden (Backstrom and Bergstrom 2000; Niemczynowicz and Hogland 1987; Teng and Sansalone 2004), Germany (Fach et al. 2002; Stotz and Krauth 1994), Spain (Jimenez and perez 1990), Singapore (Fwa et al. 1999; Tan et al. 2003) and France (Balades et al. 1995; Legret and Colandini 1999; Pagotto et al. 2000). Infiltration-exfiltration systems that include permeable pavement exhibit a high constituent removal capability; for example, the suspended particulate

matter measured as total suspension solids (TSS) can have a mass removal efficiency up to 90%, total phosphorus (TP) up to 65% and total nitrogen (TN) up to 80% (Park and Tia 2004; Sansalone 1999; Teng and Sansalone 2004).

Studies have demonstrated that depending on runoff chemistry, watershed conditions and hydrodynamics, particulate matter can be a primary vector for constituents transported in runoff (Colandini et al. 1995; Teng and Sansalone 2004, Sansalone and Buchberger 1997, Sansalone et al 1998). Constituents such as metal species, hydrocarbons, organics, pesticides and phosphorus can partition to particles (Colandini et al. 1995; Fach et al. 2002; Park and Tia 2004; Sansalone and Cristina 2004, Stotz and Krauth 1994). Therefore it is important to assess the filtration behavior of permeable pavement such as CPP.

4.2 OBJECTIVES

Permeable pavement such as CPP functions as a filtration unit operation and a medium subject to clogging. There are four main tasks of this study evaluating CPP for filtration and clogging. Results are based on application of a constant particle size gradation, classified as sandy silt, and constant head conditions applied to CPP specimens of known pore properties recovered from a partial exfiltration reactor subject to pavement runoff in Cincinnati, OH. All objectives are examined as a function of three levels of constant influent particle concentration (50, 100 and 200 mg/L), within the range of typical of rainfall-runoff event mean values. The first objective of this study examines the particle removal efficiency of these CPP specimens as a function of particle size. The second objective examines the particle size gradation of cumulative strained particles on CPP surface. The third objective is to evaluate the clogging process of CPP specimens through measurement of the CPP hydraulic conductivity. The fourth objective is to

evaluate CPP cleaning methods that can restore the original hydraulic conductivity of the CPP and a methodology to estimate the maintenance period for CPP cleaning.

4.3 BACKGROUND

4.3.1 Particle Size Gradations

Particles in urban runoff encompass wide size gradation ranging in size from less than 1-μm to greater than 10,000-μm. (Sansalone et al. 1998). When particles transported in runoff are strained at the infiltrating surface of permeable pavement, a filter cake or surface mat ("schmutzdecke") of particulate matter can eventually form. The particulate matter is relatively coarse, and is primary sediment and settleable size material (Teng and Sansalone 2004). The schmutzdecke functions as a filter cake and aids particle removal, and protecting deeper specific deposits within the CPP. Due to the formation of schumutzdecke, finer suspended particles less than 25 μm will also be strained on the CPP surface (Sansalone 1999, Teng and Sansalone 2004). Machie (1989) illustrated that coarser particles have a beneficial effect on the capture of fine particles (Stevenson 1997). Initial formation of a schmutzdecke on the CPP surface is observed as a result of accumulations from multiple runoff events loading the CPP of a passive partial exfiltration reactor (PER) infiltrating lateral pavement sheet flow (Teng and Sansalone 2004). However, this schmutzdecke will also result in reduced hydraulic conductivity or increased head loss if the water surface is able to build up on the CPP surface.

4.3.2 Filtration Models

McDowell-Boyer et al. (1986) presented three mechanisms for particle separation during filtration, namely surficial straining, deep-bed filtration and physical chemical diffusion, depending on the ratio of the media diameter d_m (a surrogate for pore diameter) to suspended particles size d_p. Because of the CPP irregular pore-solid interface shape and wide range of pore

size distributions, filtration mechanisms are more reasonably presented by CPP's pore space geometry and pore size distribution rather than CPP solid (aggregate) size (d_m) (Moghadasi et al. 2004). When $d_m/d_p < 10$, particles will not penetrate into the filter and will be separated by surficial straining; when d_m/d_p is between 10 to 20, the main removal mechanism would be deep-bed filtration, and particles would penetrate into the bed and eventually fill the pore space resulting in clogging, and when $d_m/d_p > 20$, the main mechanism is physical-chemical, which does not significantly impact pore space. These mechanisms have been identified for CPP (Teng and Sansalone 2004). Yao *et al.* (1971) and Flagen and Seinfeld (1988) examined an first-order exponential model for mono-sized filtration systems.

In contrast to drinking water or wastewater filters, CPP is usually loaded by very low hydraulic head, generally less than several centimeters. Most pavement systems carry vehicular traffic and therefore water surface buildup is generally minimized and may be only be several centimeters maximum at the outside of the traveled lane. Parking areas can usually tolerate higher water surface buildup because of slower vehicular speeds and because of their use for surface detention followed by either infiltration or controlled surface water discharge.

4.3.3 Role of Clogging

As the CPP pore space and surface accumulates particulate matter, clogging occurs eventually, resulting in a reduced infiltration rate (Balades et al. 1995; Fach et al. 2002; Stotz and Krauth 1994; Tan et al. 2003). Clogging is a significant concern for permeable pavement since a primary function of permeable pavement depends on maintaining a high drainage capacity (Fwa, et. al. 1999; Schlüter and Jefferies 2002, Tan et al. 2003). These particulates may be sand, silt or clay-sized particles, such as abraded pavement or tire debris caused by pavement-tire abrasion. CPP pores become obstructed by particles when particulates are not be able to move through the

CPP structure due to filtration, while accumulation on the CPP surface is also occurring (Balades et al. 1995, Kuang and Sansalone, 2005; Teng and Sansalone 2004). As with any filter, cleaning of the CPP material is required before the infiltration rate drops to unacceptable low level.

Temporal measurements of hydraulic conductivity is the most convenient and appropriate tool to evaluate clogging properties of CPP (Fwa et al. 1999; Isenring et al. 1990; Jiménez and Perez 1990). Jiménez (1990) used the Laboratorio Caminos de Santander (LCS) permeameter to estimate the permeability of the permeable pavement in terms the time a given amount of water takes to penetrate the surface, and developed an equation for hydraulic conductivity *k* of asphalt pavement as a function of time t measured:

$$\ln k = 7.626 - 1.348 \ln t \tag{4-1}$$

In this expression *k* is hydraulic conductivity in cm/s and *t* is time in seconds.

Tan et al. (2003) considered clogging materials retained in pavement sub-base as a factor decreasing the media hydraulic conductivity, and developed a deposit model to predict the infiltration rate of the porous media.

$$k = k_0 \frac{(1-\phi_t)^2}{(\phi_t)^3} \frac{(\phi_t - \alpha\sigma)^3}{[1-(\phi_t - \alpha\sigma)]^2} \tag{4-2}$$

In this expression, k = hydraulic conductivity (mm/s); k_0 = average initial hydraulic conductivity; ϕ_t = total porosity; α = empirical constant, and σ is specific deposit.

$$\sigma = V_d / V_T \tag{4-3}$$

In this expression V_d is the volume of deposited materials and V_T is the total volume of the specimen. This model is more applicable for deep-bed filtration in which the filter porosity is reduced by clogging materials (Ojha and Graham 1991; Seki and Miyazaki 2001; Tobiason and Vigneswaran 1994).

Balades et al. (1995) suggested that the clogged depth was limited to the first several centimeters of the permeable pavement, and compared four types of cleaning methods, moistening followed by sweeping, sweeping followed by suction, suction alone, and high pressure water jet and suction together. It was found that suction as well as high pressure water jet could clean the permeable pavement and recover the infiltration rate to 100% of the initial infiltration value before any clogging occurred.

Since particles strained on the CPP surface form a schmutzdecke which plays an important role in particle removal and clogging, it is desired to develop a methodology to predict the particles strained on the CPP surface at any time period. It would be also advantageous to demonstrate that CPP material could be cleaned and hydraulic conductivity restored.

4.4 METHODOLOGY

4.4.1 Experimental Configuration, Flow and Mass Measurements, Mass Balances

6 CPP specimens with similar pore characteristics were utilized in this study. These specimens were cored from CPP slabs loaded by three years of pavement runoff in urban Cincinnati, OH (Sansalone and Teng 2004, Teng and Sansalone 2004, Sansalone and Teng 2005). Total porosity (ϕ_t) more than 27%, effective porosity (ϕ_e) more than 24 %, area-based pore diameter (d_{50a}) = 200 μm. All the 6 specimens were backwashed and in an empty bed condition before experimentation. Empty bed, initial hydraulic conductivity of these CPP specimens had a mean of 3.0 x 10^{-2} cm/s and a standard deviation of 6 $\times 10^{-3}$ cm/s. The experimental setup was a constant head setup where influent, effluent and bypass quantity and quality were measured.

A constant particle gradation of known dry mass of particles, M_i was mixed with a de-ionized water influent in a well-mixed influent tank that was pumped to the constant head permeameter with a constant flow rate of q_i and mass concentration of [m_i]. Particle gradation followed a sandy silt, a relatively fine gradation for source area runoff (Sansalone et al 1998) and is illustrated in Figure 4-1. Experiment was undertaken with 3 different concentrations, namely 50, 100, and 200 mg/L (Sansalone and Teng 2004, Sansalone et al 1998).

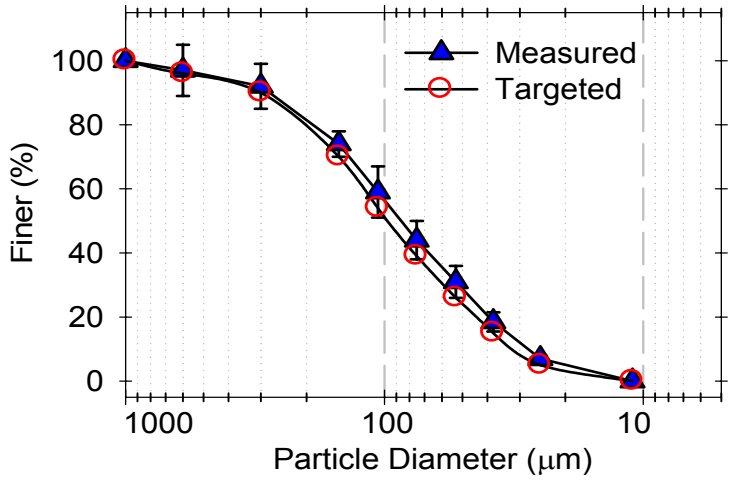

Figure 4-1 Comparison of the measured to the targeted influent particle size gradation

Influent hydraulic loading was kept constant as 22.2 L/m^2-min. Under this loading, hydraulic head was maintained approximately 1 cm above the CPP surface. As hydraulic conductivity decreased due to clogging, bypass overflow was initiated. This bypass was monitored and analyzed for flow rate (influent, q_i , effluent, q_e and overflow, q_o) particle concentration, particle size gradation. Each CPP loading experiment was conducted for a duration that allowed the hydraulic conductivity to decrease from an original range of 10^{-2} cm/s to 10^{-5} cm/s. Samples were taken every three hours for the duration of each loading experiment.

Influent, overflow and effluent were collected into clean polypropylene (PP) containers for the purpose of particle analyses, as determination for M_i, M_o and M_e and overall mass balance determination. When an experiment was ended, the total volume of effluent and overflow were each separately dried at 60°C until a constant mass was achieved. The particle mass from each volume was measured, the particles disaggregated and their size gradation analyzed. Particles strained and filtered by the CPP cores were recovered, dried, weighed, disaggregated and their size gradation determined. Total particle mass, M_i, during the duration of the loading, t_e, was checked through calculation.

$$M_i = [m]_i \cdot q_i \cdot t_e \tag{4-4}$$

In order to recover strained particles and mass, M_s after each loading, CPP specimens were removed from the permeameter, placed into a plastic bag, the permeameter washed into the bag with de-ionized water and the bag then subsequently filled with de-ionized water. The bag was sealed and placed into an ultrasonic cell and sonicated for 30 minutes to recover filtered and strained particles. The CPP specimen was placed in a second clean bag of deionized water and the process repeated to ensure complete removal of all filtered particles. This water and particles were dried in clean open containers at 60°C until a constant mass, M_s was achieved.

Based on measured M_i, M_e, M_o, and M_s, total particle removal efficiency for the duration of CPP specimen loading can be calculated by the following expression.

$$\eta_T = (\frac{M_s}{M_i - M_o}) \times 100\% = (\frac{M_s}{M_s + M_e}) \times 100\% \tag{4-5}$$

Particle mass balance error can be estimated with based on M_i, M_e, M_o, and M_s and the measured amount of original influent mass.

$$E_m = (1 - \frac{M_o + M_s + M_e}{M_i}) \times 100\% \tag{4-6}$$

With known flow rate q and particle concentration $[m]$ in influent, overflow and effluent, total removed particle mass, M_s(t) (mg) during a period of time t can be calculated (and compared to measured values).

$$M_s(t) = [m]_i \cdot q_i \cdot t - [m]_o \int_0^t q_o(t) \cdot t \cdot dt - \int_0^t q_e(t) \cdot t \cdot [m]_e(t)\, dt \tag{4-7}$$

In this expression, $[m]$ represents particle concentration (mg/L), and q represents flow rate (L/s). $[m]_i$, $[m]_o$ and q_i were kept constant, while q_o, q_e, and $[m]_e$ change with time.

4.4.2 Particle and Turbidity Analyses

Particle gradations were determined according to American Society of Testing and Materials (ASTM) D421 for the sample preparation and ASTM D422 for sieve analysis (ASTM 2002) except for the use of additional sieves and a lower drying temperature. The set of sieves was expanded from the ASTM protocol to include the 2-mm through the 25-μm (#500) sieves. Across each gradation, strained particulates were separated into 10 size classes. Dry solids separated on each of the stainless steel sieves were weighted and stored separately. Mass balances were within 2% of the initial total dry mass for each sieve analysis.

PSD for particles in the influent, effluent and overflow samples was analyzed by laser diffraction using a LISST-potable particle analyzer (Sequoia Technology) to determine particle total volume concentration (TVC) distribution for each sample. Each sample was tested no later than 4 hours after sampling and was well-mixed when analyzed for PSDs using laser diffraction. Through PSD analysis, TSS concentration in influent, effluent, and overflow at different time can be obtained for both mass based $[m]$ (mg/L) and number based $[N]$ (count/L). Turbidity for both influent and effluent was measured every 3 hours based on the ASTM D1889-00 (ASTM 2000) using turbidimeter (HACH 2100AN)

4.4.3 Particle Mass Removal Efficiency, η

From PSD analysis results, number concentration of each particle size fraction, d_j could be obtained in both influent, $[N_j]_i$, and effluent, $[N_j]_e$. Number based particle removal efficiency η_n at any time t can be calculated by the following expression.

$$\eta_n(t) = (1 - \frac{[N]_e(t)}{[N]_i(t)}) \times 100\% = (1 - \frac{\sum[N_j]_e}{\sum[N_j]_i}) \times 100\% \quad (4\text{-}8)$$

In this expression, $[N]_i$ and $[N]_e$ are the number of total particles for influent and effluent, respectively, and $[N_j]$ is the number of the *j*th size fraction.

Mass based particle removal efficiency η_m at any time also could be estimated based on PDS analysis results.

$$\eta_m(t) = (1 - \frac{[m]_e(t)}{[m]_i(t)}) \times 100\% = (1 - \frac{\sum[N_j]_e \cdot d_j^3}{\sum[N_j]_i \cdot d_j^3}) \times 100\% \quad (4\text{-}9)$$

In these equations, $[m]_i(t)$ and $[m]_e(t)$ are mass based particle concentration (mg/L) in influent and effluent at time t, respectively. Two assumptions made for η_m calculation here are that all particles are spherical, and all particles have the same specific gravity.

4.4.4 Surficial Cleaning by Sonicating Followed by Backwash and Vacuum Suction

As filtration progresses, particles will begin to fill the upper pore space and create a schmutzdecke, resulting in progressive clogging of the CPP. Clogging and concern regarding inability to restore hydraulic conductivity of permeable pavement, once clogged, are two weaknesses that are commonly cited when permeable pavement applications are considered. In order to examine the ability to restore clogged CPP hydraulic conductivity and to provide a suitable schedule for CPP cleaning, the clogging specimens were cleaned by two methods. The first method was to sonicate the CPP and then backwash the CPP. All particles strained on the

CPP surface were washed from the surface; the specimen was sonicated for 30 minutes, and then backwashed by DI water. The second method was to wash the surface, removing the schmutzdecke, and then to vacuum the surface with a suction of one atmosphere pressure (100 kPa). After the specimens were clean by one of the two methods, hydraulic conductivity was tested with tap water for each specimen to examine to what degree the original hydraulic conductivity was recovered. Based on these results and loading data, a cleaning schedule can be developed.

4.4.5 CPP Cleaning Schedule Decision

Based on hydrologic and loading data for a location, utilizing representative runoff particle concentration $[m]_{in}$ [mg/L], the average dry days between hydrologic events is x, and the average runoff duration of a rainfall events is t_c hours; the total runoff load can be determined on an annual basis. Based on the experimental measurements, the elapsed time, t_e for the hydraulic conductivity of CPP to drop below 10^{-3} cm/s can be determined. The cleaning period (p, yr) would be

$$p \le \frac{t_e}{365 \cdot t_c / x} \tag{4-10}$$

In this expression, t_c is the average runoff concentration time of rainfall events in a given location; t_e is the elapsed time for CPP to drop below an hydraulic conductivity of 10^{-3} cm/s as determined by experiment, x is the average dry days in the interested location.

4.5 RESULTS AND DISCUSSION

A basic summary of the general experimental conditions and results are presented in Table 4-1. In this Table, the elapsed time to let the hydraulic conductivity drop down from initially of 10^{-2} cm/s to 10^{-5} cm/s, and surface strained particles under different particle loading concentrations were illustrated.

Table 4-1 Experimental matrix summary and experimental results

Particle load.	Parameter	Experimental Result		
$[m]_i$ = 50 mg/L	Hydraulic loading rate, Q	22.28 L/m^2-min		
	Elapsed time t_e	252 hours		
	Initial hydraulic conductivity, k_i	3.23×10^{-2} cm/s		
	Final hydraulic conductivity, k_f	6.97×10^{-5} cm/s		
	Strained particle mass	14.0531 grams		
	Surface straining rate	1922.42 g/m^2		
		Influent	**Effluent**	**Overflow**
	Total Volume V (L)	1289.46	280.12	1009.34
	Particle [m] (mg/L)	47.25	$[m]_e = f(t)$	43.28
	Total particle mass (g)	60.9269	2.1489	43.6894
$[m]_i$ =100 mg/L	Hydraulic loading	22.17 L/m^2-min		
	Elapsed time t_e	197 hours		
	Initial hydraulic conductivity, k_i	3.04×10^{-2} cm/s		
	Final hydraulic conductivity, k_f	7.92×10^{-5} cm/s		
	Strained particle mass	15.2368 g		
	Surface straining rate	2084.34 g/m^2		
		Influent	**Effluent**	**Overflow**
	Total Volume V (L)	990.42	187.14	803.28
	Particle [m] (mg/L)	93.58	$[m]_e = f(t)$	92.46
	Total particle mass (g)	92.68	1.97	74.28
$[m]_i$ =200 mg/L	Hydraulic loading	22.35 L/m^2-min		
	Elapsed time t_e	136 hours		
	Initial hydraulic conductivity, k_i	3.24×10^{-2} cm/s		
	Final hydraulic conductivity, k_f	5.58×10^{-5} cm/s		
	Strained particles	16.8598 g		
	Surface straining rate	2306.37 g/m^2		
		Influent	**Effluent**	**Overflow**
	Total Volume V (L)	689.71	102.24	587.47
	Particle [m] (mg/L)	190.76	$[m]_e = f(t)$	189.87
	Total particle mass (g)	131.5686	1.5155	111.5860

q_0: initial infiltration rate (mL/s);
$[m]_i$: influent particle loading concentration;
$[m]_e$: effluent particle concentration, which declined with time during filtration;
b: first-order exponential rate constant for effluent particle concentration profile.
Mass balance errors associated with each of these experimental run were less than 10%.

Temporal profiles for influent, effluent and overflow are illustrated in Figure 4-2. The influent loading was kept constant within a range of 21 to 22 L/m^2-min, the effluent flow rate declined with time while the overflow rate correspondingly increased. The hydraulic volumetric balance error was less than 1% for all experimental runs.

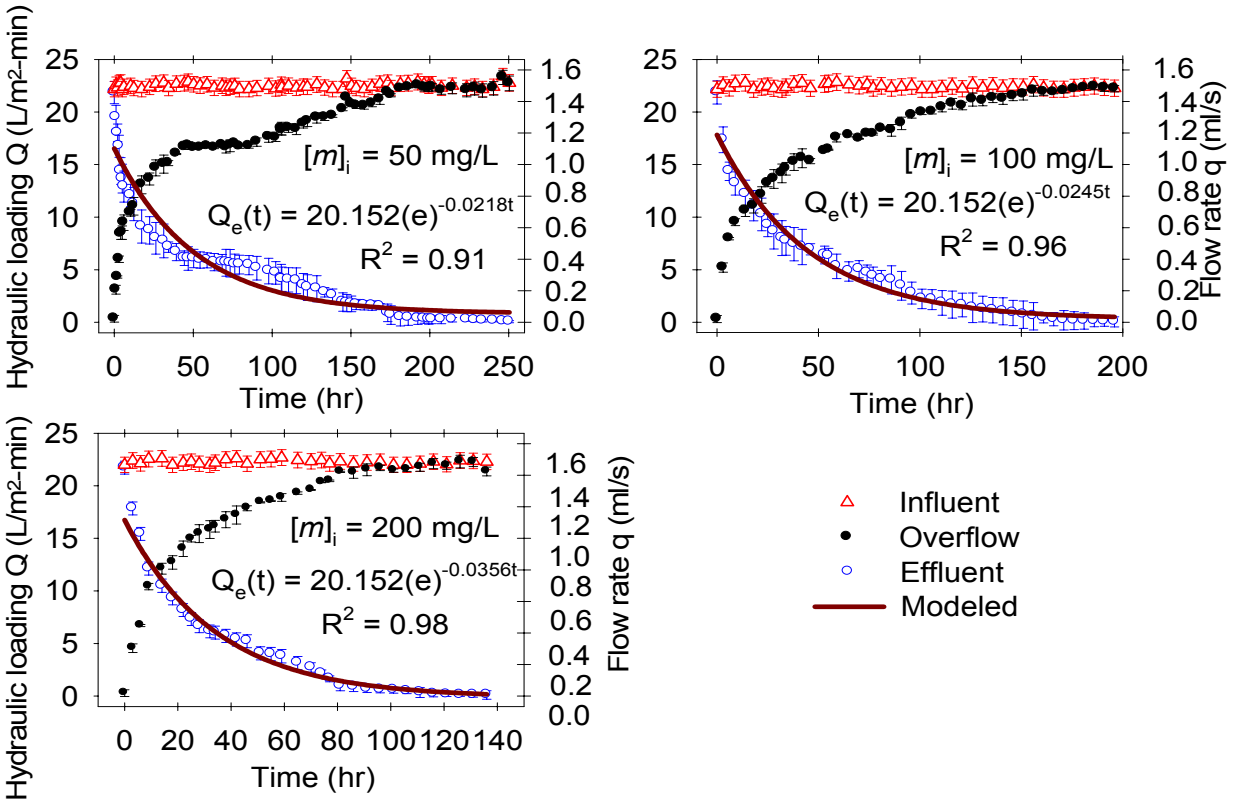

Figure 4-2 Hydraulic loading balance with particle loading. Influent hydraulic loading was kept constant. Effluent was modeled by exponential decay models as $Q_e(t) = Q_{e0} \cdot (e)^{-b \cdot t}$ with $R^2 > 0.91$. In this expression, Q_{e0} is the original infiltrate rate of a specimen, and equals to 21.152 L/m^2-min; b is the regression coefficient, equals to 0.0218, 0.0245 and 0.0356 with $[m]_i$ = 50, 100 and 200 mg/L, correspondingly.

4.5.1 Temporal Hydraulic Conductivity and Flow Rate Balance

Figure 4-3 illustrates the temporal hydraulic conductivity mean profiles with measured standard deviations, *k(t)*, during the filtration period with different particle concentration loading $[m]_i$. Results indicate that for higher particle loadings that hydraulic conductivity decreased more

rapidly. Results indicate that when $[m]_i$ = 50 mg/L, approximately 250 hours of loading were required for k to drop off from 3×10^{-2} to lower than 10^{-4}, while when $[m]_i$ = 200 mg/L, approximately 136 hours were required for k to drop to lower than 10^{-4}. When combined with hydrology, granulometry and mass loadings for a given location such results could be employed to predict hydraulic conductivity profiles and maintenance schedules to provide an acceptable infiltration rate.

A first-order exponential model simulated profiles of *k(t)* for all experiments.

$$k(t) = k_0 \cdot (e)^{-b \cdot t} \tag{4-11}$$

In this expression, k_0 is the original hydraulic conductivity, and the parameter b is a first-order rate constant (1/hour) determined from linear regression.

Figure 4-3 shows that the lower the loading concentration, the smaller the rate constant. The coefficient of determination, R^2 between measured and modeled hydraulic conductivity profiles exceeded 0.91 for all experimental runs. With a constant hydraulic gradient, i, and since $k(t) = q_e(t)/(A \cdot i)$, it was hypothesized that the effluent flow rate $q_e(t)$ should also follow the exponential decay model.

$$q_e(t) = A \cdot i \cdot k_0 (e)^{-b \cdot t} = q_0 \cdot (e)^{-b \cdot t} \tag{4-12}$$

In this expression, A is specimen cross-sectional area (L^2); q_0 is the original volumetric infiltration rate (L^3/T), and equals to 1.38 mL/s in this study. From (4-12), it is possible to estimate the total infiltration volume, V_w (m^3/m^2) during any period of t_e.

$$V_w = \frac{1}{A} \int_0^{te} q(t).dt \tag{4-13}$$

When k declines from 3.15×10^{-2} cm/s to less than 10^{-4} cm/s, the total infiltration volume (V_w) is 74, 50, and 27 m^3/m^2 with $[m]_i$ = 50, 100 and 200 mg/L, respectively.

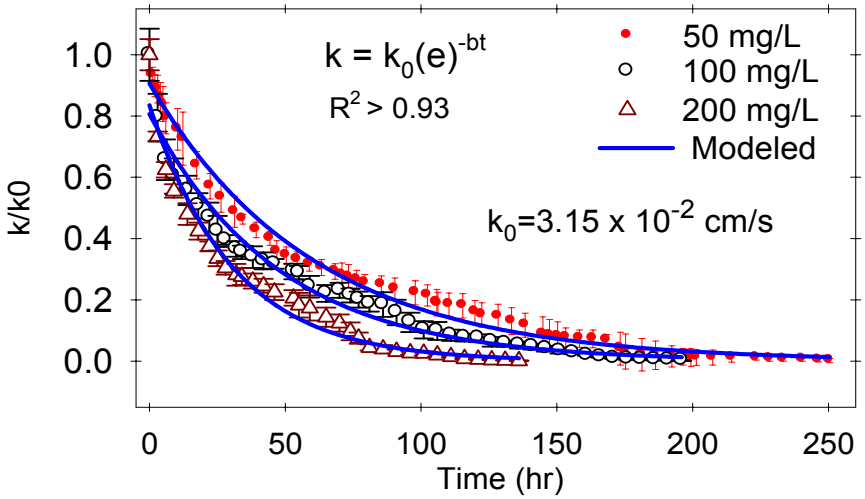

Figure 4-3 CPP hydraulic conductivity as a function of loading time. The influent hydraulic loading was held constant as 21.152 L/m2-min. The hydraulic head was maintained at approximately 1 cm above the CPP surface. The measured temporal hydraulic conductivity profile was modeled by a first-order exponential model of the form $k(t) = k_0 \cdot (e)^{-b \cdot t}$ with $R^2 > 0.91$. In this expression, k_0 is the initial hydraulic conductivity of the specimen, and equals to 3.150×10^{-2} cm/s. b is the first-order rate constant of 0.0218, 0.0245 and 0.0356 for $[m]_i$ = 50, 100 and 200 [mg/L], respectively.

4.5.2 Particle Mass Balance and Particle Removal Efficiency for each Size Fraction

Particles in influent, overflow, effluent and strained on CPP surface were measured and sieved, as illustrated in Table 4-2. Mass balance error for all experimental runs was less than 10%. Figure 4-4 illustrates the measured mean particle gradations and standard deviations for influent, overflow and effluent under different loading of 50, 100, and 200 mg/L, respectively.

Results from Figure 4-4 demonstrate that particles in effluent were relatively fine, more than 94% of them are finer than 100 μm, while filtered/strained particles are coarser, with only 60% of particles finer than 100 μm. Overflow gradation was very similar to the influent gradation. Measurement results also showed that overflow concentration, $[m]_o$, was constant and very close to influent concentration $[m]_i$.

Table 4-2 Particle mass balance in influent, effluent, overflow and entrained

Loading Particles	Particle Size	Particle mass (g)				
		influent	Effluent	Overflow	Entrained	
mg/L	μm				Meas.	Cal.
50 mg/L	1000	0.0000	0.0000	0.0000	0.0000	0.0000
	600	1.8705	0.0000	1.1652	0.6674	0.7052
	300	3.1926	0.0316	2.3201	0.7862	0.8408
	150	11.7041	0.1073	8.1048	3.1978	3.4920
	106	9.6508	0.1970	7.0043	2.2628	2.4495
	75	9.3462	0.2875	6.7581	2.2265	2.3006
	53	8.2130	0.3413	5.9911	1.7438	1.8805
	38	7.2869	0.4134	5.3161	1.4623	1.5574
	25	6.5070	0.4329	4.7393	1.1995	1.3348
	<25	3.1560	0.3379	2.2904	0.5068	0.5277
	Sum	60.9269	2.1489	43.6894	14.0531	15.0886
	Mass balance error ε (%)				6.86	
100 mg/L	1000	0.0000	0.0000	0.0000	0.0000	0.0000
	600	3.0678	0.0000	2.0658	0.8546	1.0020
	300	4.9771	0.0168	3.3867	1.4027	1.5736
	150	17.8323	0.0896	14.4488	3.1830	3.2939
	106	14.5328	0.1342	11.8300	2.3068	2.5686
	75	14.5791	0.2364	11.7686	2.1670	2.5741
	53	12.7347	0.3347	10.3092	1.9462	2.0908
	38	9.7503	0.3350	8.8864	1.5662	0.5289
	25	9.8893	0.4222	7.7242	1.3664	1.7429
	<25	5.3200	0.4014	3.8644	0.4439	1.0542
	Sum	92.6836	1.9703	74.2841	15.2368	16.4292
	Mass balance error ε (%)				7.26	
200 mg/L	1000	0.0000	0.0000	0.0000	0.0000	0.0000
	600	4.2628	0.0000	3.3984	0.8836	0.8644
	300	6.1179	0.0014	5.1617	0.8642	0.9548
	150	25.0243	0.0251	21.1447	3.4565	3.8545
	106	20.3010	0.1876	17.3678	2.5182	2.7456
	75	21.0773	0.2268	17.9472	2.7648	2.9033
	53	18.2617	0.2315	15.6047	2.1761	2.4255
	38	15.3146	0.2765	13.0126	1.7795	2.0255
	25	14.0515	0.3125	11.8946	1.6423	1.8444
	<25	7.1573	0.2541	6.0543	0.7746	0.8489
	Sum	131.5686	1.5155	111.5860	16.8598	18.4671
	Balance error ε (%)				8.70	

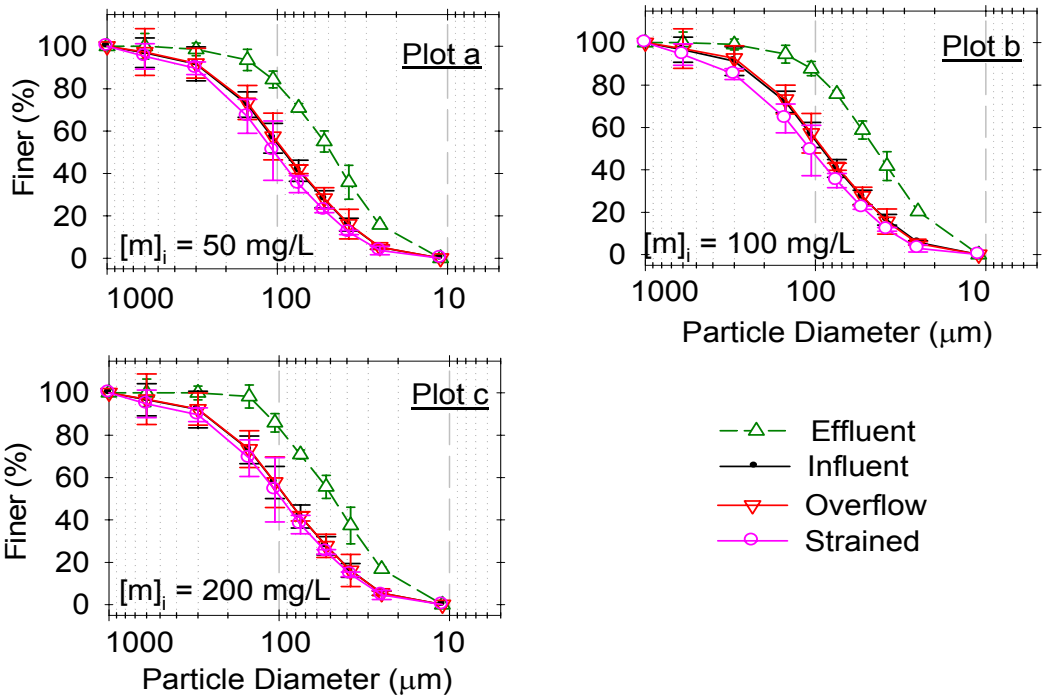

Figure 4-4 Particle size gradations for influent, effluent, overflow and particles strained by the CPP. Plot (a) compares the measured influent particle size gradation as compared to the targeted influent gradation. Plot (b), (c), and (d) are gradations for influent, effluent, overflow and surface strained particles under different particle loading concentration of 50, 100, and 200 mg/L, respectively. Gradations for influent and overflow are nearly identical.

Since both $[m]_o$ and $[m]_i$ were nearly constant during filtration, effective influent particle loading $[m]_{ie}$, can be calculated.

$$[m]_{ie} = \frac{([m]_i \cdot V_i - [m]_o V_o)}{V_e} \tag{4-14}$$

In this expression, V_e is total effluent volume. Effective particle mass loading (M_{ie}) on the CPP surface within elapsed time, t_e is $M_{ie} = [m]_{ie} \times V_e$.

Based on sieve analysis results, particle removal efficiency of each size fraction under different particle loading concentration of 50, 100 and 200 mg/L determined, was illustrated in Table 4-3 and Figure 4-5. Results from the table and figure illustrate that removal efficiency of coarser particles is higher than that of finer particles under a fixed concentration loading. With

$[m]_i$ = 50 mg/L, particle remove efficiency (η) for those finer than 25 μm is 50%, while for those coarser than 100 μm, η is as high as 90%. For those particles coarser than 300 μm, removal efficiency was nearly 100%, namely no particles coarser than 300 μm infiltrated through CPP specimens.

For each particle size fraction, removal efficiency increased with the higher loading concentration, resulting a total removal efficiency of 92.21% when $[m]_i$ = 200 mg/L, compared to 88.74% and 83.76% with $[m]_{i0}$ = 100 and 50 mg/L, respectively. Another finding is that more fine particles were strained on the CPP surface with higher particle concentration loading. The thicker inorganic schmutzdecke formed at higher concentration loading, resulted in more particles strained on CPP surface forming a progressively thicker schmutzdecke helping to prevent finer particles infiltrating into the CPP specimens. However, this increased efficiency came at the expense of more rapid reductions in hydraulic conductivity.

Table 4-3 Particle removal efficiency for different size fractions

Sieve Size (μm)	Particle loading concentration $[m]_i$ (mg/L)								
	50			100			200		
	M_{ie} (g)	M_e (g)	η (%)	M_{ie} (g)	M_e (g)	η (%)	M_{ie} (g)	M_e (g)	η (%)
1000	0.0000	0.0000		0.0000	0.0000	100.00	0.0000	0.0000	
600	0.4062	0.0000	100.00	0.5792	0.0000	100.00	0.6304	0.0000	100.00
300	0.6933	0.0286	95.87	0.9397	0.0168	98.21	0.9048	0.0014	99.85
150	2.5415	0.1113	95.55	3.3669	0.0896	97.34	3.7008	0.0251	99.32
106	2.0956	0.1970	90.60	2.7439	0.1342	95.11	3.0023	0.1876	95.75
75	2.0295	0.2875	85.83	2.7527	0.2364	91.41	3.1171	0.2268	92.72
53	1.7834	0.3413	80.86	2.4044	0.3347	86.08	2.7007	0.2315	91.43
38	1.5823	0.4134	73.87	1.8409	0.3350	81.80	2.2649	0.2765	87.79
25	1.4130	0.4329	69.37	1.8672	0.4222	77.39	2.0781	0.3125	84.96
<25	0.6853	0.3379	50.69	1.0045	0.4014	60.04	1.0585	0.2541	75.99
Total	13.2300	2.1489	83.76	17.4995	1.9703	88.74	19.4575	1.5155	92.21

M_{ie}: effective influent particles, g;
Me: effluent particles, g;
η: removal efficiency, $\eta = (1 - M_e / M_{ie}) \times 100\%$

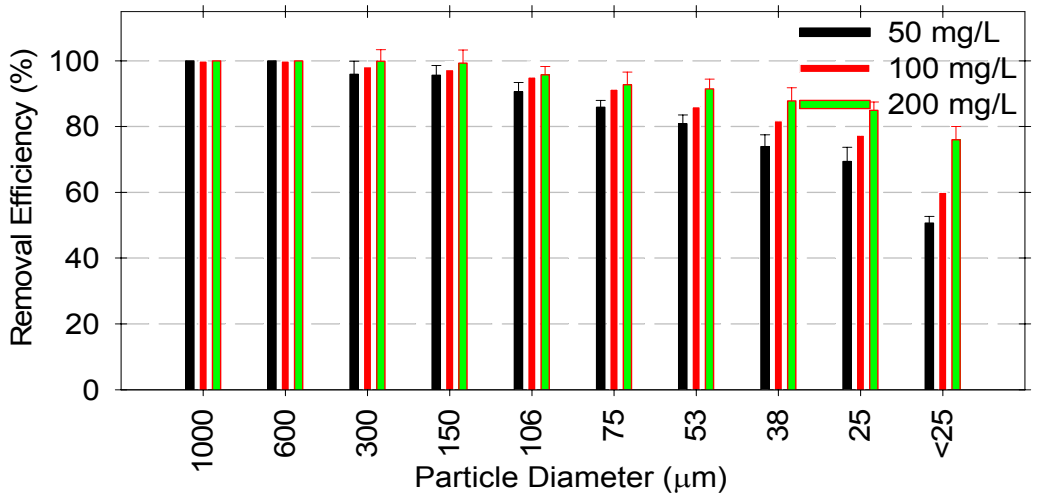

Figure 4-5 CPP particle removal efficiency for particle size fractions across the influent particle size gradation. For a same size fraction, removal efficiency increases with increasing loading concentration for the same influent gradation.

4.5.3 Strained Particles on CPP Surface

A schmutzdecke was formed on each tested CPP specimen, even at 50 mg/L. It was found that the thickness of the schmutzdecke on all CPP surface was about 1.5-1.8 mm at a point in time when the hydraulic conductivity dropped down to less than 10^{-4} cm/s, indicating that the schmutzdecke itself was a significant factor in clogging. Strained particle mass and gradation were illustrated in Table 4-2 and Figure 4-4. With known particle concentration of $[m]_i$, $[m]_o$, and $[m]_e(t)$, as illustrated in the plot *a* of Figure 4-6, and known flow rate of q_i, $q_o(t)$ and $q_e(t)$, as illustrated in Figure 4-2, strained particles during any period could be determined through application of equation (4-7). Plot *b* of Figure 4-6 illustrates results of cumulative strained particles for each concentration. Effluent concentrations in the plot *a* were modeled by a first-order exponential model.

$$[m]_e = [m]_0 + a \cdot (e)^{-bt} \tag{4-15}$$

In this expression, the parameter $[m]_0$, a, and b depend on influent particle gradation and concentration. When influent loading $[m]_i$ = 50 mg/L, $[m]_0$ = 4.07 mg/L, a = 13.58 mg/L and b = -0.0365 hour^{-1}; when $[m]_i$ = 100 mg/L, $[m]_0$ = 3.69 mg/L, a = 35.28 mg/L and b = -0.071 hour^{-1}; when $[m]_i$ = 200 mg/L, $[m]_0$ = 3.47 mg/L, a = 49.59 mg/L and b = -0.0861 hour^{-1}.

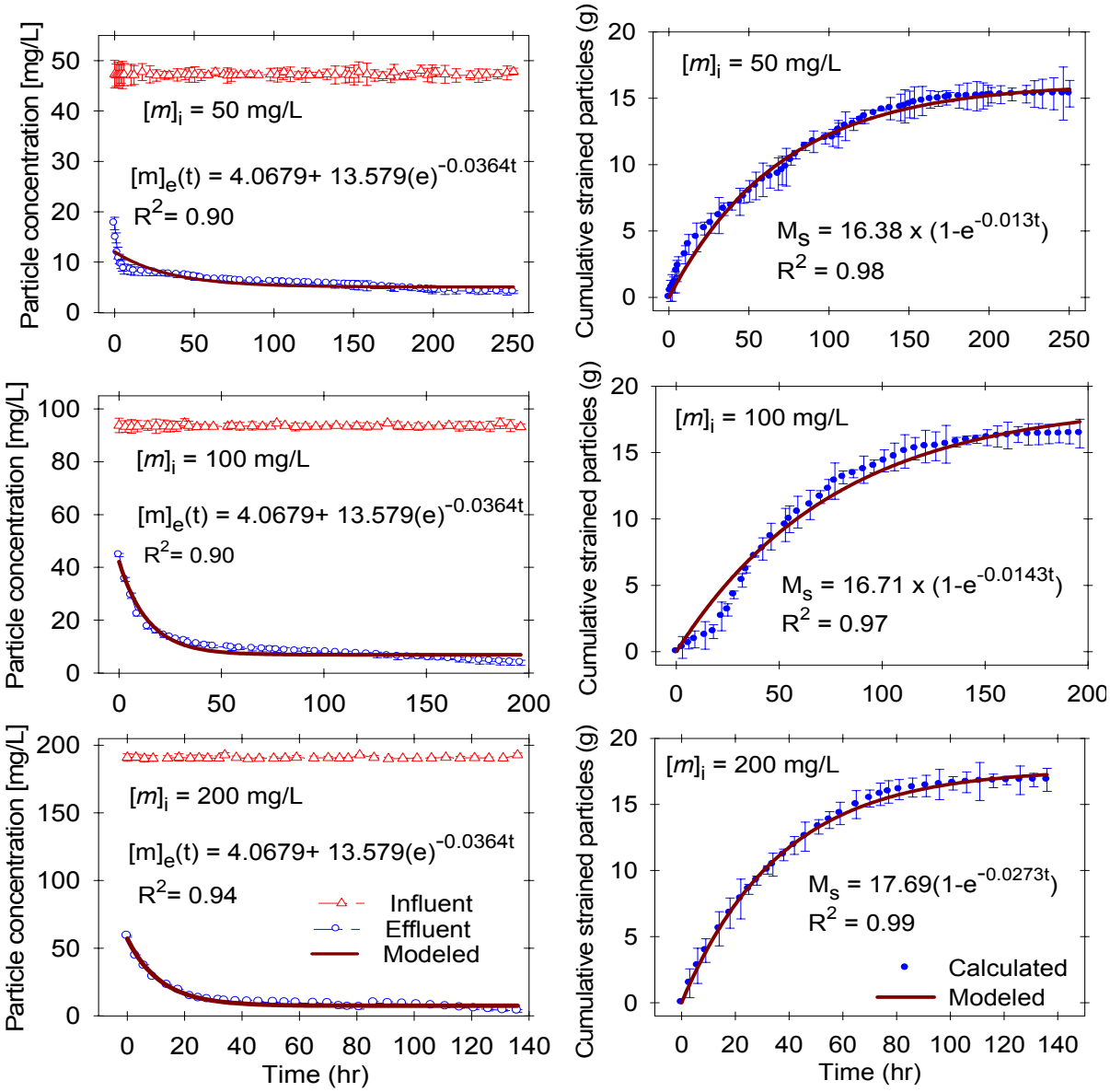

a . Temporal particle concentration profiles b. Cumulative particle straining profiles

Figure 4-6 Calculation mechanism of strained particles on CPP surface based on equation (4-7) with know particle concentration and flow rate of influent, effluent and overflow.

Based on results from (4-7), strained particle mass during the filtration period illustrated in the plot *b* of Figure 4-6 were modeled through a power law function.

$$M_s = \alpha(1 - e^{-\beta t}) \tag{4-16}$$

In this expression, α and β were determined by loading particle concentration. α = 16.38, 16.71 and 17.69 (mg), respectively, with $[m]_i$ = 50, 100 and 200 mg/L, while β = -0.013, -0.0143 and -0.0273 ($hour^{-1}$), respectively, with the corresponding loading concentration.

4.5.4 Particle Breakthrough from CPP

Figure 4-7 illustrates the ratio of the number of particles in effluent $[N]_e$ to that in influent $[N]_i$.

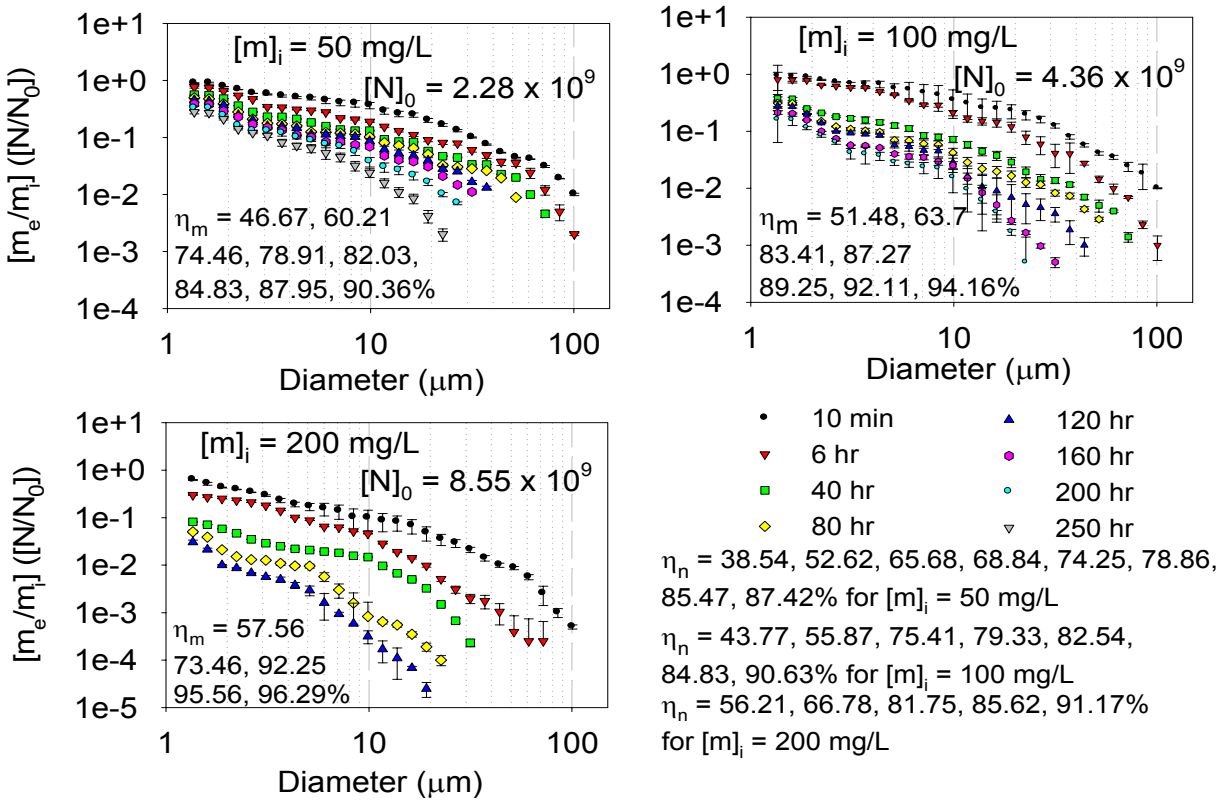

Figure 4-7 [TSS] removal efficiency at different time based on PSD analysis. [N] and $[N_0]$ are particle number concentration in effluent and influent (count/L), respectively. $[m]_i$ is particle mass concentration in influent. η_n and η_m are removal efficiency based on mass and number, respectively, calculated based on equation (4-5) and (4-6).

It was found that particle removal efficiency increased with higher loading particle concentration. When $[m]_i$ = 50 mg/L, β_m = 46.67% and 87.95% after 10 minutes and 200 hours of filtration, respectively. When $[m]_i$ = 100 mg/L, β_m = 51.48% and 94.16% after 10 minutes and 200 hours of filtration, respectively. When $[m]_i$ = 200 mg/L, however, β_m = 57.56% and 98.29% after 10 minutes and 130 hours of filtration, respectively. Based on PSD analysis for influent and effluent samples, particle mass concentration removal efficiencies based on mass and number are also illustrated in Figure 4-7.

After 3 hours of filtration, no particles coarser than 100 μm were measured in the effluent; after 6 hours, no particles coarser than 75 μm measured in the effluent; after 80 hours, no particles coarser than 50 μm measured in the effluent, while at the end of each filtration test when k dropped off lower than 10^{-4} cm/s, no particle coarser than 25 μm were measured in the effluent.

4.5.5 Turbidity and SSC

Since influent concentration was kept constant, influent turbidity remained nearly constant. For effluent, however, with more and more particles strained, particulate mass concentration in effluent decreased with time, resulting in a decrease of effluent turbidity. Turbidities for influent and effluent are illustrated in Figure 4-8. Results indicate that the turbidity at the end of each experimental run decreased to approximately 4 NTU for all influent particle loadings of 50, 100 and 200 mg/L.

Comparing the results of turbidity and suspended solid concentration (SSC) from PSD analysis, a correlation between those two parameters for effluent was found, as illustrated in Figure 4-9. A power law was employed hereby to model the relationship.

$$SSC\,[mg/L] = 0.3678 \times [\tau]^{1.4051} \tag{4-17}$$

In the above expression, τ is turbidity (NTU), and SSC is in mg/L. Through this model, for the given gradation, particle mass concentration can be obtained from measured turbidity.

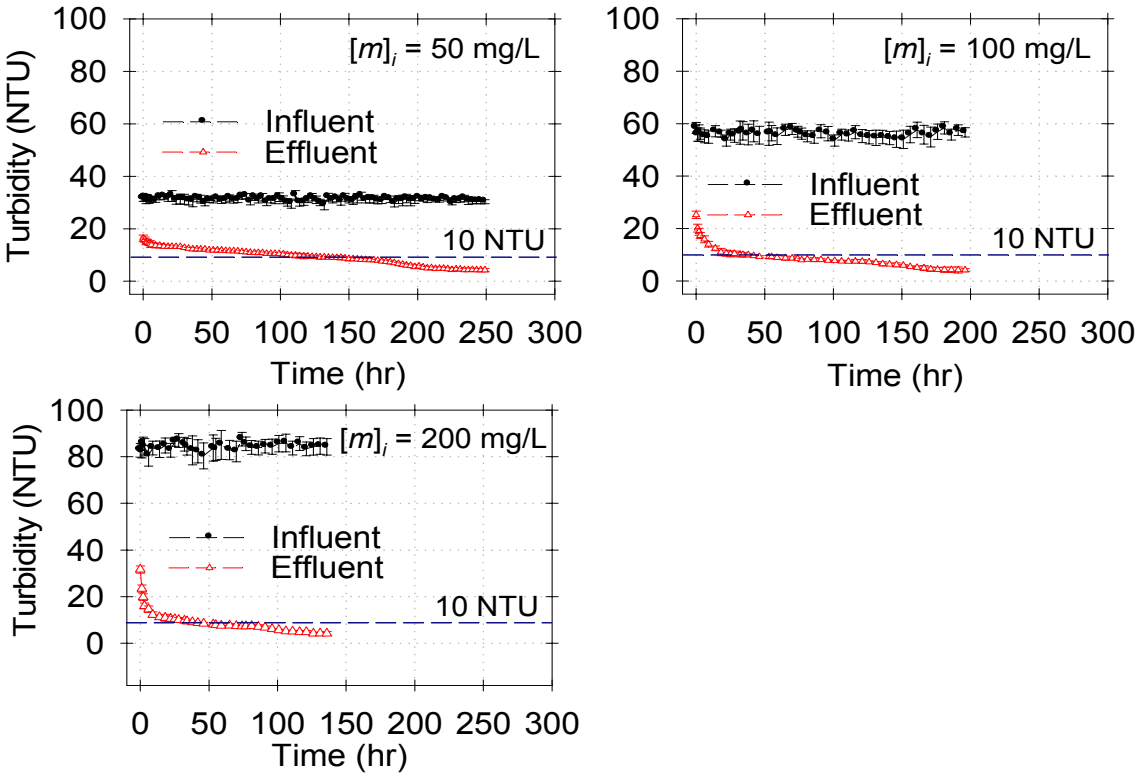

Figure 4-8 Turbidity in influent and effluent for different particle loading concentration

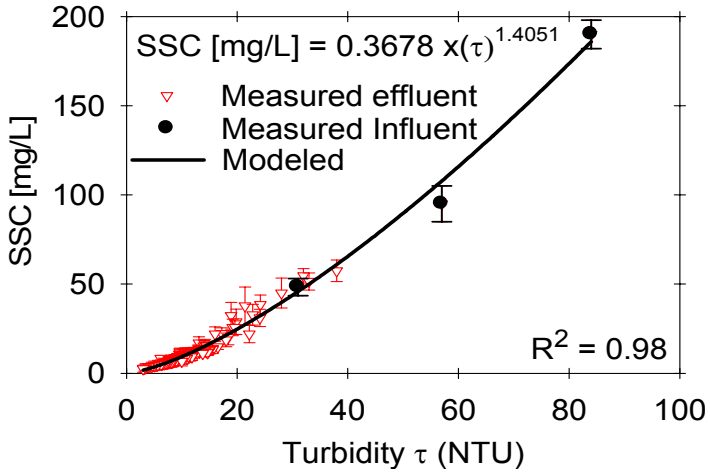

Figure 4-9 Relationship between effluent turbidity and SSC. The relationship between turbidity (τ) and particle mass concentration as SSC was modeled by a power law model.

4.5.6 Hydraulic Backup by Surface Vacuuming and Sonicating-Backwash Cleaning

With a schmutzdecke formed on each CPP surface and hydraulic conductivity reduced to less than 10^{-4} cm/s two cleaning methods were examined. Three of the clogged specimens were cleaned by a sonicating/backwash method as described, while the other 3 specimens were cleaned by a vacuuming method. Hydraulic conductivity then was measured for each cleaned specimens. It was found that the sonicating/backwash method and the vacuum method recovered the hydraulic conductivity to more than 96% of k_0. Figure 4-10 illustrates these results for recovered hydraulic conductivity after cleaning. It was found that, for a given influent particle gradation, the loading concentration (50, 100 or 200 mg/L) had little influence on the effectiveness of vacuum or backwashing cleaning method. However, it should be identified that at present, a sonicating/backwash method is not yet a well-developed methodology in practice. In reality, it is very hard to backwash the pavement. The vacuum method provides an effective and practical method for permeable pavement cleaning.

4.5.7 Estimation of Cleaning Schedule for CPP Maintenance

The evaluation of surface cleaning and the measurement of temporal hydraulic conductivity established a foundation for surface cleaning schedule estimation. An example of a typical cleaning schedule for a location is illustrated. Assume this location has a typical runoff particle concentration of 100 mg/L of the particle size gradation specified in this study and CPP characteristics. This location has an average dry period of 4 days and a runoff duration that is 3 hours for each runoff event. This results in a total annual loading time of 274 hours. Based on the experimental measurements, it will take 156 hours for CPP to drop its k to lower than 10^{-3} cm/s under the particle loading concentration of 100 mg/L. Using equation (4-10), the maintainence period would be $156/274 \approx 0.57$ year.

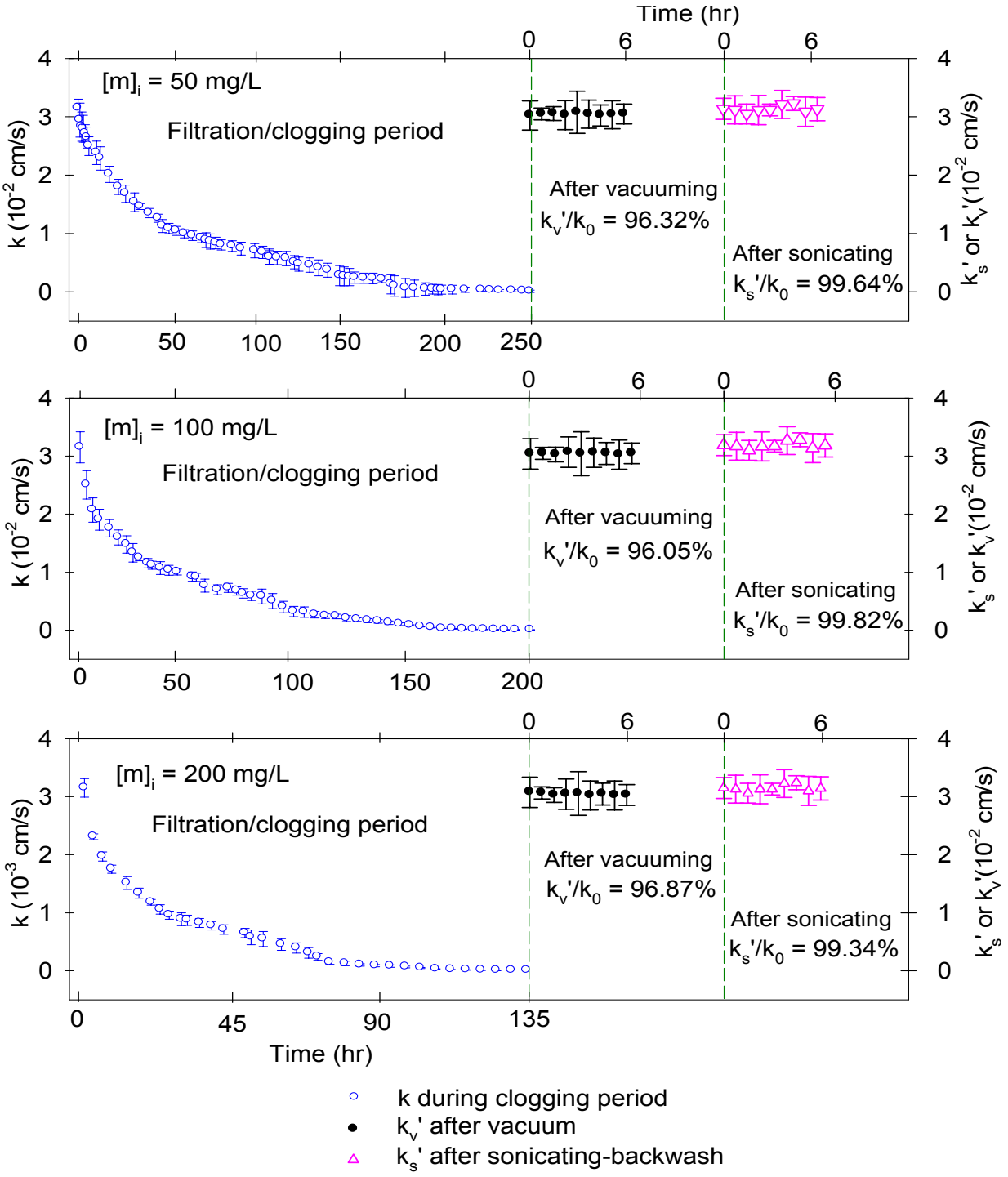

Figure 4-10 these plots show the hydraulic conductivity (k) of clogged CPP materials could be recovered up to 96% by vacuum cleaning method, and 99% by sonicating-backwashing method. It was found that, for a given influent particle gradation, the loading concentration (50, 100 or 200 mg/L) had little influence on the effectiveness of vacuum or backwashing cleaning method.

4.6 SUMMARY AND CONCLUSIONS

Based on the experimental measurements and modeling, the filtration and clogging behavior of permeable pavement (cementitious permeable pavement, CPP) were examined. This behavior was examined for 6 specimens recovered from an in-situ CPP slabs that served as the infiltrating and filtration interface during a period of 3 years for a partial exfiltration reactor (PER) in Cincinnati, OH.

CPP particle removal efficiency illustrated a dependence on loading concentration. For the given loading gradation, designated a sandy silt on a textural basis, when $[m]_{i0}$ = 200 mg/L, η_m = 92.21%; when $[m]_{i0}$ = 100 mg/L, η_m = 88.74% and η_m = 83.76% for $[m]_{i0}$ = 50 mg/L, respectively. For particles coarser than 300 μm, removal efficiency, η was 100% and there was no particle breakthrough, while for those particles finer than 25 μm, η was approximately 50%.

Particle mass concentration in effluent was measured and predicted by a first-order exponential model for each particle loading concentration. Based on this model, the particle mass concentration in the effluent after infiltrating through CPP could be estimated. The first-order rate constant, whether for CPP effluent mass concentration or CPP hydraulic conductivity was a function of particle gradation (held constant), CPP pore properties (held constant and uniform for all specimens), loaded particle properties including gradation (held constant) and influent concentration, and CPP pore characteristics, such as effective porosity, pore size distribution, and specific surface area. From experimental measurements, when schumutzdecke thickness was more than 1.5 mm on the CPP surface, the infiltration rate of CPP dropped to less than 10^{-4} cm/s for the given gradation and hydraulic loading.

A methodology was developed to determine the particle mass strained on the CPP surface during any filtration and clogging period. The methodology for strained particle estimation as

well as the temporal hydraulic conductivity model provides a foundation for prediction of the CPP clogging potential and for determination of a CPP cleaning schedule.

The sonicating/ backwash cleaning method recovered up to 99% of the CPP hydraulic conductivity, while the vacuuming method recovered 96%. At an event mean loading of 100 mg/L particle mass loading for the tested gradation, the CPP surface could be cleaned once every 6 months by vacuuming to restore infiltration capacity.

Turbidity was measured before and after runoff infiltrating through CPP. It was found that the effluent turbidity was significantly reduced. The CPP produced an effluent turbidity of less than 10 NTU after 20 hours of filtration with a final turbidity of 4 NTUs at the end of each run. A turbidity-TSS relationship was developed based on experimental measurements. A power law model was employed to describe this correlation.

4.7 NOTATION

The following symbols are used in this Chapter.

$[M_{tss}]$ = mass concentration of total solids suspension (M/L^3);

$[N_j]_i$ = particle number concentration for each particle size fraction in influent ($/L^{3)}$;

$[N_j]_e$ = particle number concentration for each particle size fraction in effluent ($/L^3$);

$[N]_i$ = total number concentration in influent ($/L^3$);

$[N]_e$ = total number concentration in effluent ($/L^3$);

$[m]_{i0}$ = designed influent particle concentration (mg/L).

$[m]_i$ = influent particle concentration (M/L^3);

$[m]_e$ = effluent particle concentration (M/L^3);

$[m]_o$ = particle concentration in overflow (M/L^3);

A = specimen cross-sectional area (L^2);

M_e = total particles in effluent (M);

M_i = total particle loaded on the CPP surface (M);

M_o = total particles in overflow (M);

M_s = total particles strained on CPP surface (M);

T_{ur} = turbidity (NTU);

TSS = total solid suspension;

V_d = the volume of deposited materials (L^3);

V_e = total effluent volume (L^3);

V_i = volume of the influent samples (L^3);

V_T = the total volume of the specimen (L^3);

a, b = coefficient of the model predicting the effluent mass concentration;

d_g = diameter of the spherical collector (L);

d_j = diameter of each particle size fraction (M)

d_m = media diameter to

d_p = suspended particles size

k = hydraulic conductivity (cm/s);

k_0 = average initial permeability;

m_i = the mass obtained from influent samples (mg)

m_e = the mass obtained from effluent samples (mg)

p = the cleaning period (T);

q_e = effluent flow rate (L^3/T);

q_i = influent flow rate (L^3/T);

q_0 = original infiltration rate (L^3/T);

q_o = overflow flow rate (L^3/T);

t_c = average runoff concentration time (T);

t_e = test period of filtration (T);

x = average drying days (T)

α and β = coefficient of the model predicting the strained particles on the CPP surface;

η = particle removal efficiency (%)

ϕ_t = total porosity (%);

σ = specific deposit.

4.8 REFERENCES

ASTM D1889-00, 2005, "America Standard Test Method for Turbidity of Water". *ASTM International-2005*.

ASTM D421-85(2002), 2002, "Standard Practice for Dry Preparation of Soil Samples for Particle-Size Analysis and Determination of Soil Constants", *ASTM International* 10-Nov-2002.

ASTM D422-63(2002), 2002, "Standard Test Method for Particle-Size Analysis of Soils", *ASTM International 10-Nov-2002*.

Andersen, C. T. and I. D. L. Foster, 1999, "The role of urban surfaces (permeable pavements) in regulating drainage and evaporation: development." *Hydrol. Proc*. 13, pp. 597-609.

Aulenbach, D.B. and Y.Y. Chan, 1988, "Heavy meal removal in a rapid infiltration sand column", *Particle. Sci. Tech*. 6, pp 467-481.

Backstrom, M. and A. Bergstrom, 2000, "Draining function of porous asphalt during snowmelt and temporary", *Journal of Civil Engineering,* 27, pp 594-598.

Balades, J-D., M. Legret and H. Madiec, 1995, "Permeable pavements: pollution management tools." *Wat. Sci. Tech*. Vol. 32, No. 1, pp. 49-56.

Brattebo, B., O. Derek and B. Booth, 2003, "Long-term stormwater quantity and quality performance of permeable pavement systems." *Water Research*, 37, pp. 4369-4376.

Colandini, V., M. Legret, and J. D. Balades, 1995, "Metallic pollution in clogging materials of urban porous pavements." *Wat. Sci. Tech*., Vol. 32, No. 1, pp. 57-62.

Elimelech, M. and C.R. O'Melia, 1990, "Kinetics of deposition of colloidal particles in porous media", *Environ. Sci. Tech*. 24, pp 1528-1536.

Fach, Dipl.-Ing. S., W.F. Geiger, C. Dierkes, 2002, "Development of an assessment procedure for permeable pavements." University of Essen, *Urban Water Management*, 15, 45141 Essen, Germany, pp. 1-12.

Field, R. , H. Masters and M. Singer, 1982, "Status of porous pavement research." *Water Res*. Vol. 16, pp. 849-858.

Field, R, H. Masters, and M. Singer, 1982, "Porous pavement: research; development; and demonstration", Trans. Eng. J. of ASCE, Vol. 108, No. TE3. pp. 244- 258.

Fujita, S., 1993, "Infiltration in congested urban areas of Tokyo", Proc. 6th Int. Conf. on Urban Storm Drainage, Vol. 1, pp993-998.

Fwa, T. F., Tan S. A., and Y. K. Guwe, 1999, "Laboratory evaluation fo clogging potential of porous asphalt mixtures." *J. Tran. Eng., ASCE*, pp. 43-49.

Hogland, W., J. Niemczynowicz, and T. Wahlman, 1987, "The unit superstructure during the constructive period." *Sci. Total Environ.*, 59, pp. 411-424.

Isenring, T. H. Koster, and I. Scazziga, 1990, "Experience with porous asphalt in Switzerland." *Transportation Research Record 1265*, pp. 41-53.

Jackson, T. J., and R. M. Ragan, 1974, "Journal of the hydraulics division." *Journal of the Hydraulics Division*, ASCE, pp. 1739-1752.

Jahangir, I., 1998, "Rainwater and its infiltration importance in Iran." *Pro., 3rd Int. Conf. on Innovative Technologies in Urban Storm Drainage*, Vol. 2, pp 475-485.

Jimenez, F.E.P. and M.A.C. Perez, 1990, "Analysis and evaluation of the performance of porous asphalt: the Spanish experience." *Surface Characteristics of Roadway: International Research and Technologies*, ASTM STP 1031, W. E. Meyer and J. Reichert, Eds., American Society for Testing and Materials, PA, pp. 512-527.

Legret, M. , M. Nicollet, P. Miloda, V. Colandini, and G. Raimbault, 1999, "Simulation of heavy metal pollution from stormwater infiltration through a porous pavement with reservoir structure." *Wat, Sci. Tech*. 39(2), pp. 119-125.

Legret, M. and V. Colandini, 1999, "Effects of a porous pavement with reservoir structure on runoff water: water quality and fate of heavy metals." *Wat. Sci. Tech*. 39(2), pp. 111-117.

McDowell-Boyer, L. M., J. R. Hunt, and N. Sitar, 1986, "Particle transport through porous media." *Water Resour. Res*., Vol. 22, pp. 1901-1921.

Moghadasi, J., M. Jamialahmadi, H. Müller-Steinhagen and A.O. Sharif, 2004, "Theoretical and experimental study of particle movement and deposition in porous media during water injection", *Journal of Petroleum Science and Engineering*, 43, pp 163– 181

Niemczynowicz, J., and W. Hogland, 1987, "Tests of porous pavements perforated in Lund, Sweden." *Proc., 22nd AIRH Congress-IAHR and 4th Int. Conf. on Urban Storm Drainage*, pp. 79-80.

Ojha, C. S. P. and N. J. D. Graham, 1992, "Appropriate use of deep-bed filtration models." *Journal of Environment Engineering*, *ASCE*, 118(6), pp. 964-980.

O'Melia C. R., 1985, "Particle pretreatment and performance in water filtration", *Journal of Environmental Engineering, ASCE*, 111, 874-890.

Pagotto, C. , M. Legret, and P. LE Cloirec, 2000, "Comparison of the hydraulic behavior and the quality of highway runoff water according to the type of pavement." *Wat. Res*. 34(18), pp. 4446-4454.

Park, S. B. and M. Tia, 2004, "An experimental study on the water-purification properties of the porous concrete." *Cement and Concrete Research*, Vol. 34, pp. 177-184.

Rajapakse, J.P. and K.J Ives, 1990, "Pre-filtration of very highly turbid waters using pebble matrix filtration." *Journal of IWEM*, 4(2), 140-147.

Sansalone, J.J. and Buchberger, S.G., "Partitioning and first flush of metals in urban storm water", *ASCE J. of Environmental Engineering*, Vol. 123, No. 2, pp. 134-143, February 1997.

Sansalone, J. J., 1999, "Adsorptive infiltration of metals in urban drainage-media characteristics." *The Science of the Total Environment*, 235, pp. 179-188.

Sansalone, J. J., 1999, "In-sity performance of a passive treatment system for metal source control." *Wat. Sci. Tech*. 39(2), pp.193-200.

Sansalone, J.J., Koran, J.M., Smithson, J.A., and Buchberger, S.G. (1998). "Physical characteristics of urban roadway solids transported during rain events." *J. Environ. Eng*., 124(5), 427-440.

Sansalone, J.J. and Glenn, D.W., 2002, "Accretion and partitioning of pollutants associated with urban traffic activities in roadway snow – Part I", *ASCE J. of Environmental Engineering*, Vol. 128, No.2, pp. 151-166.

Sansalone, J.J. and Glenn, D.W., 2003, "Physical and Chemical Characteristics of Urban

Roadway Snow Residuals Generated from Traffic Activities", *J. of Water, Air and Soil Pollution*, Vol. 148, (1-4), pp. 46-61.

Sansalone, J.J. and Z. Teng, 2004. "In-situ storm water treatment and recharge through infiltration: Quality and Quantity Attenuation", *ASCE J. of Environmental Engineering*, 130(9), 990-1007.

Sansalone, J.J. and Z. Teng, 2005, "Transient Rainfall-Runoff Loadings to a Partial Exfiltration System: Implications for Water Quantity and Quality", *ASCE J. of Environmental Engineering*, 131(8), pp. 1155-1167.

Sansalone, J.J and Cristina, C.M., "Gradation-Based Heavy Metal Mass Prediction Utilizing Granulometry of Urban Land Use Snowmelt Particulate Residuals", *ASCE J. of Environmental Engineering*, 130(12)

Schluter, W. C. Jefferies, 2002, "Modelling the outflow from a porous pavement." *Urban Water*, 4, pp. 245-253.

Seki, K. and T. Miyazaki, 2001, "A mathematical model for biological clogging of uniform porous media." *Water Resources Research*, 37, pp. 2995-2999.

Stevenson, D. G., 1997, "Flow and filtration through granular media-the effect of grain and particle size dispersion." *Wat. Res*. 31(2), pp. 310-332.

Stotz, G. and K. Krauth, 1994, "The pollution of effluents from pervious pavement of an experimental highway section: first results." *The Science of the Total Environment*, 146/147, pp. 465-470.

Tan, S.-A., T.-F. Fwa, and C.-T. Han, 2003, "Clogging evaluation of permeable bases." *Journal of Transportation Engineering*, 129(3), pp. 309-315.

Teng, Z. and J.J. Sansalons, 2004, "In situ partial exfiltration of rainfall runoff. II: particle separation", *Journal of Environmental Engineering*, *ASCE*, 130(9), pp 1-13.

Tobiason, J.E. and B. Vigneswaran, 1994, "Evaluation of a modified model for deep bed filtration." *Wat. Res*. 28(2), pp. 335-342.

Xu, D., A. Mermoud, 2003, "Modeling the soil water balance based on time-dependent hydraulic conductivity under different tillage practices." *Agricultural Water Management*, 63, pp. 139-151.

Xi, Y. and Z. P. Bazant, 1999, "Modeling chloride penetration in saturated concrete." *Journal of Materials in Civil Engineering*, 11(1), pp. 58-65.

Yao K. M., M. T. Habibian and C. R. O'Melia, 1971, "Water and wastewater filtration: concepts and applications". *Environ. Sci. Tech*. 5, 1105-1112.

Yu, S. L., 1993, "Stormwater management for transportation facilities." National Cooperative Highway Research Program, Synthesis of Highway Practice, *Transportation Research Board*, Washington, D. C.

CHAPTER 5 RUNOFF pH, ALKALINITY ELEVATION AND PHOSPHORUS REMOVAL OF CPP

5.1 INTRODUCTION

There has been a significant shift from interest solely in water quantity issues, such as flood defense and water supply, towards to a more balanced concern for both quantity and quality aspects with the water environment (Pratt 1999). Compared to asphalt porous pavement, CPP has its outstanding advantages for environmental benefits (Fach et al. 2002). CPP can not only control the quantity of runoff as asphalt porous pavement does by reducing the peak flow rate and volume of runoff, it also has the capability to control the quality of runoff by removing particulate matters, metals, mineral oils, soluble and anthropogenic pollutants from runoff (Balades et al. 1995; Field 1982; Stotz and Kruth 1994; Teng and Sansalone 2004), and neutralize watershed acid by elevation of alkalinity and pH values in runoff (Fach et al. 2002; Li et al. 1999; Park and Tia 2004; Pratt 1999). For example, Fach et al. (2002) presented that CPP was a suitable method to ensure the retention of heavy metals, the acid neutralization, and phosphorus (P) and nitrogen (N) removal. Regarding the risk that heavy metals are available for infiltration into groundwater because of acidic conditions, the final-pH-value of CPP is above the critical-pH value of 6.5 (Fach et al 2002). The retention capacity of CPP for copper is up to 90%, and the retention capacity for mineral oil type hydrocarbons (MOH) is higher than 99% (Fach et al 2002; Balades et al. 1995; Stotz and Krauth 1994). Park and Tia (2004) presented that total phosphorus (TP) removal efficiency is up to 66% (14 days) to 96% (7 days) for fresh made CPP.

Many particles with a diameter less than 60 μm absorb several pollutants, such as mineral oil type hydrocarbons (MOH), polycyclic aromatic hydrocarbons (PAH), phosphorus, nitrogen or heavy metals (Colandini et al. 1995; Fach et al. 2002). In-situ partial exfiltration reactor (PER) has been developed combining the advantage of cementitious porous pavement, infiltration

trenches and engineered filtration. In which CPP functions as initial control preventing solids from entering the PER (Teng and Sansalone, 2004).

5.2 OBJECTIVES

This chapter focuses on CPP functions as a reactive and absorptive material for acid neutralization and phosphorus removal from stormwater. The first objective is to measure the pH elevation characteristics of CPP. The second objective is to measure the alkalinity elevation properties of CPP. The third objective is to evaluate the phosphorus removal properties of CPP, including TP, TDP and TPP removal efficiency. The last objective is to investigate the relationship of removed total solids suspension (TSS) and total particulate phosphorus (TPP).

5.3 BACKGROUND

5.3.1 Role of Alkalinity and pH Elevation

Alkalinity is the concentration of bases dissolved in water and expressed as parts per million (ppm) or milligrams per litre (mg/L) as calcium carbonate ($CaCO_3$). These bases are usually bicarbonates (HCO_3^-) and carbonates (CO_3^{2-}), and, of high pH, hydroxide (OH^-) ions. The following chemical equilibrium equations show the relationships among the three kinds of alkalinity. Total alkalinity is the sum of all three kinds of alkalinity.

$$CO_2 + H_2O <===> H_2CO_3 <===> H^+ + HCO_3^- <===> CO_3^{2-} \quad (5\text{-}1)$$

With the urban development, more and more acidic pollutants flow to watersheds and deteriorate our water environment. The main acidic source comes from industry process and urban activity (Zivica and Bajza 2001). The presence of alkalinity neutralizes acids and alkalinity is added to water as a buffer. For example, in waters with low alkalinity, pH might fluctuate from 5 or lower to as high as 9 or above; while in high alkalinity waters, pH might fluctuate from about 7.5 to 8.5. Alkalinity levels of 20-200 mg/L are typical of fresh water. A total alkalinity

level of 100-200 mg/L will stabilize the pH level in a stream. Levels below 20 mg/L indicate that the system is poorly buffered, and is very susceptible to changes in pH from natural and human-caused sources. Above pH 9.5 (usually well above pH 10), OH^- alkalinity can exist or CO_3^{2-} and OH- alkalinities can coexist together.

5.3.2 Role of Phosphors Removal

The excess release of phosphorus into surface water is of an increasingly environmental concern. Extended phosphorus (P) have been input to rivers, lakes and oceans and other small size water bodies from over-fertilization of urban and right-of-way areas, industrial and municipal sources (such as detergents) (Spivakov et al. 1999; Teng et al. 2004). Because it is an essential nutrient for growth of organisms, phosphorus is a major cause of eutrophication in most ecosystems, subsequently followed by massive algal blooms, fish suffocation and other undesired effects (Spivakov et al. 1999). The critical concentration of P above which the growth of algae and other aqueous plants accelerates, is suggested as 0.01 mg/L for dissolved P and 0.02 mg/L for total P (Kim et al. 2003). Phosphorus in the elemental form is particularly toxic and is subject to bioaccumulation in much the same way as mercury (Spivakov et al. 1999). In comparison, dissolved P off I-10 of City Park in Baton Rouge can be as high as 1.0 mg/L and total P can be as high as 3.0 mg/L as an event mean concentration (EMC).

Phosphorus in natural waters is divided into two component parts: dissolved phosphorus (DP) and particulate phosphorus (PP) (Rigler 1973), and the sum of DP and PP is termed total phosphorus (TP). Dissolved and particulate phosphorus are differentiated by whether or not they pass through a 0.45 micron membrane filter (Carlson and Simpson 1996). It was found 60-80% of phosphorus in road runoff to be associated with particulates (Hvitved-Jacobsen et al. 1994).

Phosphorus removal from wastewater has been widely investigated (Teng and Sansalone 2004). Phosphorus removal from stormwater is either adsorption or precipitation.

One of the important advantages of CPP over asphalt permeable pavement (APP) is the capability to elevate rainfall-runoff alkalinity, which neutralizes acids in rainfall-runoff, allows metal elements to precipitate in the PER, because partitioning varies as a result of runoff pH and alkalinity (Teng and Sansalone 2004), and reduces metal toxicity.

5.4 METHODOLOGY

5.4.1 Tested Specimens

Cored specimens were taken from CPP material constructed as the surface interface of a partial exfiltration reactor (PER) in Cincinnati, OH. The PER is a linearly-extended in-situ rainfall-runoff unit operation and process, as illustrated in Chapter 2. The pore characteristics, including total porosity ϕ_t, effective porosity ϕ_e, pore size distribution $(PSD)_{pore}$, specific surface area of $(SSA)_s$, $(SSA)_{pt}$, and$(SSA)_{pe}$, and tortuosity (L_e/L) were evaluated using X-ray tomography. Details of the examination and results of pore characteristics are also illustrated in Chapter 2.

Totally 3 groups of specimens were employed in this chapter.

Group I: 3 specimens taken from the PER surface, and exposed to rainfall-runoff for 3 years, (mean suspended solids ≈ 200 mg/L, total porosity ≈ 25%);

Group II: 3 specimens taken from the PER surface, and exposed to rainfall-runoff for 3 years, coated with aluminum, (total porosity ≈ 25%), and

Group III: 3 specimens taken from control CPP material at the site (urban Cincinnati, Ohio) exposed to only rain for 3 years (mean suspended solids < 1 mg/L, total porosity ≈ 21%).

5.4.2 Aluminum Coating

The 3 specimens of the Group II were coated with aluminum. Specimens were dip into aluminum nitrate ($ALNO_3$) solution with concentration of 2 [mol], and were sonicated for 30 minutes and then were dried in hot room with 40°C.

5.4.3 Influent Profile

Influent runoff was collected from the site off I-10 at the Lake Park in Baton Rouge, LA. The initial alkalinity concentration is about 40 mg/L (in CaCO3), [P] is about 0.01 mg/L, and particle concentration about 60 mg/L. In order to simulate the typical condition of runoff happening in Baton Rouge, KH_2PO_3 was added so that [TDP] concentration of 1.0 mg/L, and [TP] of 1.45 mg/L were achieved. Influent runoff properties were listed in Table 5-1.

Table 5-1 Influent properties

pH_0	$[Alk]_0$ (mg/L)	$[TP]_0$ (mg/L)	$[TDP]_0$ (mg/L)	$[TPP]_0$ (mg/L)	$[m]_0$ (mg/L)	$[N]_0$ (count/L)
7.5-7.6	41.5-44.8	1.44-1.49	0.94-1.00	0.47-0.50	80	10×10^9

$[Alk]_0$: influent alkalinity concentration;
$[m]_0$: influent particle mass concentration;
$[N]_0$: influent particle number concentration.

5.4.4 Experimental Process

The same setup for hydraulic conductivity was used for soluble test, as illustrated in Chapter 3. Specimen sidewall was packed by waterproof gray tape to avoid boundary effects. During testing, influent water was pumped from the tank to infiltrate through the CPP specimen cylinder by a peristaltic pump (Masterflux 7520-40). Influent flow rates were controlled by regulating the speed of the peristaltic pump to keep an overflow during the whole test period, so that a certain constant head is maintained. In this study, hydraulic loading rate, Q, was

maintained constant of 31 L/m^2-min for group I specimens, for group II, Q = 30.2 L/m^2-min, and for group III, Q = 25.4 L/m^2-min.

Influent and effluent samples were collected in 45-minute interval, and a total of 9 groups of samples (influent and effluent) were collected for each specimen in each 6 hour duration event. 7 events were conducted for each specimen. Each 6 hour duration event was followed by 4 days of room temperature drying.

pH, alkalinity, total phosphorus (TP), total dissolved phosphorus (TDP) and particle size distribution (PSD) were measured for both influent and effluent samples.

5.4.5 pH Value Measurements

pH for both influent and effluent samples were measured according to ASTM D1293-99(2005) Standard Test Methods for pH of Water (2005). An Orion 190-A meter with a Silver/Silver Chloride (Ag/AgCl) combination electrode was used to measure pH. To ensure quality of data measurements, the probes were calibrated daily with fresh buffer. The pH of the buffer was measured before measuring the pH of the samples.

5.4.6 Alkalinity Measurement

Alkalinity in both influent and effluent were measured according to Test Method B-Color change titration of ASTM D1067-02 Standard Test Methods for Acidity or Alkalinity of Water (ASTM 2005). Influent and effluent samples were titrated to an end point of pH 4.5, using 0.02N sulfuric acid in a Class-A buret to determine alkalinity.

$$\text{Alkalinity, mg } CaCO_3/L = \frac{A \cdot N \cdot 50{,}000}{\text{mL sample}} \qquad (5\text{-}2)$$

In this expression, A is standard acid used in mL, and N = 0.02, normality of standard acid.

One blank of DI water was titrated per set of 20 replicate samples as quality control of the test procedure.

5.4.7 TP, TDP and TPP Measurement

To measured total dissolved phosphorus (TDP) in influent and effluent, the following 3 steps were followed. (1). Filtrate of samples through 0.45 μm membrane filter to removal particulate phosphorus bounded on the particles coarser than 0.45 μm; (2). Conduct acid digestion of samples using persulfate digestion method (PDM) described in Standard Methods (SMEWW, 1992), and (3). Measure TDP in samples using a colorimetric method, which means the color of treated sample reflects the concentration of the parameter.

The process of PDM is summarized as follows.

1) Fill 60 mL of thoroughly mixed sample to hot plate with volume mark lines;
2) Add 0.05 mL (1 drop) Phenolphthalein indicator aqueous solution;
3) Add 1 mL H_2SO_4 solution and 0.4 g solid $(NH_4)2S_2O_8$;
4) Boil gently on a preheated hot plate until a final volume of 10 mL is reached.
5) Cool, dilute to 30 mL with distilled water;
6) Add 0.05 mL (1 drop) Phenolphthalein indicator aqueous solution, and neutralize to a faint pink color with NaOH.
7) Make up to 60 mL with distilled water.
8) Determine phosphorus by colorimetric method. In this method, PhosVer 3 phosphate reagents made by Hach Company were utilized to indicate phosphorus concentration, and the Spectrophotometer (Hach DR/2000) was used to measure the phosphorus concentration.

The procedure of TP measurement follows the same steps as TDP except that no filtration step needed. As long as TP and TDP were measured, total particulate phosphorus (TPP) could be calculated as the follows.

$$[TPP] = [TP]-[TDP] \quad (5\text{-}3)$$

5.4.8 Particle Size Distribution (PSD)

The purpose of measuring PSD was to examine the P removal efficiency and PSD correlation. PSD was analyzed using LISST-potable particle analyzer (Sequoia Tech.) for suspended particles in both influent and effluent to determine particle volume concentration distribution, as illustrated in Chapter 4. All samples were sonicated before testing. Tests were duplicated to the validation of the instrument measurements.

PSD measures the volume of particles for each size fraction. Based on the volume, particle number and particle mass could be obtained through assuming specific gravity, as illustrated in Chapter 4. Total surface area (M^2) could be calculated as the follows.

$$SA = \sum 4\pi (D_i / 2)^2 \cdot n_i \quad (5\text{-}4)$$

In this expression, n_i is the particle number of each size fraction, and D_i is the particle diameter for each size fraction.

5.5 RESULTS AND DISCUSSION

5.5.1 pH Elevation after Infiltrating through CPP

Figure 5-1 illustrates pH elevation after infiltrating through CPP materials for all 7 events. With influent pH of 7.5, the first effluent flush of pH elevated to 8.62, 10.25, and 8.40 after infiltrating through specimens of Group I, II and III, respectively. During each 6 hour event, effluent pH decrease eventually with time. The effluent pH follows a similar decay trend for all 7 events, which could be modeled by an exponential decay model.

$$pH = pH_0 + a \cdot (e)^{-b \cdot t} \quad (5\text{-}5)$$

In this expression, pH_0 is determined by the influent $pH_0 = 7.5$ in this study. Coefficient *a* and *b* are determined by CPP chemical properties.

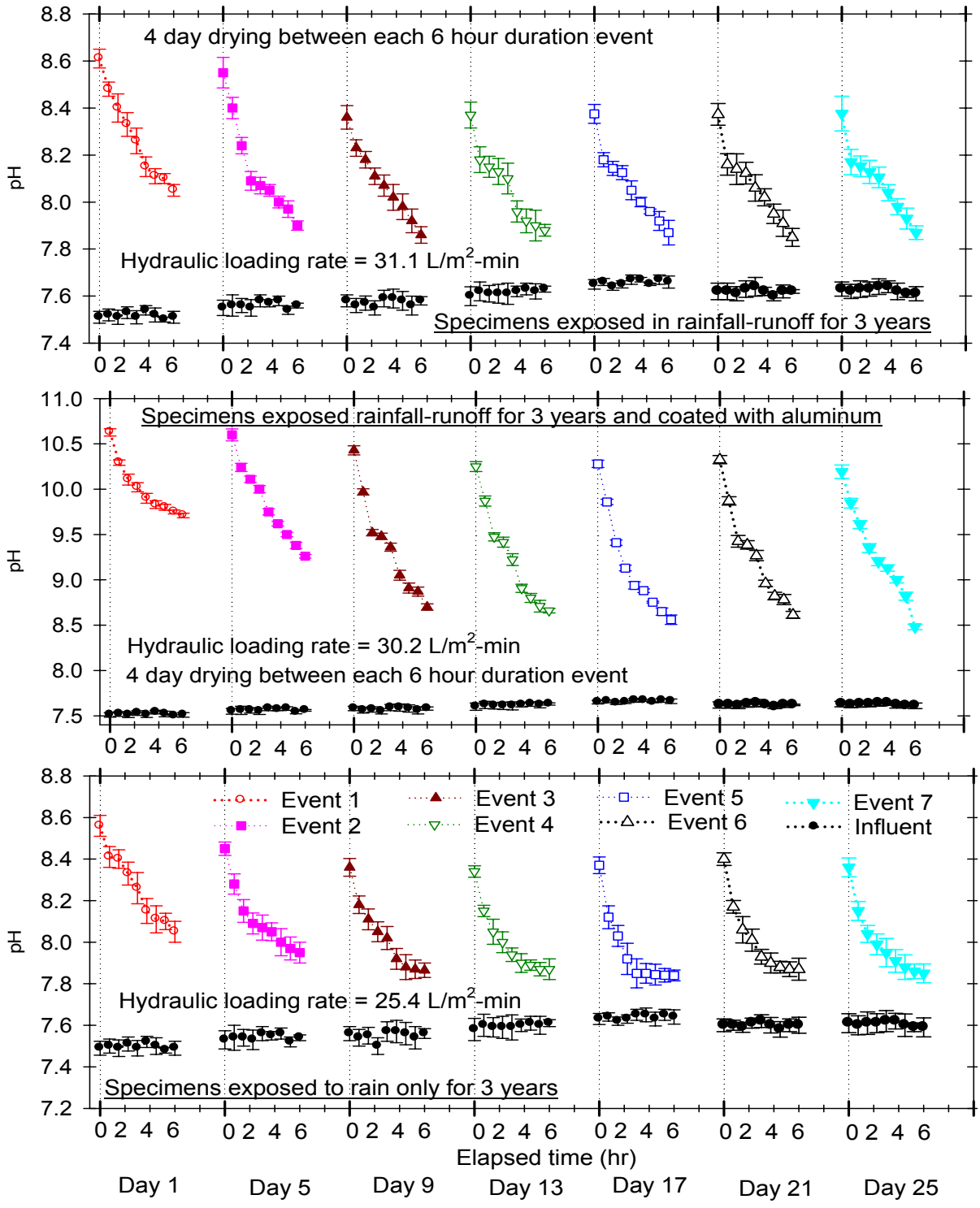

Figure 5-1 pH elevation properties of CPP materials. Influent pH value was kept constant in each event duration as 7.6.

As illustrated in Figure 5-2, for the three groups of specimens, $a = 0.78$, $b = 0.0041$ for Group I specimens; $a = 2.64$, $b = 0.0280$ for Group II specimens, and $a = 0.73$, $b = 0.0036$ for Group III specimens, respectively.

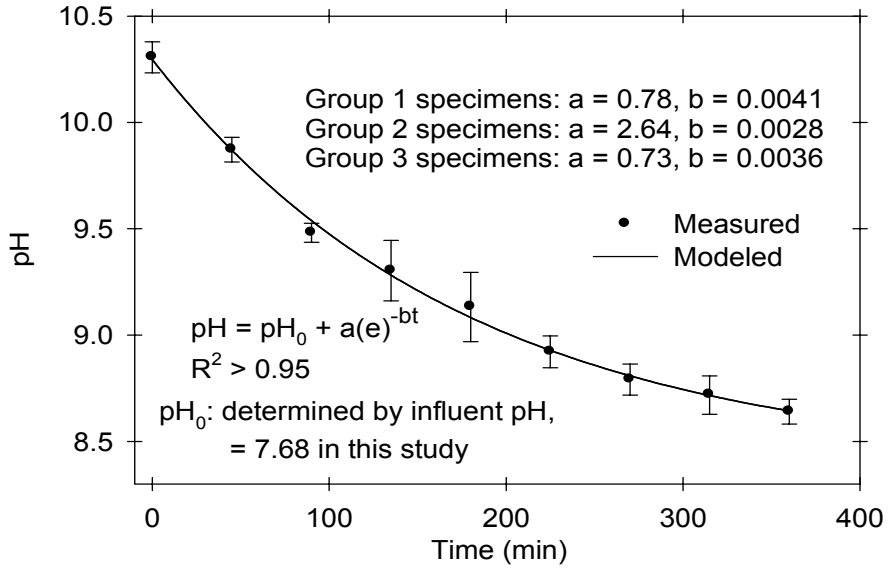

Figure 5-2 pH value after infiltration through CPP materials. Effluent pH values during 6 hour filtration were modeled by an exponential decay model as $pH = pH_0 + a(e)^{-b \cdot t}$ with $R^2 > 0.95$, in this expression, pH_0 was determined by influent pH value, and equaled to 7.68 in this study. For group I specimens exposed to rainfall-runoff for 3 years, parameters in the model $a = 0.78$, and $b = 0.0041$, for group II specimens coated with aluminum, $a = 2.64$, and $b = 0.0028$, while for group III specimens exposed to rain only for 3 years, $a = 0.73$, and $b = 0.0036$.

5.5.2 Alkalinity Elevation Properties of CPP

Alkalinities were elevated after infiltrating through CPP, showing the similar trend as pH value did. When influent alkalinity was about 44 mg/L, Group I specimens elevated alkalinity of 4.45-4.98 mg/L; Group II specimens elevated 25.87 mg/L, and Group III specimens elevated 10.22 mg/L. The average elevation rate for Group I was 11.6%, for group II 42.2% and Group III 14.5%. Figure 5-3 illustrates alkalinity elevation after infiltrating through CPP materials of all 7 events. During each 6-hour event, effluent alkalinity concentration decreased eventually with

time. The effluent alkalinity concentration follows a similar decay trend for all 7 events, which could be modeled by an exponential decay model.

$$[alk] = [alk]_0 + c \cdot (e)^{-d \cdot t} \tag{5-6}$$

In this expression, [alk] and $[alk]_0$ represent alkalinity concentration in effluent and influent. $[alk]_0$ was kept constant during each event , and equals to 41.2-44.5 mg/L in this study. Coefficient c and d are determined by CPP chemical properties. For the three groups of specimens, c = 8.91, d = 0.0189 for Group I specimens; c = 31.38, d = 0.005 for Group II specimens, and c = 15.91, d = 0.0076 for Group III specimens, respectively, as illustrated in Figure 5-5.

5.5.3 TDP Removal Efficiency of CPP

With influent $[TDP]_0$ = 1.0 mg/L, the average TDP removal efficiency of Group I was 24.2%. The [TDP] of the first flush effluent for Group I is about 0.6 mg/L, and the end [TDP] was about 0.8 mg/L after 6 hour running. For Group II coated with aluminum, the average [TDP] removal efficiency was as high as 82.3%; [TDP] of the first flush effluent of that group is only 0.06 mg/L, and the end [TDP] after 6 hour running was about 0.25 mg/L. For Group III exposed to rainfall only, the average [TDP] removal efficiency was about 28.6%; [TDP] of the first flush effluent of that group is about 0.6 mg/L, and the end [TDP] after 6 hour running was about 0.72 mg/L. Figure 5-4 shows [TDP] in both influent and effluent for all 7 events with 6 hour duration for each. It was found that the aluminum coated specimens had very high capacity to remove TDP. [TDP] in effluent could be modeled by an exponential model, as illustrated in Figure 5-7.

$$[TDP] = [TDP]_0 + p_0 (e)^{-\beta \cdot t} \tag{5-7}$$

In this expression, $[TDP]_0$ = 0.95-1.0 mg/L. For group I p_0 = 0.3004, and β = 0.0013; for group II, p_0 = 0.8792, and β = 0.0006, while for group III, p_0 = 0.2911, and β = 0.0006.

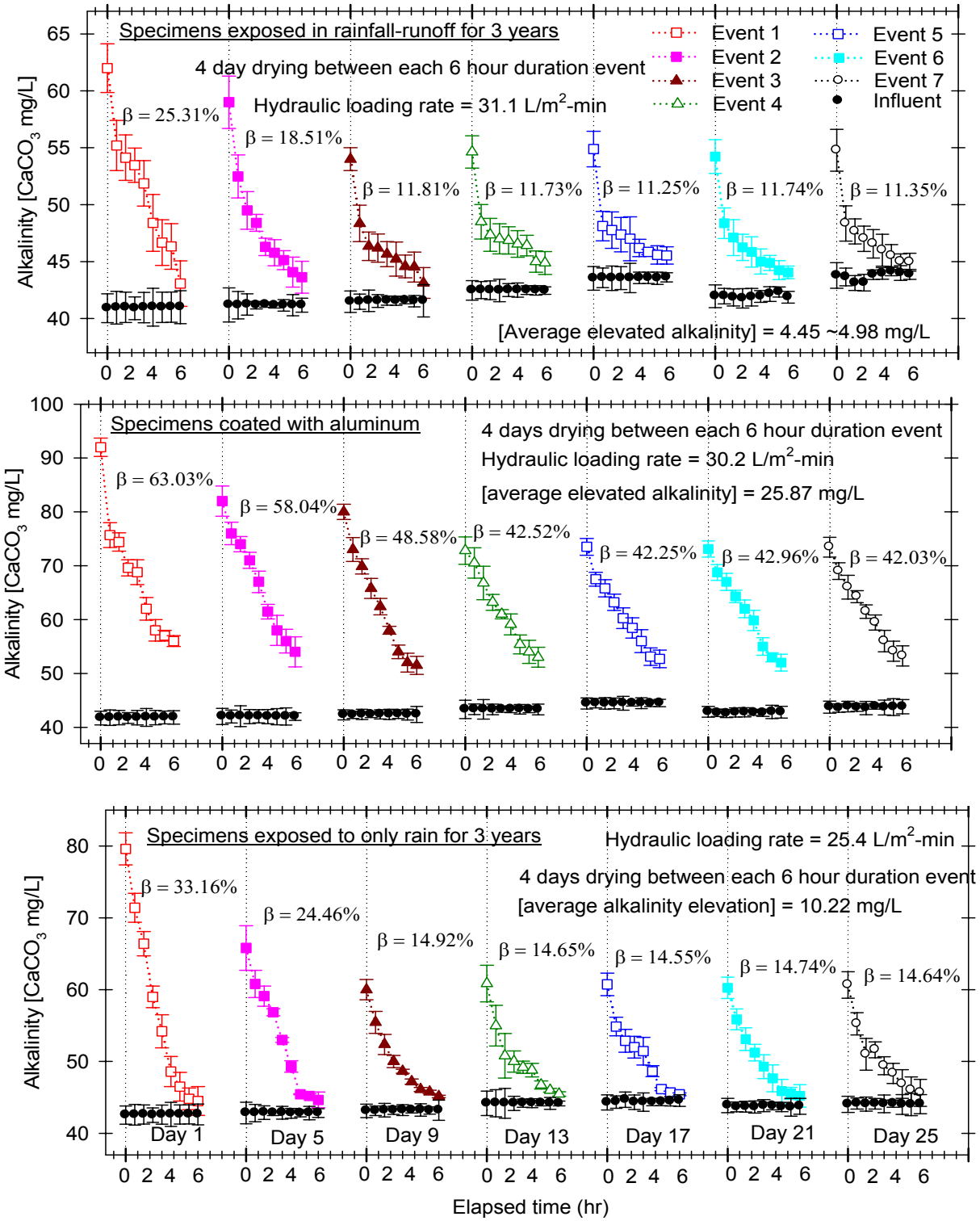

Figure 5-3 Alkalinity elevation properties of CPP specimens.

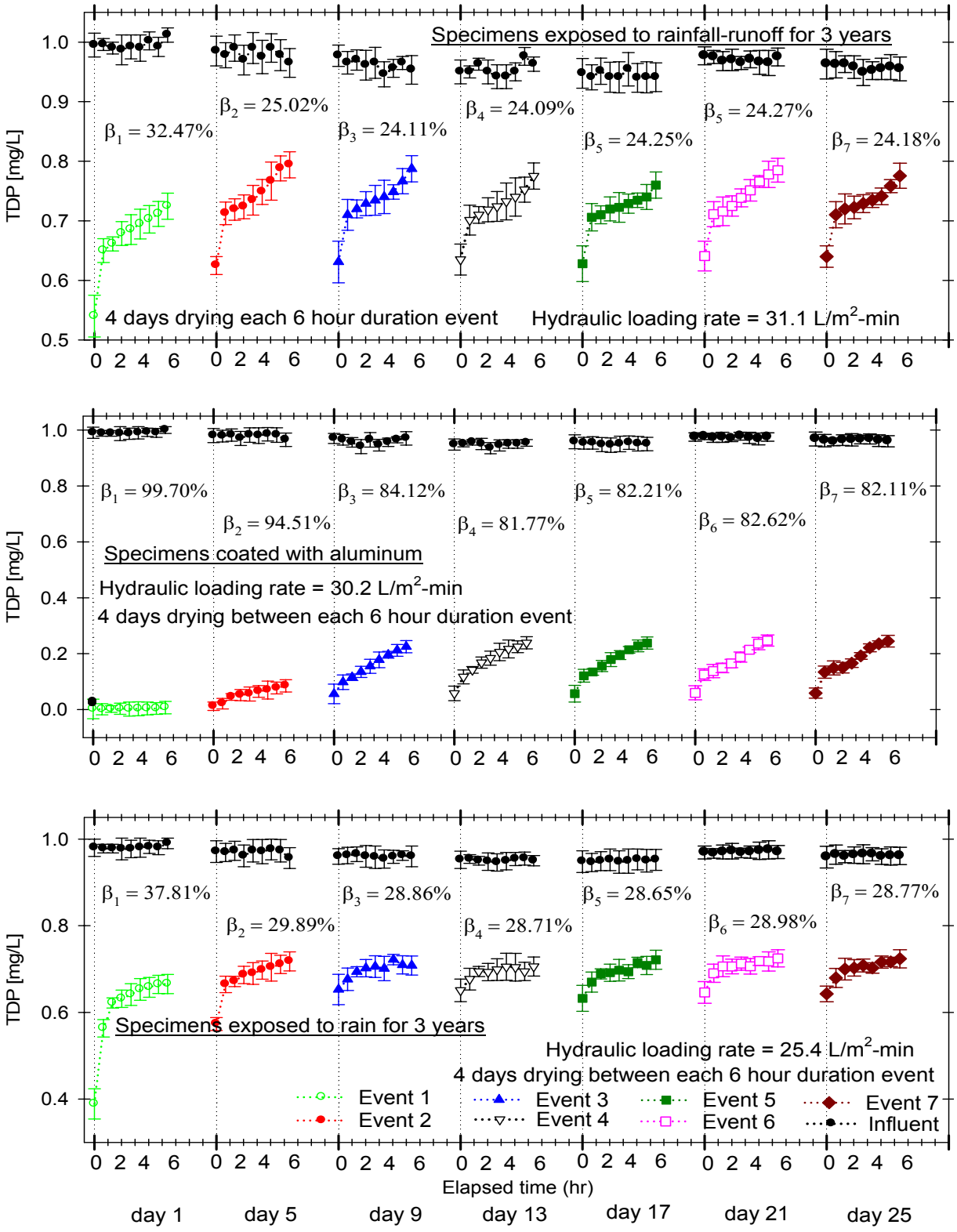

Figure 5-4 Total dissolved phosphorus (TDP) removal properties of CPP. Influent [TDP] was kept constant as 1.0 mg/L.

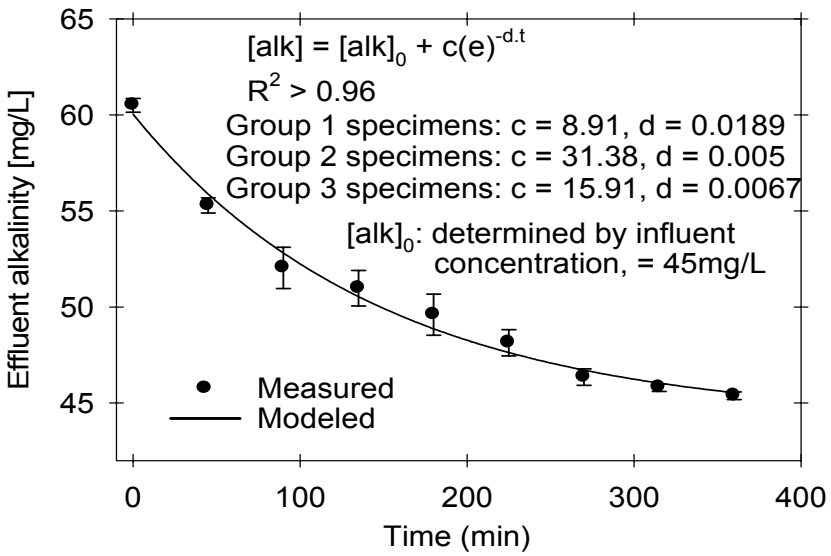

Figure 5-5 Alkalinity after infiltration through CPP materials. Effluent alkalinity concentrations during 6 hour filtration were modeled by an exponential decay model as $[alk] = [alk]_0 + c(e)^{-d \cdot t}$ with $R^2 > 0.96$, in this expression, $[alk]_0$ was determined by influent alkalinity concentration, and equaled to 45 mg/L in this study.

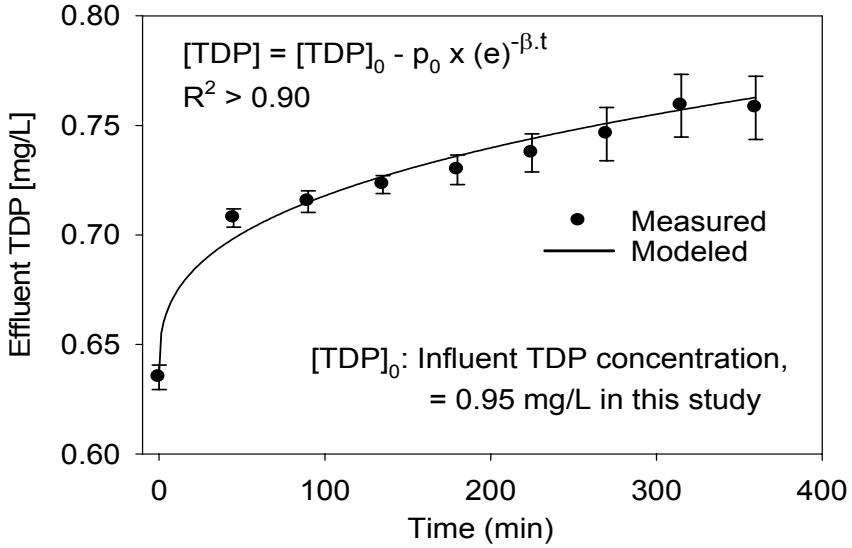

Figure 5-6 Effluent [TDP] after infiltration through CPP materials. Effluent [TDP] during 6 hour filtration were modeled by an power law model as $[TDP] = [TDP]_0 + p_0(e)^{-\beta \cdot t}$ with $R^2 > 0.91$, in this expression, $[TDP]_0$ is influent [TDP], and equals to 0.95-1.0 mg/L. For group I specimens exposed to rainfall-runoff for 3 years, $p_0 = 0.3004$, and $\beta = 0.0013$ with $R^2 = 0.90$; for group II specimens coated with aluminum, $p_0 = 0.8792$, and $\beta = 0.0006$ with $R^2 = 0.95$, while for group III specimens exposed to rain only for 3 years, $p_0 = 0.2911$, and $\beta = 0.0006$ with $R^2 = 0.91$.

5.5.4 TP Removal Efficiency of CPP

TP removal procedure was illustrated in Figure 5-7. With influent [TP] ≈ 1.45 mg/L, the average TP removal efficiency was 46%, 84% and 49% for Group I, II and III, respectively. For Group I and III specimens without coating, the effluent [TP] changed in a very narrow range of 0.78-0.82 mg/L. The reason is that [TDP] removal efficiency decreased eventually, while the [TPP] removal efficiency increased with time, leading to a relatively constant removal during each testing, as illustrated in Figure 5-8. Removed [TP] was the combination of [TDP] and [TPP].

For Group III, [TP] was as low as 0.1-0.28 mg/L, demonstrating that aluminum coated CPP has a very high capability for phosphorus removal. Figure 5-8 illustrates the removed [TP], [TDP] and [TPP]. Effluent [TPP] during 6 hour filtration were modeled by an exponential model, as Figure 5-9 illustrated.

$$[TPP] = [TPP]_0 - q_0(e)^{\alpha \cdot t} \tag{5-8}$$

In this expression, $[TPP]_0$ is the TPP concentration of influent, equals to 0.48 mg/L. Coefficient q_0 and α are determined by CPP chemical properties. For group I specimens exposed to rainfall-runoff for 3 years, q_0 = 0.3913, and α = 0.0005 with R^2 = 0.94; for group II specimens coated with aluminum, q_0 = 0.3911, and α = 0.0005 with R^2 = 0.94, while for group III specimens exposed to rain only for 3 years, q_0 = 0.4019, and α = 0.0005, with R^2 = 0.95. It was found that the coefficient of q_0 and α for the 3 groups of specimens are almost the same. The reason is that the TPP removal is mainly associated with the particle removal which is determined by the CPP pore characteristics. Since all three groups of specimens have the similar pore space geometry, the TPP removal efficiency demonstrates the same trend.

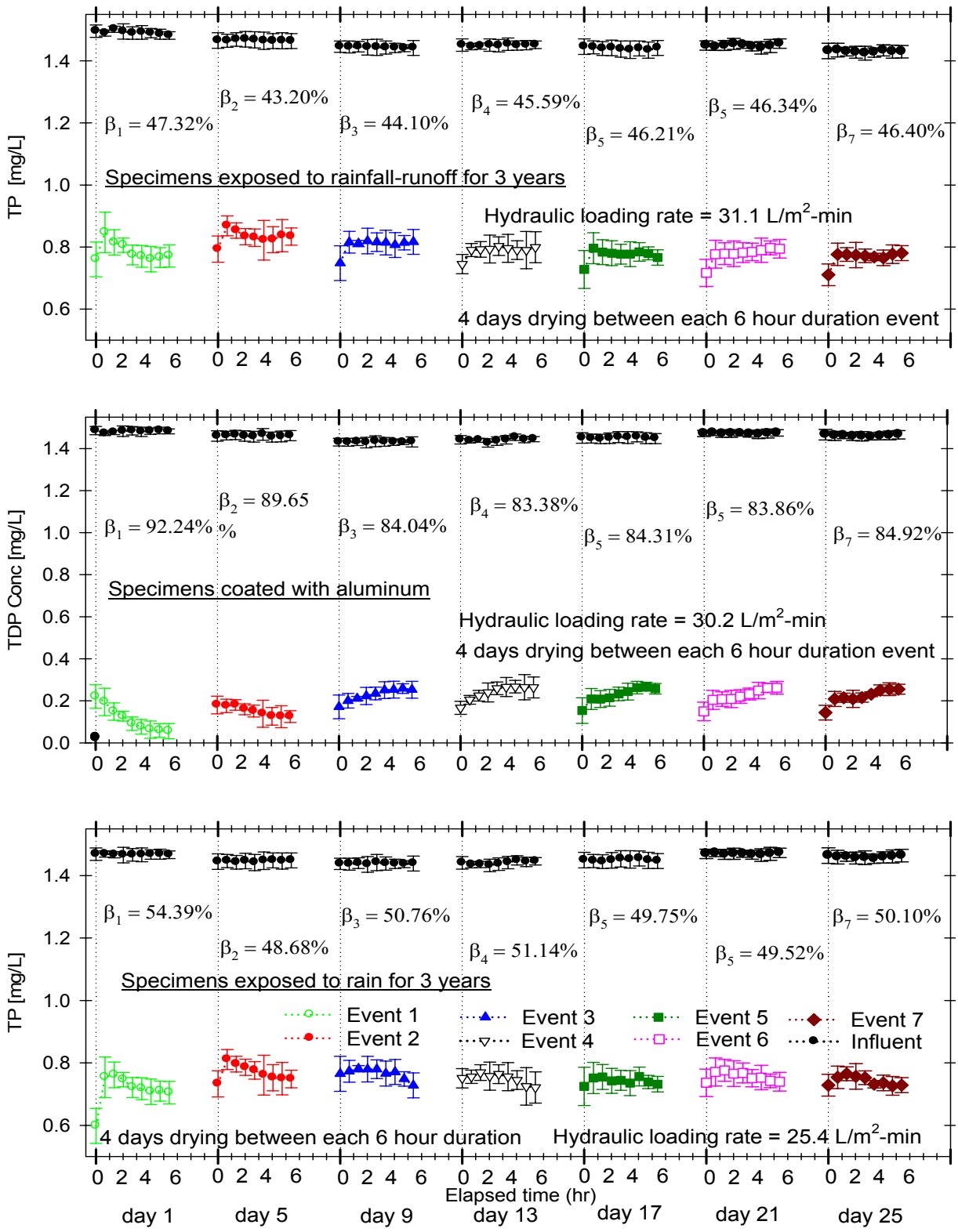

Figure 5-7 Total phosphorus (TP) removal properties of CPP. Influent [TP] was kept constant as 1.45 mg/L.

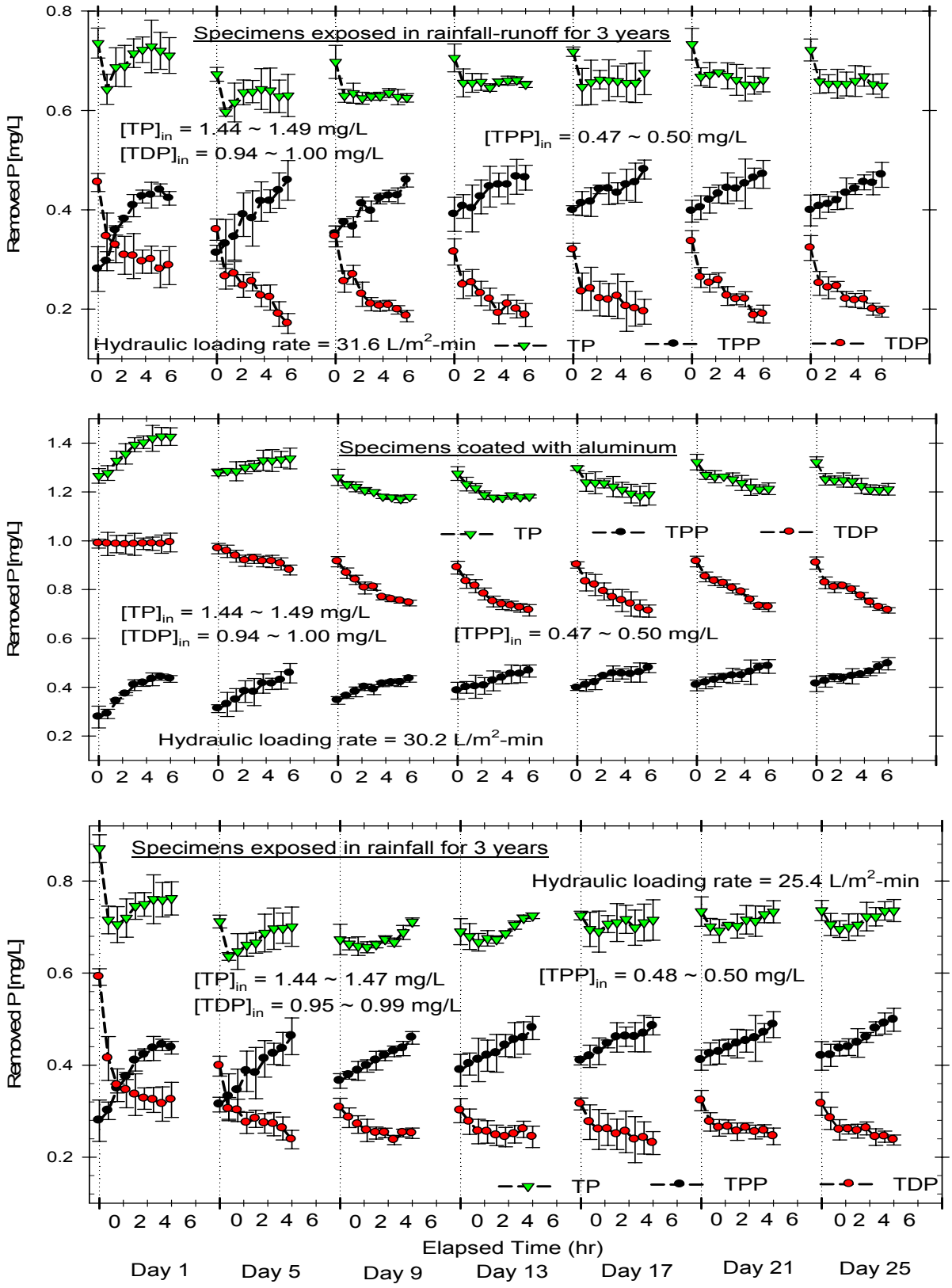

Figure 5-8 Removed TD, TDP and TPP by CPP coated with aluminum. Influent [TP] was kept constant as 1.4 mg/L.

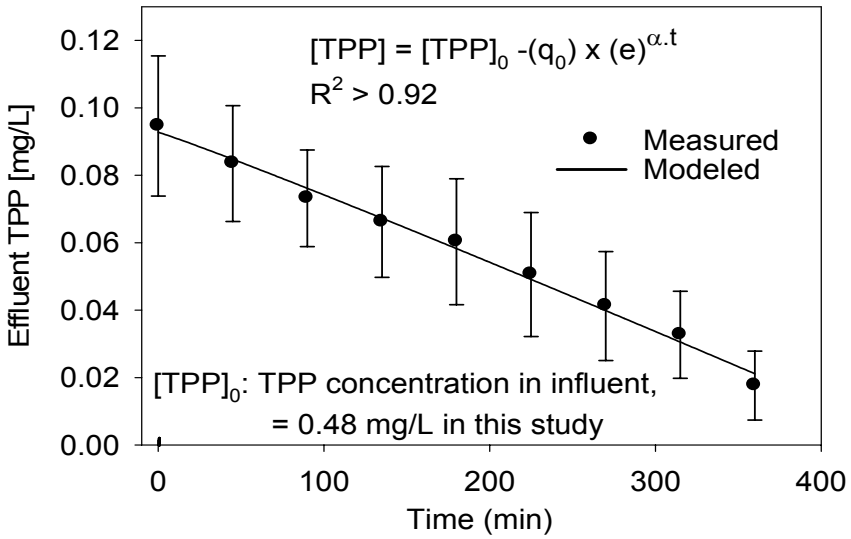

Figure 5-9 Total particulate phosphorus concentration [TPP] after infiltration through CPP materials. Effluent [TPP] during 6 hour filtration were modeled by an exponential model as $[TPP] = [TPP]_0 - q_0(e)^{\alpha \cdot t}$ with $R^2 > 0.92$, in this expression, $[TPP]_0$ is the TPP concentration of influent, equals to 1.4 mg/L. For group I specimens exposed to rainfall-runoff for 3 years, parameters in the model $q_0 = 0.3913$, and $\alpha = 0.0005$ with $R^2 = 0.94$; for group II specimens coated with aluminum, $q_0 = 0.3911$, and $\alpha = 0.0005$ with $R^2 = 0.94$, while for group III specimens exposed to rain only for 3 years, $q_0 = 0.4019$, and $\alpha = 0.0005$, with $R^2 = 0.95$.

5.5.5 Relationship of [TPP] Removal and Particle Removal through Filtration/Infiltration

In order to investigate the correlation of [TPP] and particle removal, p-value based on the pair-wise T-test between particle number, mass and particle surface area removal and TPP removal were calculated respectively. P_m, P_n, and P_{sa} were denoted as the p-value based on the pair-wise T-test between particle mass removal and [TPP] removal, between particle number removal and [TPP] removal, and between particle surface area removal and [TPP] removal, respectively. The difference between particle mass removal and TPP removal is significant ($P_{m1,2,3}$ = 0.0001, 0.0002, 0.0001); the difference between particle number removal and TPP removal is relatively significant ($P_{n1,2,3}$ = 0.116, 0.076, 0.105), while the difference between particle surface area removal and TPP removal is not significant ($P_{sa1,2,3}$ = 0.7615, 0.7436,

0.7388) with 95% confidence. Figure 5-10 shows the relationship of [TPP] removal and particle removal. It demonstrates that the removed TPP is mainly determined by the surface area of removed particles, rather than the particle mass or number. This results show that the main mechanism of phosphorus associated with particulates is surface absorption.

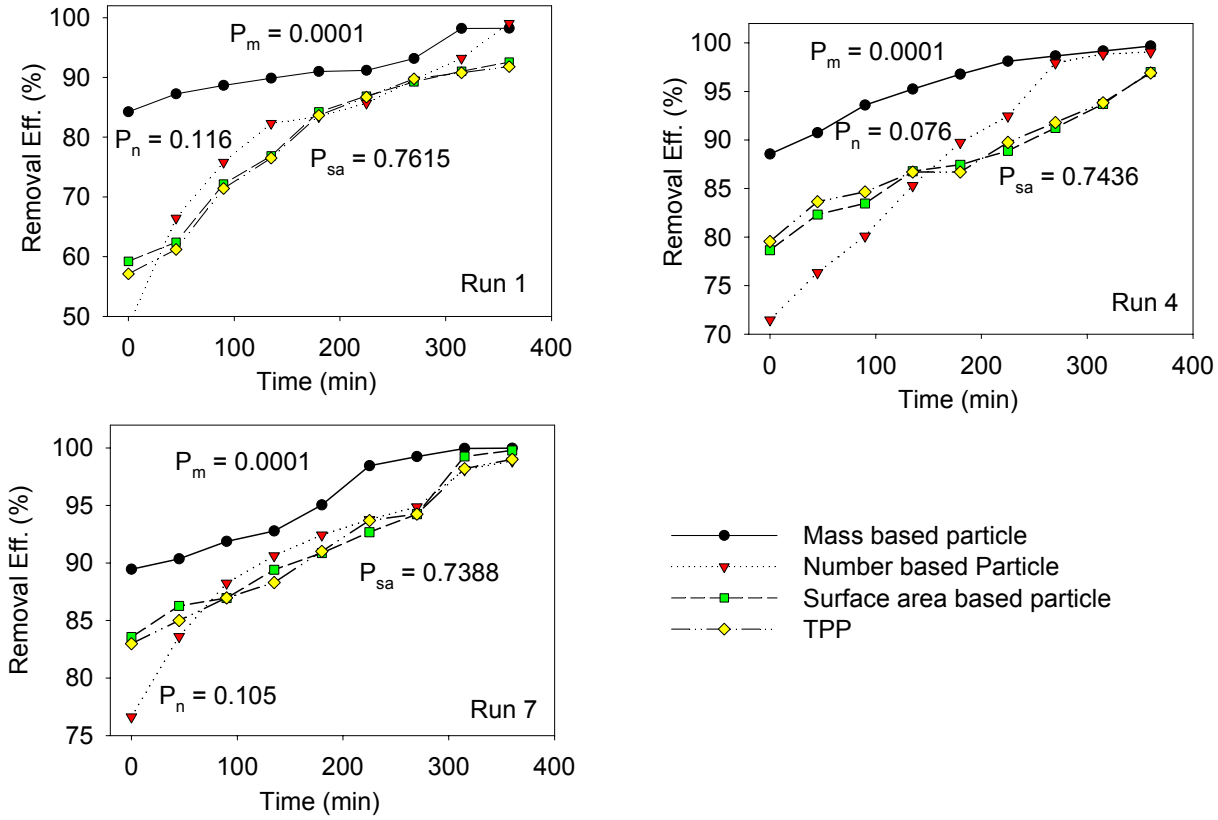

Figure 5-10 Relationship between TPP removal and particle removal. P_m, P_n, and P_{sa} are p-value based on the pair-wise T-test between, particle number removal, particle surface area removal and TPP removal, respectively. The difference between particle mass removal and TPP removal is significant ($P_{m1,2,3}$ = 0.0001, 0.0002, 0.0001); the difference between particle number removal and TPP removal is relatively significant ($P_{n1,2,3}$ = 0.116, 0.076, 0.105), and the difference between particle surface area removal and TPP removal is not significant ($P_{sa1,2,3}$ = 0.7615, 0.7436, 0.7388)

5.6 SUMMARY AND CONCLUSIONS

Three groups of specimens with different exposure condition were utilized to test the soluble infiltration, absorption properties of CPP as an absorptive and reactive material. pH, alkalinity, total phosphorus, total dissolved phosphorus and particle size distribution were

measured before and after runoff infiltrated through CPP specimens. The influent pH, alkalinity, TP and TDP were under good control.

Runoff pH was elevated after infiltrating though CPP. For specimens Group I and III, exposed to runoff or rainfall for 3 years, effluent pH was in the range of 7.8-8.5, always higher than the critical pH value of 6.5 for the retention of heavy metals (Fach 2002). For those aluminum coated specimens, the effluent pH was in the range of 8.5-10.6. Effluent pH was modeled by an exponential decay model.

Runoff alkalinity was elevated after infiltrating through CPP. The average elevation capacity for Group I and Group III specimens is 11.5% and 14.7%, respectively. The effluent alkalinity was in the range of 47-63 mg/L for Group I specimens and 47-81 mg/L for Group III specimens. The average elevation capacity for Group II coated with aluminum is up to 42%, and the effluent alkalinity was in the range of 55-95 mg/L. The effluent alkalinity concentration was modeled by an exponential decay model.

CPP could be used as an absorptive material for phosphorus removal. When influent [TDP] ≈ 1.0 mg/L, TDP removal efficiency was about 24.2 %, and the effluent [TDP] ranged from 0.55-0.82 mg/L for the uncoated specimens Group I. For the uncoated Group III, the TDP removal efficiency was about 28.5%, and the effluent [TDP] ranged from 0.38-0.76 mg/L. For the aluminum coated specimens, however, the average TDP removal efficiency is up to 82%, and the effluent [TDP] was below 0.2 mg/L. The effluent [TDP] was modeled by an exponential model.

For TP removal, when influent [TP] ≈ 1.45 mg/L, TP removal efficiency was about 46 %, and the effluent [TP] ranged from 0.7-0.8 mg/L for the uncoated specimens Group I. For the uncoated Group III, the TP removal efficiency was about 50%, and the effluent [TP] ranged from

0.6-0.8 mg/L. For the aluminum coated specimens, however, the average TP removal efficiency is up to 85%, and the effluent [TP] was below 0.23 mg/L.

With known TP and TDP removal efficiency, TPP removal efficiency were calculated. The effluent [TPP] was also modeled by an exponential model.

It was found that the TPP removal efficiency was related to removed particles. Instead of mass or number of particles, particle surface area determines the removal efficiency of TPP.

It is worth mentioning that all those tested specimens were exposed to rainfall or runoff for 3 years, the acid neutralization and phosphorus removal capacity were much lower than that of the fresh made CPP materials.

5.7 NOTATION

Symbols used in this chapter.

[alk] = alkalinity concentration, (M/L^3);

[m] = particle mass concentration, (M/L^3);

[N] = particle number concentration, (M/L^3);

[P] = phosphorus concentration, (M/L^3);

[TP] = total phosphorus concentration, (M/L^3);

[TDP] = total dissolved phosphorus concentration, (M/L^3);

[TPP] = total particulate phosphorus concentration, (M/L^3);

[TSS] = total suspended solids concentration (M/L^3)

D = particle diameter (L);

n = the number of particles in each size fraction;

SA = surface area of particles (L^2);

5.8 REFERENCES

Balades, J-D. , M. Legret and H. Madiec, 1995, "Permeable pavements: pollution management tools." Wat. Sci. Tech. Vol. 32, No. 1, pp. 49-56.

Carlson, R.E. and J. Simpson, 1996, "A Coordinator's Guide to Volunteer Lake Monitoring Methods." North American Lake Management Society, pp96.

Colandini, V., M. Legret, and J. D. Balades, 1995, "Metallic pollution in clogging materials of urban porous pavements." *Wat. Sci. Tech*., Vol. 32, No. 1, pp. 57-62.

Fach, Dipl.-Ing. S., Prof. Dr.-ing. W.F. Geiger, Dr.-Ing. C. Dierkes, 2002, "Development of an assessment procedure for permeable pavements." University of Essen, Urban Water Management, Universitaesstr. 15, 45141 Essen, Germany, pp. 1-12.

Field, R., H. Masters and M. Singer, 1982, "Status of porous pavement research." Water Res. Vol. 16, pp. 849-858.

Field, R, Hugh Masters, and Melvin Singer, 1982, "Porous pavement: research; development; and demonstration." Trans. Eng. J. of ASCE, Vol. 108, No. TE3. pp. 244- 258.

Hvitved-Jacobsen, T., N.B. Johansen and Y.A. Yousef, 1994, "Treatment systems for urban and highway run-off in Denmark." *The Science of the Total Environment*, 146/147, pp499-506

Li, Y.B., Buchberger, S.G., and Sansalone, J. (1999). "Variably Saturated Flow in Storm –Water Partial Exfiltration Trench." *Journal of Environmental Engineering*, *ASCE*, 556-565

Park, S. B. and M. Tia, 2004, "An experimental study on the water-purification properties of the porous concrete." *Cement and Concrete Research*, Vol. 34, pp. 177-184.

Pratt, C.J., 1999, "Use of permeable, reservoir pavement constructions for stormwater treatment and storage for re-use". Wat. Sic. Tech., 39(5), pp 145-151.

Rigler, F.H., E.J. Griffith, A. Beeton, J.M. Spencer, and D.T. Mitchell, 1973, "A dynamic view of the phosphorus cycle in lakes." *Environmental Phosphorus Handbook*, John Wiley & Sons.

Sansalone, John J., 1999, "Adsorptive infiltration of metals in urban drainage-media characteristics." The Science of the Total Environment 235 pp. 179-188.

Sansalone, John J., 1999, "In-sity performance of a passive treatment system for metal source control." Wat. Sci. Tech. Vol, 39, No. 2, pp.193-200.

Spivakov, B.Y., T.A. Maryutina and H. Muntau, 1999, "Phosphorus Speciation in water and sediments." *Pure Appl. Chem*., 71(11), pp 2161-2176

Standard Methods for the Examination of Water and Wastewater, 18th edition, 1992.

Stotz, G. and K. Krauth, 1994, "The pollution of effluents from pervious pavement of an experimental highway section: first results." *The Science of the Total Environment*, 146/147, pp. 465-470.

Zivica, V. and A. Bajza, 2001, "Acidic attach of cement based materials-a review. Part 1. princiole of acidic attack". Construction and building materials, 15, pp331-340.

CHAPTER 6 EVALUATION OF MIX DESIGN PARAMETERS FOR CEMENTITIOUS PERMEABLE PAVEMENT

6.1 INTRODUCTION

Cementitious permeable pavement (CPP) not only provides a smooth structural interface for traffic loading, it also functions as a passive unit operation and process for rainfall-runoff quality and quantity control (Park and Tia 2004, Sansalone et al. 2005; Teng and Sansalone 2004). The primary functions of CPP mix design is to achieve a desired strength and porosity by optimizing water-cement ratio (w/c), cement-aggregate ratio (a/c), aggregate gradation and maximum aggregate size (MAS).

The factors that dominate 28 day unconfined compressive strength (f_c') of CPP more than any other factors are the water/cement ratio (w/c) and the degree of compaction (Neville 1996, Popovics 1985). Over the narrow range of w/c values typical of conventional impervious pavement, 0.4-0.6; the (w/c-f_c') relationship is almost linear for test specimens cured in a standard warm, humid conditions and tested at 28 days (Neville 1996). However, this conclusion was based on concrete that was fully compacted. The degree of compaction influences the porosity and the whole internal structure of concrete, and thus influences strength of concrete in a significant way (Kobayasha et al. 2002, Tatro and Hinds 1992).

In addition to w/c, the factors of aggregate to cement (a/c) ratio, aggregate gradation, and aggregate maximum size (AMS) also influence concrete strength (Neville 1996, Gilkey 1961). For example, Erntroy and Shacklock (1954) concluded that for a constant w/c, a high a/c resulted in a leaner mix and resulted in a higher strength for the resulting concrete. The higher strength resulted from a lower total water content per unit volume of concrete in the leaner mix as

compared to a richer mix, with the lower total water content leading to a smaller void fraction (Neville 1996). The influence of a/c on porous concrete has not been well-established.

The type and texture of aggregate and aggregate gradations have important influences on concrete strength (Desai 2004; Knab 1983; Mohammad 2005; Mohammad et al. 2000; Perry and Gillott 1973, Sehgal 1984) and porosity (Abdullah et al. 1998, Kumart and Bhattacharjee 2003, Winslow and Liu 1990). For example, with a w/c = 0.4, the use of crushed aggregates generates compressive strength up to 38% higher for concrete as compared to gravel of the same gradation (Franklin and King 1971). Aggregate shape and texture also have important impact on concrete strength. For example, previous research has demonstrated that roughened coarse aggregate leads to a 10% higher compressive strength as compared to smooth aggregates (Neville 1996; Perry and Gillott 1977). Previous research findings indicate that for the same paste composition and the same degree of hydration, the presence of coarse aggregate results in an increased porosity (Abdullah et al. 1998, Kayyali 1987, Kumart and Bhattacharjee 2003, Neville 1996, Winslow and Liu 1990).

Absorption and moisture condition of aggregates must be considered in mix design. Previous research findings indicate that absorption and moisture influence the free water that is available for hydration, thus affect the concrete strength (Neville 1996). The maximum aggregate size will affect workability of fresh concrete and the strength of hardened concrete (Abdel-Jawad and Abdullah 2002).

To facilitate the infiltration of rainfall-runoff through CPP, with a desired hydraulic conductivity, the ability to modify CPP pore characteristics is desirable through parameter modifications of the mix design. Porosity parameters determine the hydraulic conductivity and filtration/infiltration function of CPP (Goto and Roy 1981, Yaman et al. 2002a, b). In addition,

previous research has indicated that porosity can be an effective factor for estimating concrete durability Kolias (1994).

The w/c ratio also influences porosity of concrete. For full-compacted and well-graded aggregate used with conventional concrete, the higher the w/c ratio, the higher the porosity, and the higher the hydraulic conductivity (Neville 1996). Powers et al. (1954) found that when the w/c ratio was lowered from 0.7 to 0.3, the hydraulic conductivity was reduced by three orders of magnitude, from 10^{-10} to 10^{-13} cm/s. Findings by Whiting (1998) found that over a w/c ratio range of 0.75 to 0.26, the hydraulic conductivity decreased by up to 4 orders of magnitude, from 10^{-10} to 10^{-14} cm/s.

Since w/c, a/c, aggregate texture, aggregate size gradation, and the degree of compaction have influence on both the strength and the porosity of conventional concrete, and to date are relatively undocumented for permeable concrete, this study investigates the influence of these factors on CPP. It should be recognized that none of those factors independently influence strength and porosity of permeable concrete. In mix design, all these factors combine to determine the structural and pore characteristics of CPP.

6.2 OBJECTIVES

The main goal of this study was to evaluate mix design parameters on the basic structural and hydraulic indices of CPP material so that a mix design would provide a specified strength (f_c' > 3000 psi) and effective porosity (ϕ_e > 20%) using total porosity, ϕ_t as a surrogate parameter. Therefore, this study had a number of objectives. The first objective was to evaluate the influence of water to cement ratio (w/c) on strength and porosity of CPP, and to develop a relationships for w/c-to total porosity and also to strength. The second objective was to evaluate the influence of aggregate gradation and maximum aggregate size on strength and porosity of

CPP. The third objective was to examine the relationship between aggregate to cement ratio (a/c) and CPP strength and porosity. The fourth objective was to evaluate the influence of porosity on CPP strength. The fifth objective was to examine the compressive (f_c') and splitting tensile strength (f_s) for the designed CPP materials in order to develop the f_c'-f_s relationship. The sixth objective is to evaluate the hydraulic conductivity (k) of the CPP mix designs and to investigate the ϕ_t-k relationship.

6.3 BACKGROUND

6.3.1 Unconfined Compressive Strength (f_c')

Since high porosity reduces concrete strength, strength, as measured by compressive strength, is one of the most concerns regarding cementitious permeable pavement (Kobayashi et al. 2002). ASTM C39/C39M-04a (2004) specifies the standard method for concrete compressive test. Many factors influence the test results, such as specimen height/diameter ratio, specimen size, maximum aggregate size and loading rate (Neville, 1996). The standard cylinder specimen is 6 in. in diameter and 12 in. in length. Loading rate should be between 28-42 psi/s (ASTM 2004). The ASTM standard method (2004) specified that the standard specimen height/diameter ratio for compressive test is 2. ASTM C 42-90 (1990) gives the correction factors for specimens with height/diameter different from 2.

For a given height to diameter ratio, usually, a small size of specimen leads to larger tested compressive strength (Blanks and Mcnamara, 1935). Blanks and Mcnamara (1935) found that the tested compressive strength of specimens with size of 4 in. in diameter is 105% of that of specimens with size of 6 in. in diameter, while that of specimens with size of 8 in. in diameter is only 96% of that for 6 in. specimens (Neville, 1996).

There are 6 types of fracture patterns that are typically identified after a compression test of a concrete specimen. A Type I pattern results in reasonably well formed cones on both ends, and less than 1 in cracking through caps; Type II pattern results in a well-formed cone on one end, vertical cracks running through caps, and no well defined cone on other end; Type III is the columnar vertical cracking through both ends, with no well-formed cones; Type IV is a diagonal fracture with no cracking through the ends; Type V is side fractures at top or bottom, and Type VI is similar to Type V but the end of cylinder is pointed (ASTM C39/C39M-04a 2004)).

6.3.2 Relationship between Total Porosity (ϕ_t) and Strength (f_c')

The strength of concrete is a function of porosity (Neville 1996). Although high porosity is desirable in CPP, high porosity will reduce concrete strength. The relationship between concrete compressive strength and porosity was presented as by Gudemo (1975)

$$f_c' = f'_{c0}(1-\phi_t)^n \tag{6-1}$$

In this expression, f_c' = strength of concrete with total porosity ϕ_t (%); f'_{c0} = strength of concrete with zero porosity, and *n* is a coefficient determined by experimental measurements of f_c' and f_t.

In addition to total porosity, the effect of pore size distribution on strength must be considered also. Generally, at a given porosity, smaller pores lead to a higher strength of the cement paste (Neville 1996).

6.3.3 Tensile Strength (f_t) Test

Although pavement is not normally designed to resist direct tension, tensile strength of concrete mitigates cracking development, and is often used to resist shear in un-reinforced sections and resist shrinkage and temperature stresses (Neville 1996, Oluokun 1991). There are three types of test for strength in tension: direct tension test, flexure test (also know as the third point loading test) and splitting tensile test (Lin and Wood 2003).

Direct tension test is seldom conducted due to the difficulty of application of a pure tension force. European Standard Eurocode ENV1992-1 (1992) gives an estimation of direct tensile strength from f_c' when f_c' < 7252 (psi) at 28 days (Desai 2004).

$$f_{dt} = 1.55 \times (f_c')^{0.67} \text{ (psi)} \quad (6\text{-}2)$$

6.3.4 Flexure Tensile Strength (f_r) and Correlation with f_c'

Flexure test and splitting test are usually used to measure the strength in tension. The theoretical maximum tensile stress of flexure test for the tested beam is known as the modulus of rupture (f_r) (Neville 1996). Much research has been conducted to examine the relationship between f_c' and f_r. Kaplan (1959) reported that the elastic modulus of the aggregates was the most important influencing factor on the modulus of rupture. ACI 435 (1968) presented an expression to estimate f_r based on known f_c' for concrete (Khan, et al. 1996).

$$f_r = (4.75 \sim 12) \times (fc')^{1/2} \text{ (psi)} \quad (6\text{-}3)$$

Jerome (1984) and Raphael (1984) presented the relationship between the rupture of modulus (f_r) and compressive strength (f_c') as

$$f_r = 2.3 \times (f_c')^{2/3} \text{ (psi)} \quad (6\text{-}4)$$

Bakhsh et al. (1990) gave the following expression for f_r - f_c' correlation.

$$f_r = 9.6 \times (f_c')^{1/2} \text{ (psi)} \quad (6\text{-}5)$$

6.3.5 Splitting Tensile Strength (f_s) and Correlation with f_c'

The splitting tensile test is a simple to perform and provides repeatable results as compared to the flexure test and direct tensile test (Wright 1955). Many relationships between splitting tensile strength and compressive tensile strength have been developed. ACI318-99 (1999) presents the following relationship (Desai 2003).

$$f_s = 6.7 \times (f_c')^{1/2} \quad (6\text{-}6)$$

However, results from Oluokun (1991) indicated that this relationship was not accurate enough to predict tensile strength from compressive strength. After studying on tensile and compressive strength tested from 168 laboratories, Oluikun (1991) developed the f_s-f_c' correlation as

$$f_s = 1.38 \times (f_c')^{0.69} \text{ (psi)} \quad (6\text{-}7)$$

Noville (1996) provided another f_s-f_c' relationship different from that of ACI.

$$f_s = 1.58 \times (f_c')^{2/3} \text{ (psi)} \quad (6\text{-}8)$$

Malhotra (1969) provided a similar relationship.

$$f_s = 3.67 \times (f_c')^{0.565} \text{ (psi)} \quad (6\text{-}9)$$

Akazawa (1953) also provided an expression to estimate f_s from f_c'.

$$f_s = 0.369 \times (f_c')^{0.73} \text{ (psi)} \quad (6\text{-}10)$$

The differing results indicate that although all tests followed the same standard test method, the variability of the test results is large, and as such resulted in quite different relationships, as illustrated from the literature.

6.4 METHODOLOGY

6.4.1 Materials for Mix Design

Materials for CPP specimen mix design components include type I Portland cement, coarse aggregate (crushed limestone), fine aggregate (silica sand), and potable water. Materials properties including specific gravity (ρ_s), water absorption onto aggregate and water used for mix design. These mix design were list in Table 6-1. In this table, moisture and absorption of fine aggregate were tested according to ASTM C 70-94(2001) and ASTM C 128-01 (ASTM 2004). Absorption of coarse aggregate was tested according to ASTM C 127-01 (ASTM 2004). Aggregates were sieved according to ASTM C136-01 (ASTM 2004).

Table 6-1 Material properties and indices for CPP specimen mix design components.

Property	Cement	CA	FA
ρ_s (σ)	3.15 (0.01)	2.68 (0.02)	2.62 (0.02)
Moisture (σ)	/	1.04% (0.02%)	0.5% (0.004%)
Absorption (σ)	/	0.05% (0.004%)	0.05% (0.004%)

ρ_s: specific gravity
σ: standard deviation
CA: coarse aggregate-crushed limestone, coarser than No.16, (1.18 mm);
FA: fine aggregate portion, silica sand, finer than No. 16 (1.18 mm);
Cement is Type I Portland cement;

6.4.2 Mix Design Parameter Evaluation

In order to investigate the influence of w/c, a/c and gradation (through maximum aggregate size, MAS) on CPP strength and porosity characteristics, 6 mix design batches were designed with different w/c, a/c and MAS, as illustrated in Table 6-2.

Table 6-2 Target values of design parameter for the 6 mix design batches

Batch #	Design parameters			
	Entire gradation	**MAS**	**w/c**	**a/c**
B1	Finer (I)	3/8 inch	0.3	5.5
B2	Finer (I)	3/8 inch	0.5	5.5
B3	Finer (I)	3/8 inch	0.4	5.5
B4	Coarser (II)	½ inch	0.3	5.5
B5	Coarser (II)	½ inch	0.3	4.0
B6	Coarser (II)	½ inch	0.3	7.0

w/c: water to cement ratio;
a/c: aggregate to cement ratio;
MAS: maximum aggregate size;
Finer (I) and coarser (II) gradations are illustrated in Figure 6-1;
Finer gradation (I): d_{50}: 4.75 mm, d_{15}: 9.5 mm, d_{85}: 1.18 mm ;
Coarser gradation (II): d_{50}: 4.75 mm, d_{15}: 9.50 mm, d_{85}: 2.36 mm.

Two aggregate gradations (with differing MAS) were utilized as illustrated in Figure 6-1. The maximum size of Gradation I is 3/8 inch (9.5 mm), and the maximum size of Gradation II is

½ inch (12.7 mm). An additional difference between Gradation I and II is that, in Gradation I, only 5% of aggregates are finer than ASTM No.16 (1.18 mm), and this mass was distributed to the ASTM No. 50 (0.3 mm) sieve, while in Gradation II, there was 8% finer than No.16 and this mass was evenly distributed between the ASTM No. 30 (0.6 mm) , 50 (0.3 mm), 100 (0.15 mm) and 200 (0.075 mm).

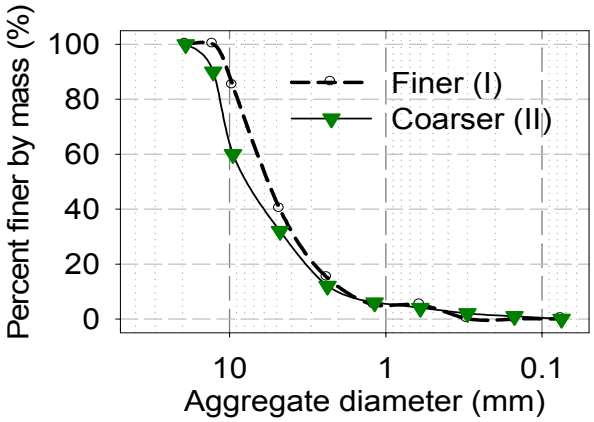

Figure 6-1 Illustration of the fine and coarse aggregate gradation for the CPP mix design. The maximum size of the fine gradation is 3/8 inch (9.50 mm), and the coarse gradation is ½ inch (12.7 mm). In the fine gradation only 5% of aggregates were finer than No.16 (1.18 mm), and was only distributed to the No. 50 (0.30 mm); while in the coarse gradation there was 8% of the mass finer than the No.16 (1.18 mm) and this mass was evenly distributed among the size of No. 30 (0.60 mm) 50 (0.30 mm), 100 (0.15 mm) and 200 (0.075 mm).

For the finer gradation (I) of aggregate, 3 different w/c ratios of 0.3, 0.4 and 0.5 were employed with the same a/c of 5.5, and denoted as Batch 1, 2 and 3, respectively. From these 3 batches, the influence of w/c on CPP behavior was obtained. For the coarser gradation (II) of aggregate, 3 different a/c ratios, namely 4.0, 5.5 and 7.0, were utilized with the same w/c of 0.3, denoted as Batch 4, 5 and 6, respectively. From these 3 batches, the influence of a/c on CPP behavior was obtained. Noting that Batch 1 and Batch 4 have the same w/c of 0.3 and the same a/c of 5.5, but with a different gradation, the influence of a finer and coarser gradation on CPP behavior could be compared.

6.4.3 Material Proportion Calculation

Material constituent proportions were determined by the absolute volume method. In this method, material proportions were determined by combining materials to 1.0 yd^3 (27 ft^3) of volume (Neville 1996).

$$\frac{W_w}{62.4}+\frac{W_c}{62.4\cdot\rho_c}+\frac{W_{CA}}{62.4\cdot\rho_{CA}}+\frac{W_{FA}}{62.4\cdot\rho_{FA}}=27\,(ft^3) \tag{6-11}$$

With known specific gravity (ρ) of each constituent, and given w/c and a/c and ratio of the coarse aggregate (CA) portion of a gradation and the fine aggregate (FA) portion of a gradation, designated C/F, the weight of water (W_w) for 1.0 yd^3 of volume could be obtained by the following expression.

$$\frac{W_w}{62.4}\{1+\frac{1}{(w/c)\cdot\rho_c}+\frac{(C/F)\cdot(a/c)}{[1+(C/F)]\cdot(w/c)\cdot\rho_{CA}}+\frac{(a/c)}{[1+(C/F)]\cdot(w/c)\cdot\rho_{FA}}\}=27\,(ft^3) \tag{6-12}$$

The weight of cement (W_c), coarse aggregate (W_{CA}) and fine aggregate (W_{FA}) could be calculated by the following equations.

$$W_c=\frac{1}{(w/c)}W_w \tag{6-13}$$

$$W_{CA}=\frac{(C/F)\cdot(a/c)}{[1+(C/F)]\cdot(w/c)}W_w \tag{6-14}$$

$$W_{FA}=\frac{(a/c)}{[1+(C/F)]\cdot(w/c)}W_w \tag{6-15}$$

In these expressions, C/F represents the mass ratio of the coarse aggregate (CA) portion of the gradation to the fine aggregate (FA) portion of the gradation. W_w, W_c, W_{CA} and W_{FA} are weight (lb) of water, cement, coarse aggregate and fine aggregate to yield 27 ft^3 volume. For lab trial batch volume (V_b, ft^3) different from 27 ft^3, material weight could be adjusted by multiplying by the reduction factor (V_b/27). Weight of water, cement, coarse aggregate and fine

aggregate for a trail batch is denoted as w_w, w_c, $(w_{CA})_{SSD}$ and $(w_{FA})_{SSD}$, respectively. The subscript of SSD represents the condition of saturated surface dry.

6.4.4 Moisture Correction

Noticing that the weights of water and aggregate for the above calculation are estimated under the saturated surface dry (SSD) condition for aggregates, moisture correction is needed during mix design when the aggregate moisture condition is different from SSD (Neville 1996). In this case, the aggregate may bring some free water to or absorb some free water from the mix.

Free moisture (p_m, %) can be calculated as

$$p_m = \text{Moisture Content} - \text{Absorption}. \tag{6-16}$$

Aggregate weight after moisture correction, $(w)_{moist}$ (lb), can be determined as

$$(w_{CA})_{moist} = [1 + (p_m)_{CA}] \cdot (w_{CA})_{SSD} \tag{6-17}$$

$$(w_{FA})_{moist} = [1 + (p_m)_{FA}] \cdot (w_{FA})_{SSD} \tag{6-18}$$

Water weight should be adjusted by the following equation.

$$(w_w)_{correct} = w_w - (w_{CA})_{SSD} \cdot (p_m)_{CA} - (w_{FA})_{SSD} \cdot (p_m)_{FA} \tag{6-19}$$

Table 6-3 shows the trial batch yield and all material weight for each mix.

Table 6-3 Material proportion for CPP mix design for each batch

Batch #	Material proportions			
	Water (kg)	Cement (kg)	CA kg	FA kg
B1	3.89	10.51	54.41	2.88
B2	5.42	9.85	51.00	2.70
B3	4.95	10.21	52.81	2.80
B4	3.18	10.59	55.34	2.91
B5	4.53	13.40	49.88	3.20
B6	3.21	8.75	57.02	3.66

CA: Coarse aggregate, crushed limestone, coarser than No.16 sieve size (1.18 mm);
FA: Fine aggregate, silica sand, finer than No. 16 (1.18 mm);
Cement type: Type I Portland cement.

6.4.5 Specimen Fabrication and Curing

The method of making test cylinders is prescribed by ASTM C192-90a and the fabrication process followed the standard method of ASTM 192/c 192M-02 and ASTM685/C 685M -01 (ASTM 2004). Cylinder molds are specified by ASTMC470-94. For each batch of mix design, 3 groups of specimens were made with different levels of compaction: full compaction, half compaction and no compaction. In full compaction, both vibration using a vibrating tables and compaction using a rod manually were applied on cylinder specimens. For half compaction, only vibration was applied. For no compaction specimens, neither vibration nor rod compaction was applied during fabrication. With this strategy, the influence of compaction on specimen strength properties could be obtained.

Specimens were covered with plastic bags and stayed in air for 24 hours, and then were moved to 100% moisture room for curing.

6.4.6 Slump, Unit Weight and Air Content Tests for CPP Mixes

Slump tests of fresh CPP mix were conducted within 5 minutes after the CPP mix was made following the standard method of ASTM 143/C 143M-3 (ASTM 2004).

Unit weight (density) of fresh CPP for each batch of mix was tested in accordance with Test Method of ASTM C138/C 138M-01a (ASTM 2004). A 0.25 ft^3 air meter container was utilized to test the density. By weighting the mass contained in the measure (M, lb), with the known measure volume of 0.25 ft^3, density of the fresh CPP could be calculated as $\rho_f = M/0.25$ (lb/ft^3). The same amount of fresh mix in the meter container was then used to determine the air content of the fresh CPP following the guideline of the ASTM 138/C 138M -01a: Test Method for Density (Unit Weight), Yield, and Air Content (Gravimetric) of Concrete (ASTM 2004).

6.4.7 Compressive Test and Splitting Tensile Test

Compressive and splitting tensile strengths for all 6 batches of specimens were tested after 28 days of curing in the 100% moisture room. Compressive strengths were tested following the Standard Method of ASTMC 39/C 39M-04a. The loading rate was 30,000 lbs/min. The coefficients of variation of tested f_c' for every batch are lower than 9%. Splitting tensile strengths were tested according to the Standard Method of ASTMC C496-96. The loading rate was 7,500 lbs/min. The within batch coefficient of variation is lower than 5% for each mix.

6.4.8 Total Porosity

Total porosity can be estimated with known specific gravity (ρ_s).

$$\phi_t = (1 - \frac{W/\rho_s}{V_b}) \times 100\% \tag{6-20}$$

In this expression W is the dry weight (g) and V_b the bulk volume (cm^3) of a specimen, and V_s is the solid volume (cm^3). The measurement of specific gravity ρ_s followed ASTM D 5550-4 (1994) through inert gas pycnometry. The gas utilized in this procedure was ultra-high pure *He* for inertness and ability to enter pore space approaching 1 angstrom (10^{-10} m) in diameter. Triplicate aliquots were analyzed for each test. Based on ρ_s, total porosity of CPP cores can be estimated by equation (6-20).

6.4.9 Hydraulic Conductivity k_{sat} Test

Hydraulic conductivity for all batches of specimens with different degree of compaction was tested. An experimental setup was designed to measure the saturated hydraulic conductivity in constant head, as Figure 3-1 illustrated. CPP specimens were dip into DI water for 48 hours before test to make sure a saturated condition. During test, tap water was pumped from the tank to specimen column by a peristaltic pump (Masterflux 7520-40). A series of constant head (5, 10, 20, 30, 40, 50, 60 mm over the surface of CPP specimen) were achieved by adjust the outlet level

of overflow. Influent flow rates were controlled by regulating the speed of the peristaltic pump to make it keep overflowing during all test time, so that a certain constant head is maintained. After the system was steady, effluent volume was collected for 5 minutes, and then measured. At least 5 samples were measured for each hydraulic head. According to Darcy's Law, k_{sat} could be presented as

$$k_{sat} = Q/(A \cdot t \cdot i) \tag{6-21}$$

In this expression, k_{sat} is saturated hydraulic conductivity in cm/s; Q is the effluent volume (mL) collected in time t (s); A is the cross section area of the CPP specimen. $i = \Delta h/L$ representing hydraulic gradient; Δh is head loss (cm) and L is the length of specimen (cm).

6.5 RESULTS AND ANALYSIS

6.5.1 Properties of Fresh CPP Mixes

Immediately after the CPP mix was made, slump, density and air content tests were conducted. Table 6-4 summarizes the test results of these properties for each batch. Results indicate that the slump of Batch 5 is 0, indicating that the workability was not good. Compared to other batches, Batch 3 has the lowest air content of 6.1% and yield of 1.09 ft^3, and highest density of 144.2 lb/ft^3. Slump of all other batches of design is from 5.0 to 7.0 in. The slump type for all batches was collapse, demonstrating a high workability. Air contents of all other batches ranged from 6.52 to 11.56%; unit weight ranged from 92.7 to 136.4 lb/ft^3.

6.5.2 Properties of CPP Specimens

6.5.2.1 Specific gravity (ρ_s) and total porosity (ϕ_t)

Specific gravity ρ_s was measured for each batch of specimens, resulting in ρ_s = 2.744, 2.736, 2.740, 2.734, 2.760 and 2.728 for batch B1-B6, respectively. From these results, it was found that ρ_s was mainly determined by the factor of a/c, the higher the a/c, the lower the ρ_s. The

reason is that the aggregate is lower than the cement ρ_s. With the highest a/c of 7.0, the ρ_s of B6 is the lowest as 2.728; the lowest a/c of 4.0 generated a highest ρ_s of 2.76 for B5, and for B1, B2, B3, B4 with a median a/c of 5.5, the ρ_s is almost the same with a mean of 2.739 and a standard deviation of 0.004.

Table 6-4 Properties of fresh CPP mix for the 6 batches of mix design

Batch #	Total Material kg {lb}	Slump cm (σ)	Air Content %	Unit Weight kg/m^3 (lb/ft^3)	Yield m^3 (ft^3)
B1	71.69 {158.08}	12.71 (2.60)	10.04	1641.61 {102.52}	0.044 {1.54}
B2	68.97 {152.08}	14.05 (3.88)	6.52	2184.50 {136.41}	0.031 {1.11}
B3	70.77 {156.04}	17.82 (5.08)	7.68	1945.93 {121.52}	0.036 {1.28}
B4	72.02 {158.80}	17.36 (4.27)	10.78	1574.36 {98.41}	0.046 {1.62}
B5	71.01 {156.58}	0.00 (0.00)	6.12	2309.52 {144.21}	0.031 {1.09}
B6	72.65 {160.19}	17.32 (3.51)	11.56	1484.70 {92.71}	0.049 {1.73}

Total material proportions for each batch were obtained from Table 6-3;
Yield = (Total mass of all materials for each batch)/(Unit weight)

Based on the geometric-gravimetric properties and known ρ_s, ϕ_t could be obtained for each CPP specimens using (6-20). Table 6-5 summarizes the results of ϕ_t of for each batch of specimens with different degree of compaction. Results indicate that for fully compacted specimens, the Batch B2 design (w/c-a/c-gradation: 0.5, 5.5, finer) generated the highest ϕ_t of 28.42%, while the Batch B5 (0.3, 4.0, coarser) led to the lowest ϕ_t of 18.27%. The ϕ_t of B1 (0.3, 5.5, finer), B3 (0.4, 5.5, finer), B4 (0.3, 5.5, coarser) and B6 (0.3, 7.0, coarser) range from 23.53 to 27.53%. For those specimens with half compaction, the ϕ_t ranges from 20.47 to 36.42%, and for those specimens without compaction, the ϕ_t ranges from 30.46 to 41.58%.

Table 6-5 Strength, porosity and hydraulic conductivity test results for all specimen batches

Batch #	Design parameters			Properties of hardened concrete			
	Entire Gradation	w/c	a/c	f_c' MPa	f_s MPa	ϕ_t (%)	k (10^{-2} cm/s)
Full Compaction							
B1	Finer (I)	0.3	5.5	27.28^{V}	3.03	24.12	19.21
B2	Finer (I)	0.5	5.5	14.51^{V}	1.55	28.42	58.34
B3	Finer (I)	0.4	5.5	19.82^{VI}	2.10	25.04	22.02
B4	Coarser (II)	0.3	5.5	32.58^{I}	3.94	23.53	19.11
B5	Coarser (II)	0.3	4.0	34.75^{VI}	4.23	18.27	8.04
B6	Coarser (II)	0.3	7.0	18.13^{I}	2.66	27.53	59.64
Half Compaction							
B1	Finer (I)	0.3	5.5	15.47^{V}	1.97	27.45	22.41
B4	Coarser (II)	0.3	5.5	17.07^{VI}	2.24	24.35	25.37
B5	Coarser (II)	0.3	4.0	19.97^{V}	2.59	20.47	9.22
B6	Coarser (II)	0.3	7.0	14.65^{V}	1.67	36.42	110.54
No Compaction							
B1	Finer (I)	0.3	5.5	6.78^{VI}	1.08	39.29	157.42
B2	Finer (I)	0.5	5.5	9.92^{VI}	1.39	32.56	56.68
B3	Finer (I)	0.4	5.5	12.31^{VI}	1.97	30.46	39.74
B4	Coarser (II)	0.3	5.5	8.80^{V}	1.39	33.92	40.08
B5	Coarser (II)	0.3	4.0	9.84^{IV}	1.52	35.26	78.10
B6	Coarser (II)	0.3	7.0	4.54^{IV}	0.83	41.58	184.07

Finer (I) and Coarser Gradation (II) are illustrated in Figure 6-1.
w/c: water to cement ratio in weight;
a/c: aggregate to cement ratio in weight;
f_c': compressive strength (psi);
f_s: splitting tensile strength (psi);
ϕ_t: total porosity (%), calculated using (6-20) with known specific gravity (ρ_s);
k: hydraulic conductivity:
Superscripts of f_c' represent fracture type during compressive test, as described in "BACKGROUND" session defined by ASTM C39/C39M-04a (2004)

6.5.2.2 Compressive strength (f_c') and splitting strength (f_s)

Table 6-5 summarizes results of compressive strength (f_c') and splitting tensile strength (f_s). Results indicate that f_c' of all specimens with half or none compaction was less than 3000 psi, and f_s was less than 400 psi. For the specimens with full compaction, B1, B4 and B5 have an f_c' higher than 3000 psi and f_s higher than 400 psi. Most of the fracture types during compressive

tests were Type 5 or 6, namely side fracture at top or bottom. The results also demonstrate that the degree of compaction significantly influences specimen strength.

6.5.2.3 Hydraulic Conductivity (k)

Table 6-5 summarizes hydraulic conductivity results. A very high hydraulic conductivity was measured for CPP. For those specimens without compaction k ranges from 40 to 184 × 10^{-2} cm/s; for those with half compaction, k ranges from 9 to 110 × 10^{-2} cm/s, and for the specimens with full compaction, k ranges from 8 to 60 × 10^{-2} cm/s. With such a high hydraulic conductivity, for the full compacted specimens, the hydraulic drainage capacity ranges from 50 to 360 L/m^2-min even at very low hydraulic head, which will be very beneficial for rainfall-runoff peak flow and volume control.

6.5.2.4 Influence of w/c on Strength and ϕ_t

Figure 6-2 illustrates the influence of w/c on CPP compressive strength (f_c'), splitting tensile strength (f_s) and total porosity (ϕ_t).

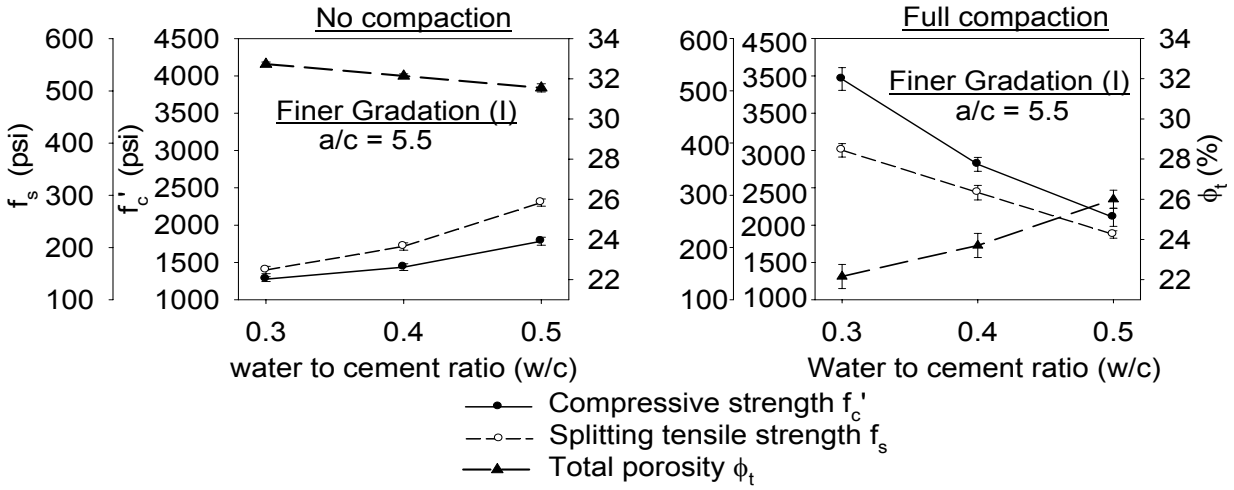

Figure 6-2 Water cement ratio (w/c) influence on CPP strength indices (f_c and f_s) and total porosity (ϕ_t). For a given aggregate to cement ratio (a/c) a given gradation, higher w/c ratios generate higher ϕ_t and lower f_c and f_s for CPP specimens with full compaction; while for CPP specimens with no compaction, higher w/c ratios generate lower ϕ_t and therefore higher f_c' and f_s. All strength results tested at 28 days.

With the same finer gradation and the same a/c of 5.5, for the specimens with full compaction, ϕ_t increase from 22.16 to 26%, f_c' decrease from 3957 to 2104 psi, and f_s decrease from 439 to 225 psi when w/c increase from 0.3 to 0.5.

For those CPP specimens without compaction, however, f_c' and f_s increase from 983 to 1785 psi and from 157 to 286, respectively, with the increase of w/c from 0.3 to 0.5. For those specimens without compaction, the increase of w/c decreases porosity and results in the increase of strength. When w/c changes from 0.3 to 0.5, ϕ_t decreases from 35.12 to 31.55%. These results illustrates that concrete strength is not only determined by w/c, but also by degree of compaction.

6.5.2.5 Influence of a/c on Strength and ϕ_t

Figure 6-3 summarizes the influence of a/c on CPP compressive strength (f_c'), splitting tensile strength (f_s) and total porosity (ϕ_t). With the same coarser gradation and the same w/c of 0.3, for both specimens with or without compaction, ϕ_t increases with the increase of a/c, resulting in the decrease of f_c' and f_s. For full compacted specimens, when a/c = 4.0, 5.5 and 7.0, respectively, results indicate a corresponding f_c' = 5040, 4725, 2629 psi; f_s = 386, 571, 614 psi, and ϕ_t = 16.58, 19.47, 26.75%, respectively. For those without compaction, when a/c = 4.0, 5.5 and 7.0, respectively, corresponding f_c' = 1427, 1276 and 658 psi; f_s = 221, 201 and 120 psi, and ϕ_t = 31.84, 32.73 and 40.26%, respectively. This result is different from that drawn for conventional impervious concrete. For impervious concrete with very low porosity, higher a/c leads to a leaner mix which results in a higher strength (Erntroy and Shacklock 1954). For CPP, however, the high a/c will increase the total porosity which is a dominant factor that determines strength. This result for porous concrete was verified by Park and Tia (2004). Park and Tia (2004) also found that the higher the a/c, the lower the compressive strength and the higher the total porosity.

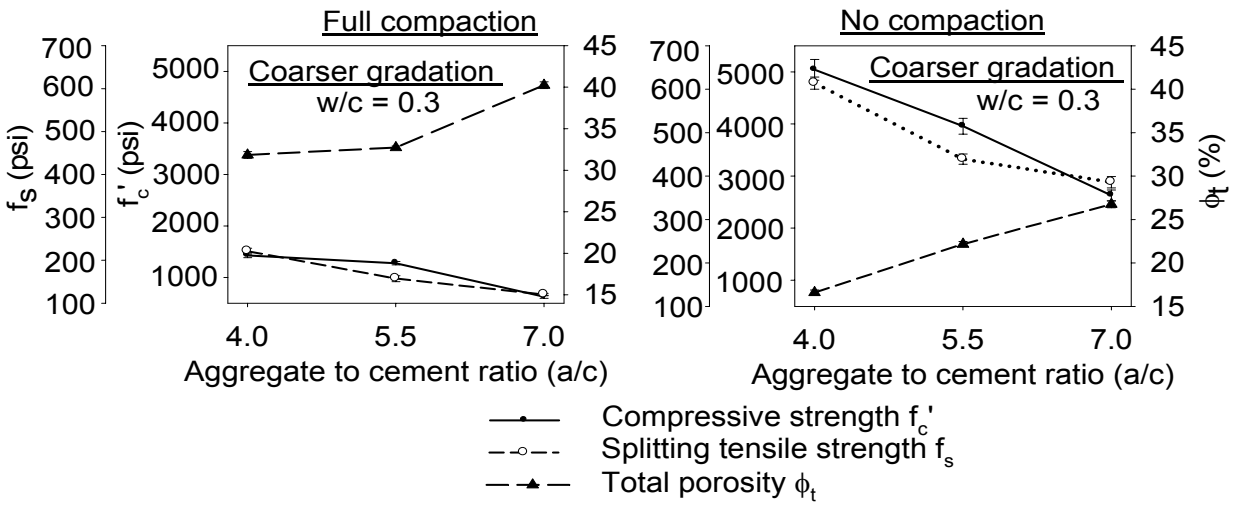

Figure 6-3 Summary of the influence of aggregate to cement ratio (a/c) on CPP strength (f_c' and f_s at 28 days) and total porosity (ϕ_t). For a given water to cement ratio (w/c) and a given gradation, lower a/c ratios generates lower ϕ_t which results in higher f_c' and f_s for CPP specimens with full compaction and CPP specimens with no compaction. All strength results tested at 28 days.

6.5.2.6 Influence of Gradation on Strength and ϕ_t

With the same w/c of 0.3, and a/c of 5.5, test results of $f_c^{'}$, f_s, and ϕ_t for the finer gradation and coarser gradation were compared in Figure 6-4. Results indicate that for a given w/c of 0.3, and a given a/c of 5.5, the coarser gradation generated higher $f_c^{'}$ and f_s and lower ϕ_t as compared to the finer gradation. For fully compacted specimens, $f_c^{'}$ = 4725 psi, f_s = 571 psi, and ϕ_t = 19.47% for the coarser gradation, while the finer gradation yielded an $f_c^{'}$ = 2875 psi, f_s = 305 psi, and ϕ_t = 23.70%.

6.5.2.7 Influence of the Degree of Compaction on CPP Strength and Porosity

Figure 6-5 summarizes the influence of the degree of compaction on CPP strength and porosity. Results indicate that the degree of compaction has a significant influence on CPP total porosity. For the same gradation (for example the coarser gradation) and a given w/c of 0.3, no compaction leads to a high total porosity ranging from 32 to 40% for a/c = 4.0, 5.5 and 7.0,

respectively; the 50% compaction leads to a total porosity ranging from 20-33%, while the 100% compaction results in total porosity from 18 to 25% for different a/c employed in the mix design. The significant differences of total porosity caused by different degrees of compaction resulted in significantly variability of CPP strength. Figure 6-5 illustrates that the full compacted specimens have an f_c' as high as 5000 psi and f_s of 600 psi when a/c = 4.0, and f_c' = 4700 psi, and f_s = 570 psi when a/c = 5.5. For those specimens with 50% compaction, f_c' = 2800 psi and f_s = 400 psi when a/c = 4.0, and f_c' = 2400 psi and f_s = 300 psi when a/c = 5.5. Results indicate that the degree of compaction is one of the critical factors by which CPP strength and porosity properties are determined.

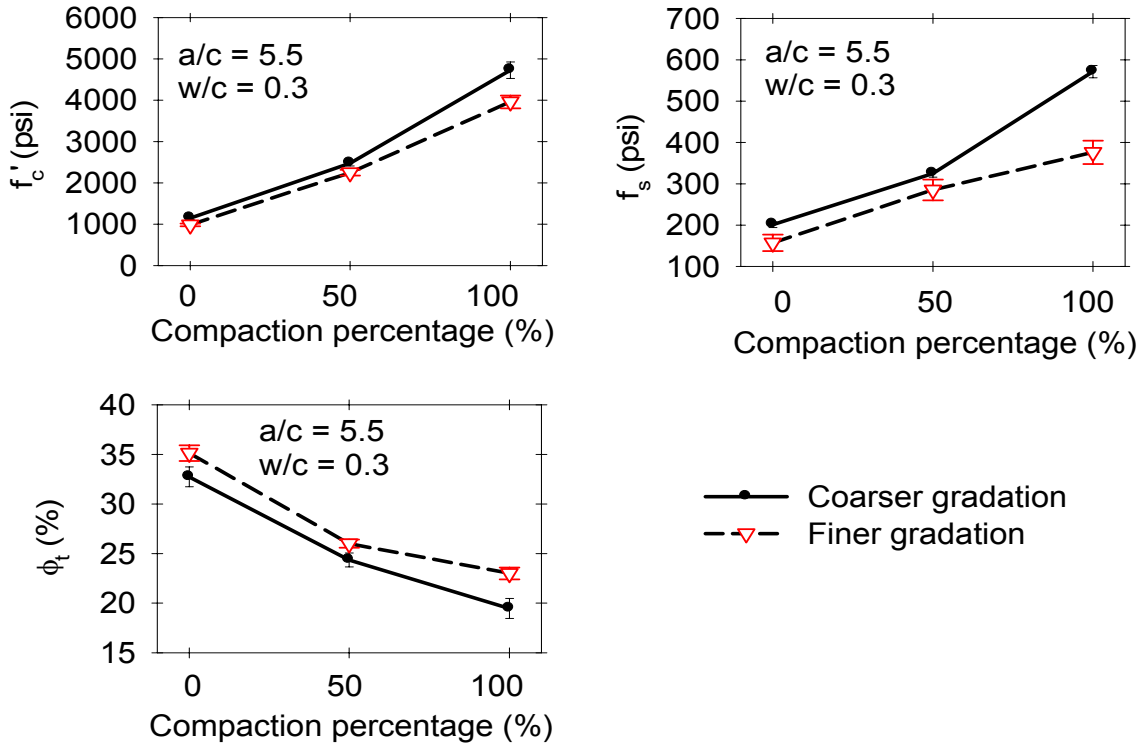

Figure 6-4 Aggregate gradation influence on CPP strength and total porosity. All specimen strength results tested at 28 days. It shows that the higher degree of compaction leads to lower percentage of total porosity and results in higher strength therefore.

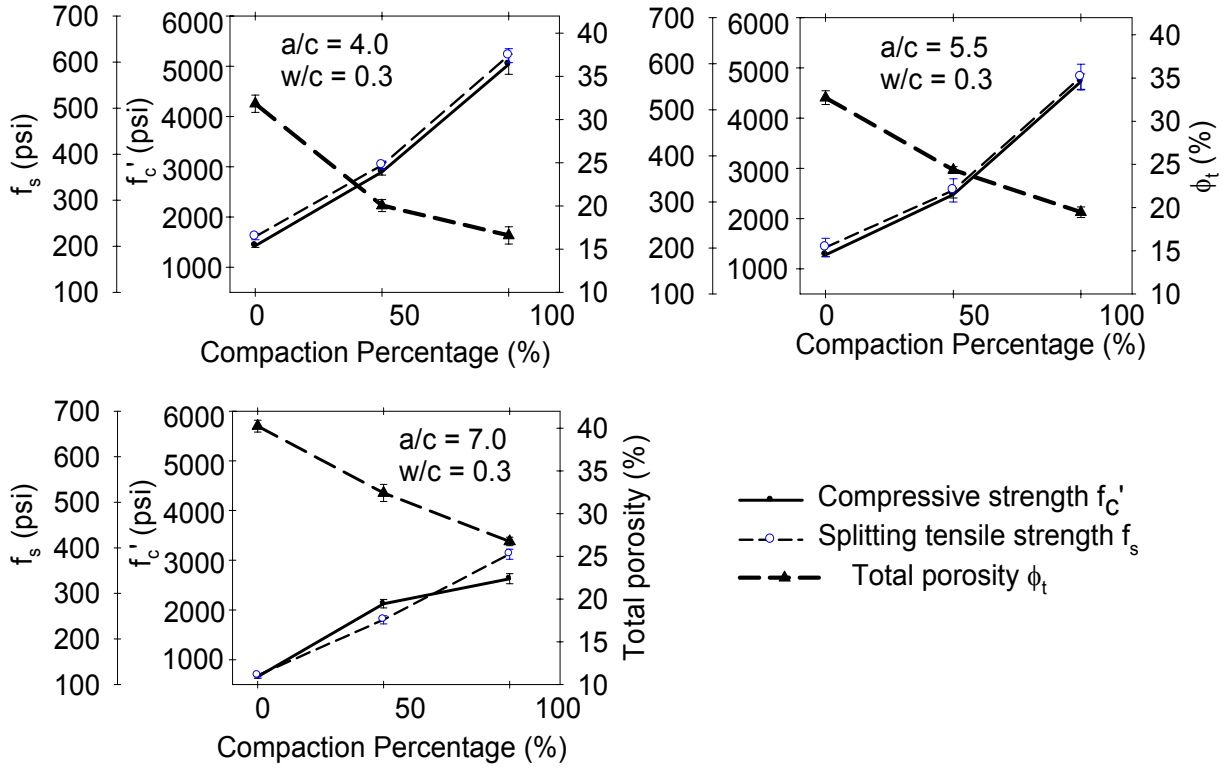

Figure 6-5 Influent of the degree of compaction on strength and total porosity for CPP specimens. Full compaction leads to lower total porosity and higher strength. All compressive strength (f_c'), splitting tensile strength (f_s) and total porosity (ϕ_t) were tested at 28 days.

6.5.2.8 f_c'-f_s Relationship

Based on test results on all batches of specimens, $f_c^{'}$ and f_s results are illustrated in Figure 6-6. A power law model was employed to describe the $f_c^{'}$ - f_s relationship.

$$f_s = 0.5478(f_c^{'})^{0.8328} \tag{6-22}$$

The model fit of the data yielded an $R^2 = 0.96$. Comparing the results predicted by other models previously developed by other researchers (ACI318-99 1999; Oluikun 1991; Akazawa 1953), it was found that this CPP mix design achieved a higher splitting tensile strength (f_s) for a given compressive strength (f_c').

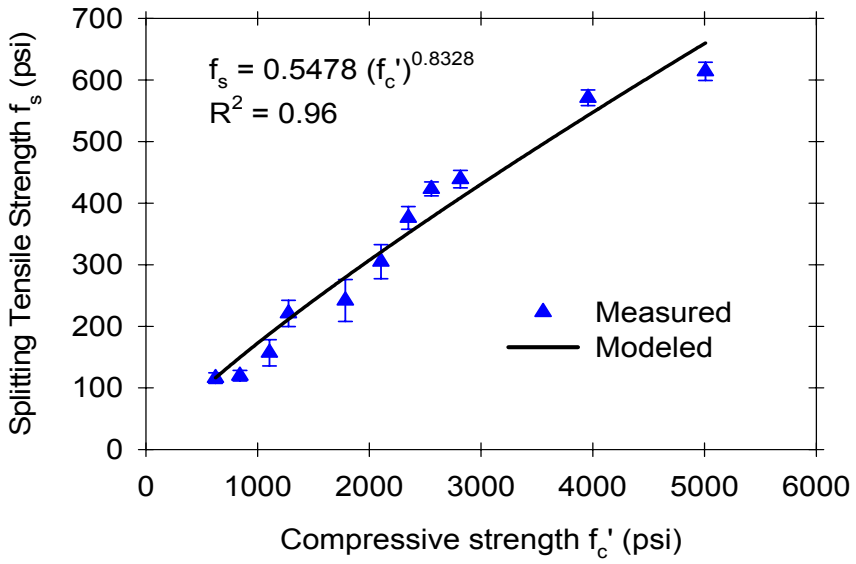

Figure 6-6 Relationship between compressive strength (f_c') and splitting tensile strength (f_s) for CPP materials, modeled as a power law: $f_s = 0.5478 \times (f_c')^{0.8328}$ with $R^2 = 0.96$. All compressive strength (f_c') and splitting tensile strength (f_s) were tested at 28 days.

6.5.2.9 f_c' -ϕ_t Relationship

Based on test results on all batches of specimens, the $f_c^{'}$ -ϕ_t relationship were illustrated in Figure 6-7. A exponential model was employed to describe the $f_c^{'}$ -ϕ_t relationship; the higher the total porosity, the lower the compressive strength.

$$f_c^{'} = 12909(e)^{-0.0638 \cdot \phi_t} \tag{6-23}$$

The model fit of the data yielded an $R^2 = 0.96$.

6.5.2.10 ϕ_t-k relationship

Based on the test results of total porosity and hydraulic conductivity, a relationship between ϕ_t and k could be developed, as illustrated in Figure 6-8. The relationship was modeled as a power law.

$$k = 1.6 \times 10^{-6} (\phi_t)^{3.714} \tag{6-24}$$

In this expression, *k* is in cm/s, and ϕ_t is in %. Model fit of the data yielded an $R^2 = 0.91$.

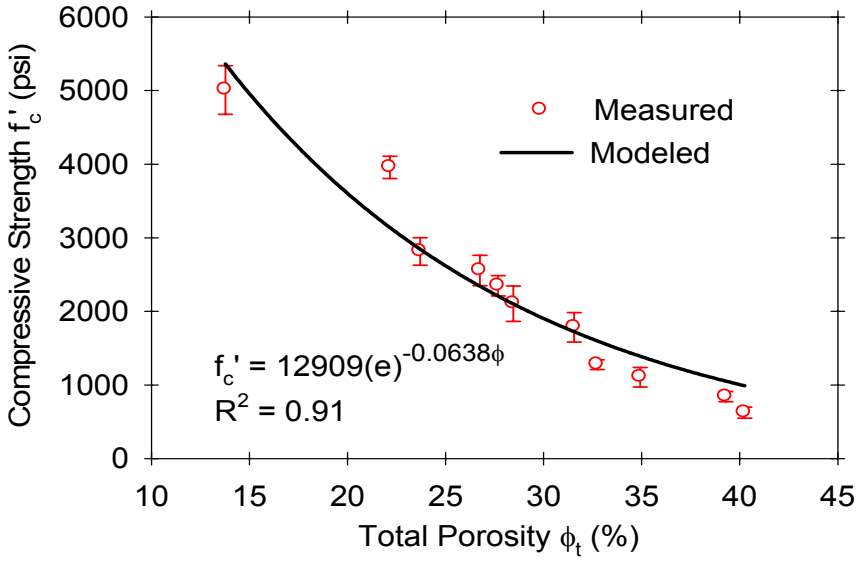

Figure 6-7 Relationship between compressive strength (f_c') and total porosity (ϕ_t) for CPP modeled using a first-order exponential model as $f_c' = 12909 \times (e)^{-0.0638\phi_t}$ with $R^2 = 0.91$. All compressive strength (f_c') and total porosity (ϕ_t) were tested at 28 days.

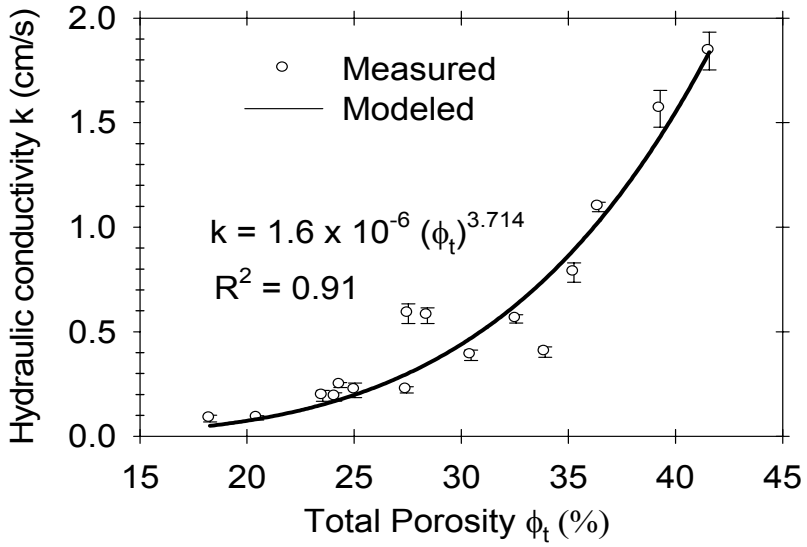

Figure 6-8 Relationship between total porosity (ϕ_t) and hydraulic conductivity (k) for CPP modeled as a power law: $k = 1.6 \times 10^{-6} (\phi_t)^{3.714}$ with $R^2 = 0.91$.

6.5.3 Suggested Mix Design

Based on the above analysis it was found that for CPP material, full compaction, lower a/c, lower w/c, and coarser well-gradated aggregates result in high strength and lower porosity. To reach a medium strength and high porosity for both traffic loading and stormwater management, it is necessary to find a balance among all of these factors. From the result analysis, a desirable mix design variables could be recommended as follows. Aggregate: coarser and open-graded aggregates with maximum aggregate size around 10 mm. At least 85% of crushed aggregate should be coarser than the No.8, and 5% of sand finer than No. 30 sieve are desirable. The w/c should be approximately 0.3 with an a/c of approximately 5 and a full degree of compaction. With this mix design, the expected results of the CPP would be as follows: Slump for fresh concrete: > 12.7 cm (5 in); Specific gravity: about 2.7; Strength: f_c' > 25 MPa (3500 psi), and f_s > 2.76 MPa (400 psi); Total porosity: > 20%; and hydraulic conductivity, k > 0.5 cm/s.

6.6 SUMMARY AND CONCLUSIONS

To design CPP with both desirable porosity and strength, 6 batches of mixes were designed with 3 different w/c of 0.3, 0.4 and 0.5, 3 different a/c of 4.0, 5.5 and 7.0, 2 aggregate gradations and 2 different maximum aggregate size of 3/8 and ½ in. The influence of design variables of w/c, a/c, gradation and the degree of compaction on CPP strength, porosity and permeability was investigated. Based on test results and analysis, the following conclusion could be drawn.

1) The factors of w/c, a/c, aggregate gradation and the degree of compaction have significant influence on CPP strength and porosity.
2) To achieve a CPP with desirable strength, full compaction is necessary.

3) For CPP materials with full compaction, under the same gradation and the same a/c, a lower w/c leads to a lower total porosity and a higher strength.
4) With an open-graded gradation and the same w/c, a lower a/c leads to a higher compressive and splitting tensile strength. This conclusion is in contrast with that for conventional impervious concrete. The reason is that for porous concrete, the high a/c will increase the total porosity which is a dominant factor that determines the properties of porous concrete strength.
5) With the same w/c and a/c, a higher percentage of fine aggregates lead to a lower total porosity, resulting a higher strength.
6) Based on test results on all batches of specimens, both the f_c' - f_s and k-ϕ_t relationship were expressed by a power law model.
7) A first-order exponential model f_c' -ϕ_t relationship was developed for CPP and provides a tool for prediction of CPP strength based on known total porosity.

6.7 NOTATIONS

Symbols used in this Chapter

CA: = coarse aggregate;

FA: = fine aggregate;

SSD: = saturated surface Dry condition of aggregates;

W: = weight of materials for CPP design before moisture correction, (lb);

f_{c0}': = compressive of concrete with no porosity;

f_c': = compressive strength, (psi);

f_s: = splitting tensile strength, (psi);

f_{dt}: = direct tensile strength, (psi);

f_r: = modulus of rupture, (psi);

k: = hydraulic conductivity, (cm/s);

p_m: = free moisture of aggregate;

w: = weight of materials for CPP after moisture correction, (lb);

ϕ_t: = total porosity (%);

ρ_s: = specific gravity;

a/c: = aggregate to cement ratio;

w/c: = water to cement ratio.

6.8 REFERENCES

Abdel-Jawad, Y.A. and W.S. Abdullah, 2002. "Design of maximum density aggregate grading". *Construction and Building Materials*, 16, pp 495-508

Abdullah W.S., M.T. Obaidat and N.M. Abu-Sa'da, "Influence of aggregate type and gradation on voids of asphalt concrete pavements", *ASCE Journal of Materials in Civil Engineering*, 10 (2), pp76-85.

ACI 435, 1968. "Deflection of Reinforced concrete flexural members". *ACI Manual of Concrete Practice*, Part II, pp32

ASTM C39/C 39M-04a, (2004). "Test Method for Compressive Strength of Cylindrical Concrete Specimens". *Annual Book of ASTM* 2004.

ASTM C70-94, (2004). "Test Method for Surface Moisture of Fine Aggregate". *Annual Book of ASTM 2004*.

ASTM C136-01, (2004). "Test Method of Sieve Analysis of Fine and Coarse Aggregates. *Annual Book of ASTM 2004*.

ASTM C143/c 143M-03, (2004). "Test Method for Slump of Hydraulic-Cement Concrete". *Annual Book of ASTM 2004*.

ASTM C231-03, (2004). "Test Method for Air Content of Freshly Mixed Concrete by the Pressure Method". *Annual Book of ASTM* 2004.

ASTM C496/C 496M-04, (2004). "Test Method for Splitting Tensile Strength of Cylindrical Specimens". *Annual Book of ASTM 2004*.

ASTM C642-97, (2004). "Test Method for Density, Absorption, and Voids in Hardened Concrete". *Annual Book of ASTM 2004*.

ASTM C684-99 (2003), (2004). "Test Method for Making, Accelerated Curing, and Testing Concrete Compressive Test Specimens". *Annual Book of ASTM 2004*.

ASTM C685/C 685M, (2004). "Specification for Concrete Made by Volumetric Batching and Continuous Mixing". *Annual Book of ASTM 2004*.

Akazawa, T., 1953, "Tensile test method for concretes" *RILEM Bulletin*, No. 16, pp13-23.

Bakhsh, A.H., F.F. Wafa, and A.A. Akhtaruzzaman, 1990. "Torsioal Behavior of high-strength concrete Beams". *ACI Structural Journal*, l 87 (5), pp 583-588

Blanks, R.F. and C.C. Mcnamara, 1935. " Mass Concrete test in large cylinders". *Journal of America Concrete Institute*, vol. 31, pp 280-303.

Desai, S., 2003. "Influence of constituents of concrete on its tensile strength and shear carrying capacity". *Magazine of Concrete Research*, 55 (1), pp 77-84.

Desai, S.B., 2004. "Influence of Constituents of concrete on its tensile strength and shear strength". *ACI Structural Journal*, January/February, pp30-39

Erntroy, H.C., and B.M. Shacklock, 1954. "Design of high-strength concrete mixes". Proc. of a Symposium on Mix Design and Quality Control of Concrete, *Cement and Concrete Association*, pp55-73

Franklin, R.E. and T.M.J. King, 1971. "Relations between compressive and indirect-tensile strength of concrete". *Road Research Lab Rep*. 32 pp.

Gilkey, H.J., 1961. "Water-cement ratio versus Strength another look". *Journal of ACI*, vol. 32, pp1287.

Goto, S. and D.M. Roy, 1981, "The effect of w/c ratio and curing temperature on the permeability of hardened cement paste", Cement and Concrete Research, 11, pp575-59;

Jerome, M.R., 1984. "Tensile Strength of Concrete". *ACI Journal*, Proceedings, vol. 32, pp158-165.

Kaplan, M.F., 1959. "Flexural and compressive strength concretes as affected by the properties of coarse aggregates". *ACI Journal*, Proceedings, vol. 55, pp1193-1208.

Kayyali, O.A., 1987. "Porosity of concrete in relation to the nature of the paste-aggregate interface". *Materials and Structures*, vol. 20, pp19-26.

Khan, A.A., W.D. Cook, and D. Mitchell, 1996. "Tensile strength of low, medium and high strength concrete at early ages". *ACI Materials Journal*, Sep./Oct., pp487-493

Kobayashi, T., M. Kagata, T. Kodama and M. Ito, 2002, Development of the environment-friendly hybrid permeable concrete pavement". *Transportation of the Janpan Concrete Institute*, vol. 23, pp65-76

Kolias, S., 1994. "Investigation of the possibility of estimating concrete strength by porosity measurements". *Materials and Structures*, vol. 27, pp 265-272.

Kumart, R. and B. Bhttacharjee, 2003, "Porosity, pore size distribution and in situ strength of concrete", *Cement and Concrete Research*, 33, pp155-164.

Lin, Z. and L. Wood, 2003. "Concrete uniaxial tensile strength and cylinder splitting test". *ASCE Journal of Structural Engineering*, 129 (5), pp 692-698.

Malhotra, V.M. and M. Branch, 1969. "Relations Between Splitting tensile, flexural and compressive strength of concrete". *Engineering Journal*, 52 (5), pp11-19

Mohammad, L.N., 2005, "Laboratory Evaluation of Aggregate Contributions to Permanent Deformation of HMA Mixtures." *13th Annual ICAR Symposium*, Austin, Texas

Mohammad, L.N., B. Huang, A. Abadie, and A. Raghavendra, 2000, "Laboratory Study of Large Stone Asphalt Mixtures." *Journal of the Association of Asphalt Paving Technologist*.

Neville, A.M., 1996. *Properties of Concrete*, Fourth Edition, Published by John Wiley & Sons, Inc. pp128-134, pp189-191, pp269-290, pp581-611 and pp724-748

Oluokun, F.A., 1991, "Prediction of concrete tensile strength from its compressive strength: evaluation of existing relations for normal weight concrete". *ACI Materials Journal*, May-June, pp302-309.

Park, S.B., and M. Tia, 2004. "An experimental study on the water-purification properties of porous concrete", Cement and Concrete Research, 34, pp 177-184.

Perry, C. and J.E. Gillott, 1977. "The influence of mortar-aggregate bond strength on the behaviour of concrete in uniaxial compression". *Cement and Concrete Research*, vol. 7, No.5, pp. 553-564.

Popovcs, S., "New formulas for the prediction of the effect of porosity on concrete strength". *ACI Journal*, March-April, pp136-146.

Raphael, J.M., 1984. "Tensile Strength of Concrete". *ACI Journal*, March-April, pp158-165.

Sansalone, J., L.Wang, Z. Teng, and X. Kuang. "Properties, Mechanism, and Application of Porous pavement as a passive Unit Operation and Process", *Proceeding of the 2004 World Water and Environment Resources Congress*, Salt Lake City, UT, June, 2004

Sansalone, J.J. and Z. Teng, 2004. “In-situ storm water treatment and recharge through infiltration: Quality and Quantity Attenuation”, *ASCE J. of Environmental Engineering*, 130(9), 990-1007.

Sansalone, J.J. and Z. Teng, 2005, “Transient Rainfall-Runoff Loadings to a Partial Exfiltration System: Implications for Water Quantity and Quality”, *ASCE J. of Environmental Engineering*, 131(8), pp. 1155-1167.

Sehgal, J.P., 1984. “Good concrete does not just happen: aggregate control/gradation vital to quality concrete Part I”. *Concrete/February*, 1984, pp30-36.

Tatro, S. and J.K. Hinds, 1992, "Roller Compacted Concrete Mix Design". *Roller Compacted Concrete III, Proceedings of the Conference ASCE*, San Diego, California, pp. 323-340

Wright, P.J.F., 1955. “Comments on an indirect tensile test on concrete cylinders”. *Magazine of Concrete Research*, Vol. 7, No. 20, pp87-96.

Yaman, I.O., H.M., Aktan and N. Hearn, 2002. “Active and non-active porosity in concrete Part II: Evaluation of existing models”. *Materials and Structures*, 34 (246), pp110-116.

Yaman, I.O., H.M., Aktan and N. Hearn, 2002. “Active and non-active porosity in concrete Part I: Experimental evidence”. *Materials and Structures*, 35, pp102-109.

CHAPTER 7 GLOBAL CONCLUSIONS

The degree of imperviousness in the built environment is significantly correlated to deleterious hydrologic, climate and environmental problems associated with urban land development and the increasing spatial extent of impervious pavement. Consequences that include increased peak flow, increased volume, increased temperature, decreased lag time of runoff, reduced underground water recharge, and degraded water quality have resulted in increasing deleterious effects to the built and natural environments.

In contrast, permeable pavement reduces rainfall-runoff peak, volume, improves water quality through physical and chemical mechanisms, facilitates groundwater and interflow recharge and mitigates temperature increases. A critical aspect of permeable pavements is characterization of their hydraulic and reactive behavior, in large part controlled by their pore characteristics. These pore characteristics were examined using XRT/image analysis and conventional techniques for cementitious permeable pavement (CPP) taken from the surface of a partial exfiltration reactor (PER) along I-75 in Cincinnati, OH.

XRT analysis results of ϕ_t, ϕ_e, d_{50a} (or A_{50a}), and (L_e/L) are nearly independent on the image resolution R_r, making XRT a useful tool to predict hydraulic and filtration constitutive properties of CPP. In contrast, (SSA), d_{50n} (or A_{50n}) results were dependent on R_r.

ϕ_t–ϕ_e relationship follows a power law correlation. Pore area distributions followed a Gaussian model while pore number distributions followed an exponential decay model. Correlation between $(SSA)_s$-d_{50n}-ϕ_t follows a power law relationship. Both the pdf of (L_e/L) and the (L_e/L)-ϕ_t relationship followed a Gaussian distribution.

Empirical hydraulic conductivity models, such as Hazen, Krüger, Fair-Hatch, Terzaghi, Bayer, USBR, Slichter model and the conventional Kozeny-Carman model, are not applicable for hydraulic conductivity estimation for CPP with typical porosity higher than 20%.

Factors that significantly influence fluid flow in porous media include effective porosity, pore connectivity and pore size distribution. A modified Kozeny-Carman model in which effective porosity ϕ_e, specific surface area based on effective pores $(SSA)_{pe}$, and weighted tortuosity $(L_e/L)_w$ were employed was developed applicable for prediction of CPP hydraulic conductivity.

(SSA) obtained by EGME method generate underestimated values in 3-5 order of magnitude when used for hydraulic conductivity estimation. For CPP, pores smaller than 1/100 of d_{50a} may be neglected. Both the K_{sat}- ϕ_t relationship and k_{sat}- ϕ_e relationship follows a power law model correlation.

CPP particle removal efficiency vary with different loading concentration. For a given stormwater particulate gradation, when $[m]_{i0}$ = 200 mg/L, η = 92.21%; when $[m]_{i0}$ = 100 mg/L, η = 88.74% and η = 83.76% for $[m]_{i0}$ = 50 mg/L, respectively. For different particle size fraction, particles coarser than 300 μm, removal efficiency was 100%, while for those finer than 25 μm, η is about 50%.

When the "schmutzdecke" thickness is more than 1.5 mm on the CPP surface, the infiltration rate of CPP drops to less than 10^{-4} cm/s. The decrease of infiltration rate caused by particle clogging is determined by both CPP material and the particle properties such as gradation and concentration.

The sonicating and backwash method can recover the CPP original infiltration rate up to 99%, while the vacuum suction method can recover it more than 96%. Under 100 mg/L particle loading, the CPP surface could be cleaned once every year by vacuum suction.

Runoff water quality can be significantly improved after infiltrating through CPP. The effluent turbidity is less than 10 NTU after 10 hours of filtration. The final turbidity is about 4 NTU. The turbidity-TSS relationship follows a power law model.

Both runoff pH value and alkalinity were elevated after infiltrating though CPP. For specimens exposed to runoff or rainfall for 3 years, the effluent pH was in the range of 7.8-8.5, and the alkalinity elevation rate was in the range of 11.5%-14.7%. When influent [TDP] ≈ 1.0 mg/L, TDP removal efficiency was in the range of 24.2 %- 28.5%. For TP removal, when influent [TP] ≈ 1.45 mg/L, TP removal efficiency was in the range of 46-50%.

For the aluminum coated CPP specimens, the effluent pH was in the range of 8.5 or higher, and the alkalinity elevation rate was in about 42%. TDP removal efficiency is up to 82%, the average TP removal efficiency is up to 85%. Total particulate phosphorus (TPP) removal efficiency was related to removed particles. Instead of mass or number of particles, particle surface area determines the removal efficiency of TPP.

All factors including w/c, a/c, aggregate gradation and the degree of compaction have significant influence on CPP strength and porosity properties. To achieve a CPP structural with desirable strength, full compaction is necessary. For CPP materials with full compaction, under the same gradation and the same a/c, a lower w/c leads to a lower total porosity and a higher strength. With the open graded gradation and the same w/c, a lower a/c leads to a higher compressive and splitting tensile strength. This conclusion is on the contrast with that drawn for standard impervious concrete.

With the same w/c and a/c, a higher percentage of fine aggregates leads to a lower total porosity, resulting a higher strength. Both the f_c' - f_s relationship and f_c' and -ϕ_t relationship could be expressed by a power law model.

A recommended mix design for CPP materials is as follows:

Aggregate: coarser and open grade aggregates with max aggregate size around 10 mm. At least 85% of crushed lime stone coarser than No.8, and 5% of sand finer than No. 30 are desirable;

w/c: less than 0.4, 0.3 is preferred;

a/c: around 4-5.5, and

Degree of compaction: full compaction.

With this design, the expected mix and CPP properties are:

Slump for fresh concrete: > 12.7 cm (5 in);

Specific gravity: about 2.7;

Strength: f_c' > 25 MPa (3500 psi), and f_s > 2.76 MPa (400 psi);

Total porosity: > 20%, and

Permeability: k > 0.5 cm/s.

CPP not only has the capability to control the quantity of runoff by reducing runoff peak flow rate, volume and concentration time through infiltration function, it also has the capability to control the quality of runoff by removing particles, particulate associated heavy metals and anthropogenic pollutants, phosphorus, and elevating alkalinity and pH values in runoff through filtration, absorption and reaction.

VITA

Xuheng Kuang is a native of Hunan Province, China. He received a Bachelor of Science degree in hydraulic engineering from Wuhan University of Hydraulic and Electrical Engineering in June 1994, and a Master of Science degree under the guidance of Professor Guanlin Liu in the fluid machinery and dynamic engineering in the same institute in June 1997. He began his doctoral career in Fall 2002, in the Department of Civil and Environmental Engineering of Louisiana State University under the guidance of Dr. John Sansalone. Xuheng will receive a doctorate in civil engineering from Louisiana State University in December 2005.